

SIMULATION OF THERMAL MECHANICAL AND OPTICAL BEHAVIOR OF
YAG CERAMICS WITH INCREASING Nd³⁺ CONCENTRATION UNDER
LASING CONDITIONS

A THESIS SUBMITTED TO
THE GRADUATE SCHOOL OF NATURAL AND APPLIED SCIENCES
OF
MIDDLE EAST TECHNICAL UNIVERSITY

BY

NECMETTİN KENAR

IN PARTIAL FULFILLMENT OF THE REQUIREMENTS
FOR
THE DEGREE OF DOCTOR OF PHILOSOPHY
IN
PHYSICS

MAY 2007

Approval of the Graduate School of Natural and Applied Sciences

Prof. Dr. Canan ÖZGEN
Director

I certify that this thesis satisfies all the requirements as a thesis for the degree of Doctor of Philosophy.

Prof. Dr. Sinan BİLİKMEN
Head of Department

This is to certify that we have read this thesis and that in our opinion it is fully adequate, in scope and quality, as a thesis for the degree of Doctor of Philosophy.

Prof. Dr. Gülay ÖKE
Supervisor

Examining Committee Members

Assoc. Prof. Dr. Akif ESENDEMİR (METU, PHYS) _____

Prof. Dr. Gülay ÖKE (METU, PHYS) _____

Prof. Dr. Nizami HASANLI (METU, PHYS) _____

Assoc. Prof. Dr. Serhat ÇAKIR (METU, PHYS) _____

Assist. Prof. Dr. M. Efe ÖZBEK (ATILIM Univ, EE) _____

I hereby declare that all information in this document has been obtained and presented in accordance with academic rules and ethical conduct. I also declare that, as required by these rules and conduct, I have fully cited and referenced all material and results that are not original to this work.

Name, Last name: Necmettin KENAR

Signature :

ABSTRACT

SIMULATION OF THERMAL, MECHANICAL AND OPTICAL BEHAVIOR OF YAG CERAMICS WITH INCREASING Nd³⁺ CONCENTRATION UNDER LASING CONDITIONS

KENAR, Necmettin

Ph.D., Department of Physics

Supervisor: Prof. Dr. Gülay ÖKE

May 2007, 142 pages

Two-dimensional thermal, mechanical and optical simulations are carried out to investigate the effect of Nd³⁺ concentration on thermal, mechanical and optical behavior of Nd:YAG ceramic laser materials under continuous wave laser operation.

In the analyses, rods are pumped longitudinally with laser diodes, in three, six, nine and twelve fold structures.

Rods having diameters of 3 and 6 mm are pumped with 808 nm and 885 nm sources separately having Nd³⁺ concentrations of 0.6, 1, 2, 3, 4 and 6 at. %.

Total absorbed pump power are kept constant for all rods. Absorbed pump power distribution are obtained for each rod using ray tracing method and Beer's Law.

In the analysis, temperature dependent material properties are incorporated. Nonlinear numerical solutions of thermal and stress equations have been performed. Temperature and stress results are obtained to investigate the effect of Nd concentration on the optical properties of ceramic YAG laser material. Analysis results reveal that, increase in Nd³⁺ concentration of YAG ceramic laser material, decreases the temperature and stress developed during optical pumping. Rods pumped with 808 nm source have large temperature and stress values compared to 885 nm pumped ones.

Optical path difference (OPD) of each ray passed through the material is calculated using thermal and elastic strain results together with photo-elastic constants of Nd:YAG material. Focal length and depolarization of each rod is calculated numerically from OPD results. Focal length of each rod is found to increase, in contrary depolarization is found to decrease with increase in the dopant concentration.

Keywords: Solid-state lasers, diode pumped lasers, ceramic laser materials, thermo-optical effects.

ÖZ

LAZER IŞINIMI SIRASINDA Nd³⁺ YOĞUNLUĞUNUN ARTMASI İLE YAG SERAMİKLERİNİN ISIL, MEKANİK VE OPTİKSEL DAVRANIŞLARININ BİLGİSAYAR ORTAMINDA İNCELENMESİ

KENAR, Necmettin

Doktora, Fizik Bölümü

Tez Yöneticisi: Prof. Dr. Gülay ÖKE

Mayıs 2007, 142 sayfa

Sürekli çalışma kipinde çalışan seramik Nd:YAG lazer malzemelerinde Nd³⁺ yoğunluğunun lazer malzemesinin ısı, mekanik ve optik özellikleri üzerine etkilerini araştırmak amacı ile iki boyutlu ısı, mekanik ve optik analizler bilgisayar ortamında yapılmıştır.

Analizlerde, çubuklar uzunlamasına lazer diyotları ile üçlü, altılı, dokuzlu ve on ikili dizilişlerde pompalanmıştır.

Üç ve altı milimetre çaplara sahip çubuklar 808 nm ve 885 nm de ışımaya yapan kaynaklar ile pompalanmıştır. Çubuklardaki Nd³⁺ oranları % 0.6, % 1, % 2, % 3, % 4 ve % 6 dır.

Tüm çubuklarda soğurulan pompalanan güç eşit tutulmuştur. Çubuklardaki soğurulan güç dağılımı, ışın iletme ve Beer kanunu kullanılarak elde edilmiştir.

Analizlerde sıcaklığa bağlı malzeme özellikleri kullanılmıştır. Isı ve gerilme denklemlerinin çözümünde doğrusal olmayan sayısal yöntem kullanılmıştır.

Nd yoğunluğunun seramik malzemenin optik özellikleri üzerine etkilerini araştırmak için ısı ve gerilme sonuçları elde edilmiştir. Analiz sonuçları Nd³⁺ yoğunluğunun artması ile malzeme içerisinde oluşan sıcaklık ve gerilme değerlerinin azaldığı sonucunu ortaya çıkarmıştır.

Farklı pompalama dalga boyları karşılaştırıldığında 808 nm ile pompalanan çubuklarda sıcaklık ve gerilme değerlerinin 885 nm ile pompalananlara göre daha yüksek olduğu ortaya çıkmıştır.

Malzeme içerisinden geçen her ışının uğradığı optik yol farkı, malzemede oluşan sıcaklık ve gerilme sonuçları yanında malzemenin opto-elastik özellikleri de kullanılarak hesaplanmıştır. Optik yol farkı sonuçları kullanılarak çubuklarda oluşan ısıl merceğin odak uzaklığı ve toplam polarizasyon bozunumu elde edilmiştir. Nd³⁺ yoğunluğunun artması ile ısıl merceğin odak uzaklığının uzadığı ve polarizasyon bozunumunun azaldığı gözlenmiştir.

Anahtar Kelimeler: Katı hal lazerler, diyot pompalı lazerler, seramik lazer malzemeleri, ısıl ve optik etkiler

To My Parents

ACKNOWLEDGMENTS

I would like to express my sincere thanks to my advisor Prof. Dr. Gülay ÖKE for her support, guidance and careful reading of manuscript.

I am grateful to Assoc. Prof. Dr. Akif ESENDEMİR for his fruitful criticism during thesis progress stage and for the opportunity to work in proposal preparation of his projects.

I am grateful to Assist. Prof. Dr. M. Efe ÖZBEK for his guidance and criticism during thesis progress stage and careful reading of manuscript.

I would like to express my sincere thanks Prof. Dr. Sinan BİLİKMEN for the opportunity to study on lasers as a member of Physics Department and for the opportunity to work in proposal preparation of his projects.

I would like to thank to Mr. Semih ÖZEL from Genel Makina Tasarım Ltd. Şti. for his kind support and encouragement during the thesis work.

At last but not least I would like to express my sincere thanks to my family for their patient and support during my work.

TABLE OF CONTENTS

ABSTRACT.....	iv
ÖZ.....	vi
ACKNOWLEDGMENTS.....	ix
TABLE OF CONTENTS.....	x
LIST OF TABLES.....	xiii
LIST OF FIGURES.....	xv
CHAPTERS	
1 CERAMIC Nd:YAG.....	1
1.1 Introduction.....	1
1.2 Manufacturing Process.....	2
1.3 Optical Properties.....	3
1.4 Physical Properties.....	7
1.5 Laser Performance.....	9
2 THERMO-OPTIC EFFECTS.....	11
2.1 Introduction.....	11
2.2 Heat Dissipation Factor.....	12
2.3 Temperature Distribution.....	14
2.4 Thermal Stresses.....	15
2.5 Stress Birefringence.....	16
2.6 Refractive Index Distribution.....	18
2.7 Depolarization.....	20
2.8 Thermal Lens Effect.....	21

3. ABSORBED POWER DISTRIBUTION	24
3.1 Introduction	24
3.2 Pump Structure	25
3.3 Pump Source	26
3.4 Ray Tracing	27
3.5 Absorption	29
4. THERMO-ELASTICITY ANALYSIS	38
4.1 Introduction	38
4.2 Heat Equation	39
4.3 Elasticity Equations	40
4.4 Finite Element Analysis	44
4.5 Results	45
4.5.1 Temperature distributions	45
4.5.2 Thermal Gradient Distribution	47
4.5.3 Radial Stress	50
4.5.4 Azimuthal Stress	52
4.5.5 Axial Stress	54
4.5.6 Shear Stress	57
4.5.7 Von Mises Stress	58
5. OPTICAL ANALYSIS	61
5.1 Introduction	61
5.2 Temperature Index Variations	62
5.3 Birefringence	63
5.4 Depolarization	64
5.5 Focal Length	65
5.6 Results	66
5.6.1 Temperature Index Variations	66
5.6.2 Birefringence	67
5.6.3 Depolarization	72
5.6.4 Focal Length	74

6. DISCUSSION	80
6.1 Introduction	80
6.2 Effect of Dopant Concentration	80
6.3 Effect of Pump Structure.....	84
6.4 Effect of Pump Wavelength	85
7. CONCLUSION	87
REFERENCES	89
APPENDICES	
I. MATERIAL PROPERTIES	93
II. ABSORBED POWER DENSITY DISTRIBUTION	95
III. TEMPERATURE DISTRIBUTION RESULTS	99
IV. TEMPERATURE GRADIENT RESULTS	103
V. RADIAL STRESS RESULTS	107
VI. AZIMUTHAL STRESS RESULTS	111
VII. AXIAL STRESS RESULTS	115
VIII. SHEAR STRESS RESULTS	119
IX. VON MISES STRESS RESULTS	123
X. INDEX VARIATION DUE TO TEMPERATURE	127
XI. INDEX VARIATION FOR RADIALY POLARIZED LIGHT.....	131
XII. INDEX VARIATION FOR AZIMUTHALLY POLARIZED LIGHT	135
XIII. DEPOLARIZATION	139
CURRICULUM VITAE	143

LIST OF TABLES

<i>Table 1. 1 - Ceramic Laser Reports</i>	<i>10</i>
<i>Table 4. 1– Boundary conditions</i>	<i>44</i>
<i>Table A1. 1 - Youngs Modulus and Poissons Ratio [23].....</i>	<i>93</i>
<i>Table A2. 1- Absorbed power density distribution of 3mm rod pumped with 808 nm source.....</i>	<i>95</i>
<i>Table A2. 2 - Absorbed power density distribution of 6 mm rod pumped with 808 nm source.....</i>	<i>96</i>
<i>Table A2. 3 - Absorbed power density distribution of 3 mm rod pumped with 885 nm source.....</i>	<i>97</i>
<i>Table A2. 4 - Absorbed power density distribution of 6 mm rod pumped with 885 nm source.....</i>	<i>98</i>
<i>Table A3. 1- Temperature distribution of 3mm rod pumped with 808 nm source.....</i>	<i>99</i>
<i>Table A3. 2- Temperature distribution of 6 mm rod pumped with 808 nm source.....</i>	<i>100</i>
<i>Table A3. 3- Temperature distribution of 3 mm rod pumped with 885 nm source.....</i>	<i>101</i>
<i>Table A3. 4- Temperature distribution of 6 mm rod pumped with 885 nm source.....</i>	<i>102</i>
<i>Table A4. 1– Thermal gradient distribution of 3 mm rod pumped with 808 nm source.....</i>	<i>103</i>
<i>Table A4. 2- Thermal gradient distribution of 6 mm rod pumped with 808 nm source</i>	<i>104</i>
<i>Table A4. 3- Thermal gradient distribution of 3 mm rod pumped with 885 nm source</i>	<i>105</i>
<i>Table A4. 4- Thermal gradient distribution of 6 mm rod pumped with 885 nm source</i>	<i>106</i>
<i>Table A5.1- Radial stress distribution of 3 mm rod pumped with 808 nm source.....</i>	<i>107</i>
<i>Table A5.2- Radial stress distribution of 6 mm rod pumped with 808 nm source.....</i>	<i>108</i>
<i>Table A5.3- Radial stress distribution of 3 mm rod pumped with 885 nm source.....</i>	<i>109</i>
<i>Table A5.4- Radial stress distribution of 6 mm rod pumped with 885 nm source.....</i>	<i>110</i>
<i>Table A6. 1-Azimuthal stress distribution of 3 mm rod pumped with 808 nm source</i>	<i>111</i>
<i>Table A6. 2- Azimuthal stress distribution of 6 mm rod pumped with 808 nm source</i>	<i>112</i>
<i>Table A6. 3- Azimuthal stress distribution of 3 mm rod pumped with 885 nm source</i>	<i>113</i>
<i>Table A6. 4- Azimuthal stress distribution of 6 mm rod pumped with 885 nm source</i>	<i>114</i>
<i>Table A7.1– Axial stress distribution of 3 mm rod pumped with 808 nm source</i>	<i>115</i>
<i>Table A7.2- Axial stress distribution of 6 mm rod pumped with 808 nm source.....</i>	<i>116</i>
<i>Table A7.3- Axial stress distribution of 3 mm rod pumped with 885 nm source.....</i>	<i>117</i>
<i>Table A7.4- Axial stress distribution of 6 mm rod pumped with 885 nm source.....</i>	<i>118</i>
<i>Table A8. 1– Shear stress distribution of 3 mm rod pumped with 808 nm source</i>	<i>119</i>
<i>Table A8. 2– Shear stress distribution of 6 mm rod pumped with 808 nm source</i>	<i>120</i>
<i>Table A8.3- Shear stress distribution of 3 mm rod pumped with 885 nm source.....</i>	<i>121</i>
<i>Table A8. 4- Shear stress distribution of 6 mm rod pumped with 885 nm source.....</i>	<i>122</i>
<i>Table A9. 1 – von Mises stress distribution of 3 mm rod pumped with 808 nm source.....</i>	<i>123</i>
<i>Table A9. 2 – von Mises stress distribution of 6 mm rod pumped with 808 nm source.....</i>	<i>124</i>

<i>Table A9. 3- von Mises stress distribution of 3 mm rod pumped with 885 nm source.....</i>	<i>125</i>
<i>Table A9.4- von Mises stress distribution of 6 mm rod pumped with 885 nm source</i>	<i>126</i>
<i>Table A10. 1 - Thermal index change distribution of 3 mm rod pumped with 808 nm source.....</i>	<i>127</i>
<i>Table A10. 2 - Thermal index change distribution of 6 mm rod pumped with 808 nm source.....</i>	<i>128</i>
<i>Table A10. 3- Thermal index change distribution of 3 mm rod pumped with 885 nm source.....</i>	<i>129</i>
<i>Table A10. 4- Thermal index change distribution of 6 mm rod pumped with 885 nm source.....</i>	<i>130</i>
<i>Table A11. 1- Stress induced index change distribution of 3 mm rod pumped with 808 nm source for radially polarized light.....</i>	<i>131</i>
<i>Table A11. 2- Stress induced index change distribution of 6 mm rod pumped with 808 nm source for radially polarized light.....</i>	<i>132</i>
<i>Table A11. 3- Stress induced index change distribution of 3 mm rod pumped with 885 nm source for radially polarized light.....</i>	<i>133</i>
<i>Table A11. 4- Stress induced index change distribution of 6 mm rod pumped with 885 nm source for radially polarized light.....</i>	<i>134</i>
<i>Table A12. 1- Stress induced index change distribution of 3 mm rod pumped with 808 nm source for azimuthally polarized light.....</i>	<i>135</i>
<i>Table A12. 2- Stress induced index change distribution of 6 mm rod pumped with 808 nm source for azimuthally polarized light.....</i>	<i>136</i>
<i>Table A12. 3 - Stress induced index change distribution of 3 mm rod pumped with 885 nm source for azimuthally polarized light.....</i>	<i>137</i>
<i>Table A12. 4- Stress induced index change distribution of 6 mm rod pumped with 885 nm source for azimuthally polarized light.....</i>	<i>138</i>
<i>Table A13. 1- Depolarization distribution of 3 mm rod pumped with 808 nm source</i>	<i>139</i>
<i>Table A13. 2- Depolarization distribution of 6 mm rod pumped with 808 nm source</i>	<i>140</i>
<i>Table A13. 3- Depolarization distribution of 3 mm rod pumped with 885 nm source</i>	<i>141</i>
<i>Table A13. 4 - Depolarization distribution of 6 mm rod pumped with 885 nm source</i>	<i>142</i>

LIST OF FIGURES

<i>Figure 1. 1- Fluorescence spectrum from 1045 nm to 1085 nm; a) 1% Nd:YAG ceramic, b) 0.9% Nd:YAG single crystal [17].....</i>	4
<i>Figure 1. 2– a) Fluorescence redshift versus neodymium concentration, b) FWHM at 1064 nm versus neodymium concentration [17].</i>	5
<i>Figure 1.3- Fluorescence lifetime as a function of Nd³⁺ concentration. The open squares show the experimental data for the ceramics and the closed triangles for the single crystals [12].....</i>	5
<i>Figure 1. 4- Absorption spectra of 2.0, 3.4, and 6.6 at. % Nd:YAG ceramics (solid curves) and 1.0 at. % Nd:YAG single crystal (dashed curve) [12].....</i>	6
<i>Figure 1. 5 - Concentration-dependent broadening of Nd:YAG absorption lines at 300 K [14].....</i>	6
<i>Figure 1. 6- The absorption profile of Nd:YAG ceramics (1.0 and 9.0 at. % doping) at room temperature around 885 nm [19].....</i>	7
<i>Figure 1.7- The experiment results on the thermal conductivity of the YAG single crystal and polycrystal [23].....</i>	8
<i>Figure 2.1– Temperature distribution across the laser rod of f6x50mm.....</i>	15
<i>(h=2 W/cm²°K, k=0.13 W/cm°K, T_h=298°K).....</i>	15
<i>Figure 2. 2– Radial, azimuthal and axial stress components within Nd:YAG crystal rod as a function of radial distance.....</i>	16
<i>Figure 2. 3 – State of refractive index in rod shaped material.....</i>	18
<i>Figure 2. 4 – Laser rod focal length dependence on a) heat power, b) crystal length and c) crystal radius</i>	23
<i>Figure 3. 1- Model Used for the analysis.....</i>	25
<i>Figure 3. 2 - Absorption coefficients of ceramic Nd:YAG for 808 nm and 885 nm</i>	26
<i>Figure 3. 3 – Ray discretization for ray tracing.....</i>	28
<i>Figure 3. 4 – Ray tracing results; a) 3 mm rod, b) 6 mm rod</i>	28
<i>Figure 3. 5 – Intensities assigned to each individual ray.....</i>	30
<i>Figure 3. 6 – Grid used in power distribution calculations (a), representative power matrix for 11x11 grid.....</i>	31
<i>Figure 3. 7 – Step wise power density matrix construction.....</i>	31
<i>Figure 3. 8– Absorbed power density distributed along the radius of rod a) 3 mm and b) 6 mm using 808 nm pump source</i>	33
<i>Figure 3. 9 - Absorbed power density distributed along the radius of rod a) 3 mm and b) 6 mm using 885.....</i>	34

<i>Figure 3. 10 – Percent of absorbed power distributed along the radius of rod a) 3 mm and b) 6 mm using 808 nm pump source.....</i>	<i>36</i>
<i>Figure 3. 11 - Percent of absorbed power distributed along the radius of rod a) 3 mm and b) 6 mm using 885 nm pump source.....</i>	<i>37</i>
<i>Figure 4. 1 – Maximum temperature in rods a) 3 mm and b) 6 mm using 808 nm pump source and in rods c) 3mm and d) 6 mm using 885 nm pump source as a function of % at. Nd concentrations.....</i>	<i>46</i>
<i>Figure 4. 2 – Temperature distribution as a function of radial distance of 9-fold pump structure a) 3mm and b) 6mm rods with 808 nm pump source and c) 3mm and d) 6mm rods with 885 nm pump source.....</i>	<i>47</i>
<i>Figure 4. 3- Maximum thermal gradient in rods a) 3 mm and b) 6 mm using 808 nm pump source and in rods c) 3mm and d) 6 mm using 885 nm pump source as a function of % at. Nd concentrations.....</i>	<i>48</i>
<i>Figure 4. 4 - Thermal gradient distribution as a function of radial distance of 9-fold pump structure a) 3mm and b) 6mm rods with 808 nm pump source and c) 3mm and d) 6mm rods with 885 nm pump source.....</i>	<i>49</i>
<i>Figure 4. 5 - Maximum radial stress in rods a) 3 mm and b) 6 mm using 808 nm pump source and in rods c) 3mm and d) 6 mm using 885 nm pump source as a function of % at. Nd concentrations.....</i>	<i>50</i>
<i>Figure 4. 6 – Radial stress distribution as a function of radial distance of 9-fold pump structure a) 3mm and b) 6mm rods with 808 nm pump source and c) 3mm and d) 6mm rods with 885 nm pump source.....</i>	<i>51</i>
<i>Figure 4. 7 - Maximum azimuthal stress in rods a) 3 mm and b) 6 mm using 808 nm pump source and in rods c) 3mm and d) 6 mm using 885 nm pump source as a function of % at. Nd concentrations....</i>	<i>53</i>
<i>Figure 4. 8 - Azimuthal stress distribution as a function of radial distance of 9-fold pump structure a) 3mm and b) 6mm rods with 808 nm pump source and c) 3mm and d) 6mm rods with 885 nm pump source.....</i>	<i>54</i>
<i>Figure 4. 9 - Maximum axial stress in rods a) 3 mm and b) 6 mm using 808 nm pump source and in rods c) 3mm and d) 6 mm using 885 nm pump source as a function of % at. Nd concentrations.....</i>	<i>55</i>
<i>Figure 4. 10 - Axial stress distribution as a function of radial distance of 9-fold pump structure a) 3mm and b) 6mm rods with 808 nm pump source and c) 3mm and d) 6mm rods with 885 nm pump source.....</i>	<i>56</i>
<i>Figure 4. 11 - Maximum shear stress in rods a) 3 mm and b) 6 mm using 808 nm pump source and in rods c) 3mm and d) 6 mm using 885 nm pump source as a function of % at. Nd concentrations.....</i>	<i>57</i>
<i>Figure 4. 12 - Maximum von Mises stress in rods a) 3 mm and b) 6 mm using 808 nm pump source and in rods c) 3mm and d) 6 mm using 885 nm pump source as a function of % at. Nd concentrations.....</i>	<i>59</i>
<i>Figure 4. 13 – von Mises stress distribution as a function of radial distance of 9-fold pump structure a) 3mm and b) 6mm rods with 808 nm pump source and c) 3mm and d) 6mm rods with 885 nm pump source.....</i>	<i>60</i>
<i>Figure 5. 1 – Temperature dependence of refractive index coefficient on temperature.....</i>	<i>63</i>

Figure 5. 2– Thermal index variation as a function of radial distance of 9-fold pump structure a) 3mm and b) 6mm rods with 808 nm pump source and c) 3mm and d) 6mm rods with 885 nm pump source.....	67
Figure 5. 3 – Azimuthally polarized light index variation as a function of radial distance of 9-fold pump structure a) 3mm and b) 6mm rods with 808 nm pump source and c) 3mm and d) 6mm rods with 885 nm pump source.....	69
Figure 5. 4 – Radially polarized light index variation as a function of radial distance of 9-fold pump structure a) 3mm and b) 6mm rods with 808 nm pump source and c) 3mm and d) 6mm rods with 885 nm pump source	70
Figure 5. 5- Ratio of stress induced index variations of azimuthally polarized light to temperature induced index variations as a function of radial distance of 9-fold pump structure a) 3mm and b) 6mm rods with 808 nm pump source and c) 3mm and d) 6mm rods with 885 nm pump source.....	71
Figure 5. 6 - Ratio of stress induced index variations of radially polarized light to temperature induced index variations as a function of radial distance of 9-fold pump structure a) 3mm and b) 6mm rods with 808 nm pump source and c) 3mm and d) 6mm rods with 885 nm pump source.....	72
Figure 5. 7 - Depolarization as a function of % Nd^{3+} at. concentration a) 3mm and b) 6mm rods with 808 nm pump source and c) 3mm and d) 6mm rods with 885 nm pump source.....	73
Figure 5. 8- Azimuthally polarized light focal length as a function of % Nd^{3+} at. concentration a) 3mm and b) 6mm rods with 808 nm pump source and c) 3mm and d) 6mm rods with 885 nm pump source.....	74
Figure 5. 9- Radially polarized light focal length as a function of % Nd^{3+} at. concentration a) 3mm and b) 6mm rods with 808 nm pump source and c) 3mm and d) 6mm rods with 885 nm pump source	75
Figure 5. 10- Ratio of the difference of radially polarized light focal length and azimuthally polarized light focal length to the azimuthally polarized light one as a function of % Nd^{3+} at. concentration a) 3mm and b) 6mm rods with 808 nm pump source and c) 3mm and d) 6mm rods with 885 nm pump source.....	76
Figure 5. 11 – Percentage contribution of stress induced OPD to the focal length calculated from temperature induced OPD of azimuthally polarized light as a function of % Nd^{3+} at. concentration a) 3mm and b) 6mm rods with 808 nm pump source and c) 3mm and d) 6mm rods with 885 nm pump source.....	77
Figure 5. 12 - Percentage contribution of stress induced OPD to the focal length calculated from temperature induced OPD of radially polarized light as a function of % Nd^{3+} at. concentration a) 3mm and b) 6mm rods with 808 nm pump source and c) 3mm and d) 6mm rods with 885 nm pump source.....	78
Figure 5. 13 Related OPD distributions of 6 mm rod in 9-fold pump structure pumped with 808 nm source, a) azimuthally polarized light, b) radially polarized light.....	79

CHAPTER 1

CERAMIC Nd:YAG

1.1 Introduction

First Nd:YAG ($\text{Nd:Y}_3\text{Al}_5\text{O}_{12}$) laser material was discovered by Guesic et al. [1] in 1964. Since its discovery, Nd:YAG was the most important solid-state laser material. Nd:YAG lasers are used in research, medicine and industry and these lasers are the second most available laser type in the market following CO_2 gas laser.

Fabrication technique used in the manufacturing of Nd:YAG single crystal is Czochralski method, a type of melt-grown techniques. Since its discovery, grown technique was improved and crystals with good optical quality became available in the market. Czochralski grown single crystals have some limitations that make difficult to scale it to high laser powers. Main limitations are:

- Dope concentrations above 1.5 % are difficult to obtain [2]
- There is variation in dope concentration in growth direction [3, 4]
- Large size crystals cannot be manufactured
- Crystal growth process takes weeks [3]
- Crystal growth process is expensive [5].

In order to overcome these limitations attempts to produce polycrystalline laser materials was first reported by Greskovich et al. [6, 7]. However, due to excessive scattering by residual pores less than 0.5 mm in size, the laser efficiency was unsatisfactory. DeWith et al. [8] and Sekita et al. [9] reported efforts to fabricate transparent YAG ceramics for optical applications, but their ceramics were of insufficient quality to achieve the optical properties of single-crystal Nd:YAG.

Ikesue et al. [10, 11] was the first to demonstrate the possibility of fabricating transparent Nd:YAG ceramics of sufficient quality for solid-state lasers with reasonable efficiency. Recently, a number of studies have shown that transparent polycrystalline Nd:YAG is equivalent or better than single crystals grown by the Czochralski method [12-16]. Advantages of polycrystalline Nd:YAG ceramics can be stated as follow:

- Doping concentration can be increased to as much as 9 at. %
- A homogeneous dopant distribution can be achieved
- The specimen size can be significantly increased
- Production process takes days
- Process is simple and cheaper.

Ceramic materials generally include residual pores and grain boundaries. Pores and grain boundaries are source of scattering which results in optical loss [12, 13]. The excellent quality of the Nd:YAG ceramic with low pore volume and narrow grain boundary ensures its near equivalence to Nd:YAG crystal in its optical and stimulated emission properties [13].

1.2 Manufacturing Process

The fabrication process of polycrystalline Nd:YAG ceramics with good optical quality was first reported by Ikesue et al. [10,11]. Commercially available high-purity Y_2O_3 , Al_2O_3 , and Nd_2O_3 powders of 99.99 %-99.999 % purity with primary particle sizes less than micron are used as starting materials. These powders are blended with the stoichiometric ratio of YAG and ball milled for 12 h in ethanol, with 0.5 mass % tetraethyl orthosilicate (TEOS) added as a sintering aid. Then, the alcohol solvent is removed by spray drying the milled slurry. Spherical granules (ca. 30–50 μm) having a homogeneous composition are obtained. The spray-dried powder is pressed with low pressure into required shapes in a metal mold and then cold isostatically pressed at 98–196 MPa. Transparent Nd:YAG ceramics are

obtained after sintering under vacuum (1×10^{-3} Pa) at 1750°C for 10 h. Then, the specimens are processed into the required configuration and used in laser oscillation.

Recently fabrication of single crystal starting with polycrystalline material has been reported by Ikesue et al. [16]. In the case of single-crystal fabrication, after pre-sintering the powder compacts at 1550°C for 3 h under vacuum, the surface of the specimen is mirror polished. The polished surface of the polycrystal Nd:YAG ceramic is bonded with an undoped YAG single crystal (seed crystal of $\langle 111 \rangle$, $\langle 110 \rangle$, or $\langle 100 \rangle$) grown by the Czochralski method. Then, the bonded sample is heated at $1700^{\circ} - 1840^{\circ}\text{C}$. Continuous grain growth occurs from the seed crystal toward the polycrystal region and finally the whole polycrystal changes into Nd:YAG single crystal.

1.3 Optical Properties

Optical properties of a material are its transparency, fluorescence and absorption spectrum, fluorescence decay time, refractive index and variation of refractive index with temperature.

Fluorescence spectrum was demonstrated to be nearly the same for single crystals and ceramics for the same concentration ratio [17]. Figure 1.1 [17] shows the room-temperature fluorescence spectrum for ${}^4\text{F}_{3/2}$ to ${}^4\text{I}_{11/2}$ transition of 1% Nd:YAG single crystal and ceramics, respectively. From this figure, these two spectra are almost identical. The main emission peak is at 1064.18 nm. Full width at half maximum (FWHM) is 0.78 nm. With increase in dopant concentration, a little redshift in wavelength has been observed. Figure 1.2a [17] shows the main fluorescence peak spectra near 1064 nm for 0.6%, 1%, 2% and 4% Nd:YAG ceramics, respectively. The four emission peaks are centered at 1064.15 nm, 1064.18 nm, 1064.24 nm and 1064.30 nm for 0.6%, 1%, 2% and 4% Nd:YAG ceramics, respectively. The redshift from 0.6% to 4% Nd:YAG ceramics is 0.12 nm. Because of the fluorescent quenching effect, the fluorescence emission line width at 1064 nm

is also a little broadened with the concentration increases greater than 1%. Figure 1.2b shows the FWHM of the 1064-nm fluorescence peak. The FWHMs are 0.78 nm, 0.78 nm, 0.81 nm and 0.85 nm for 0.6%, 1%, 2% and 4% Nd:YAG ceramics, respectively. The line widths for 0.6% and 1% Nd:YAG ceramics are identical. It means that the fluorescent quenching effect is very weak for neodymium concentration less than 1%, which is similar to that of single crystal.

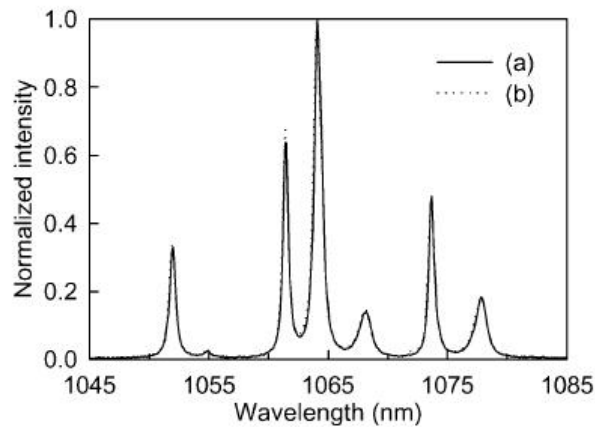
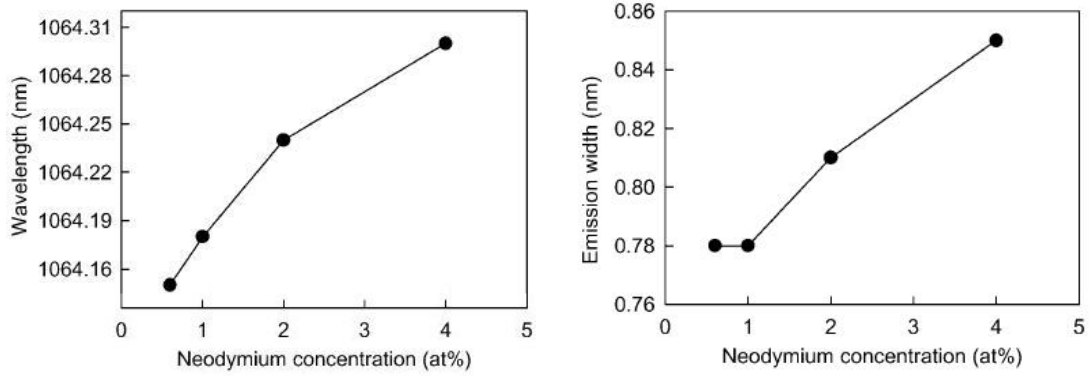


Figure 1. 1- Fluorescence spectrum from 1045 nm to 1085 nm; a) 1% Nd:YAG ceramic, b) 0.9% Nd:YAG single crystal [17]

Fluorescence lifetime was observed to decrease with increasing concentration [12, 17]. As given in Figure 1.3 there is no difference in fluorescence lifetime for ceramics and single crystals with the same concentration.

Figure 1.4 shows the absorption spectrum of ceramics and a single crystal. Absorption spectrum keeps its pattern constant with increasing concentration. Peak absorption at 808 nm is shown to increase linearly with concentration [17]. Also from Figure 1.4 it can be observed that there is broadening in absorption lines with increasing concentration. This broadening was pointed out by Dubinskii et al. [14] and increasing rate is in order of nanometers (Figure 1.5).



a)

b)

Figure 1. 2– a) Fluorescence redshift versus neodymium concentration, b) FWHM at 1064 nm versus neodymium concentration [17].

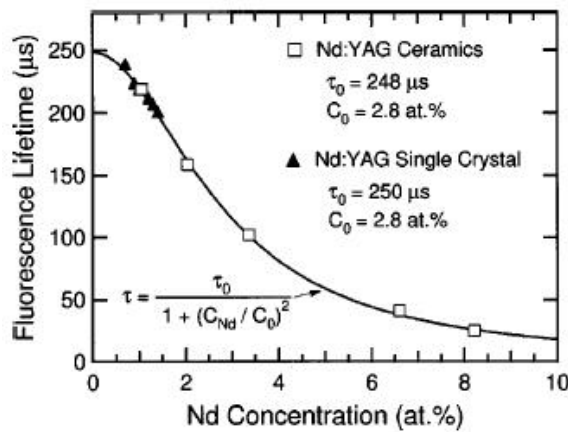


Figure 1.3- Fluorescence lifetime as a function of Nd^{3+} concentration. The open squares show the experimental data for the ceramics and the closed triangles for the single crystals [12].

Lupei et al. [18], showed the possibility of using high concentrated ceramic laser materials with 885 nm pump source. Measurements show that the absorption coefficients of the two peaks of the 885-nm band are approximately equal at room temperature and become appreciable at high Nd concentrations: they increase from $\sim 1.7 \text{ cm}^{-1}$ at 1 at. % Nd to $\sim 6.5 \text{ cm}^{-1}$ at 4 at. % and $13\text{--}14 \text{ cm}^{-1}$ at 9 at. % Nd, while the FWHM increases from $\sim 2.5 \text{ nm}$ at 1 at. % Nd to $\sim 3.2 \text{ nm}$ at 9 at. % Nd. Figure

1.6 [19] shows the absorption spectrum of 1 and 9 at. % Nd concentrated YAG ceramics near 885 nm.

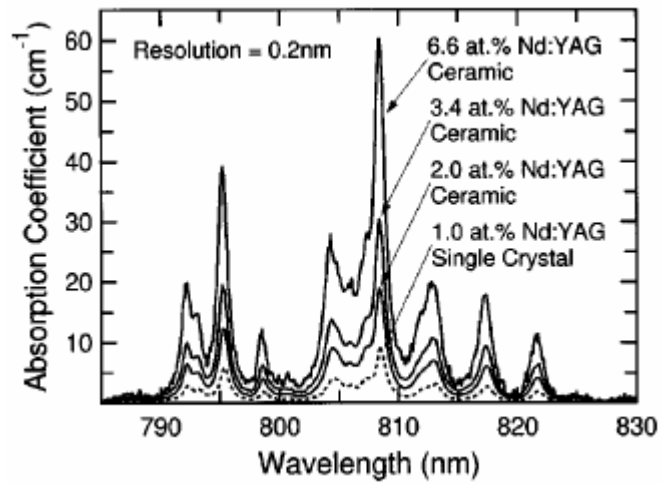


Figure 1. 4- Absorption spectra of 2.0, 3.4, and 6.6 at. % Nd:YAG ceramics (solid curves) and 1.0 at. % Nd:YAG single crystal (dashed curve) [12].

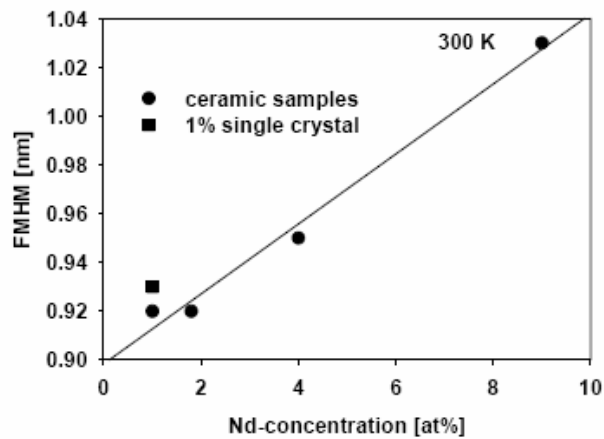


Figure 1. 5 - Concentration-dependent broadening of Nd:YAG absorption lines at 300 °K [14]

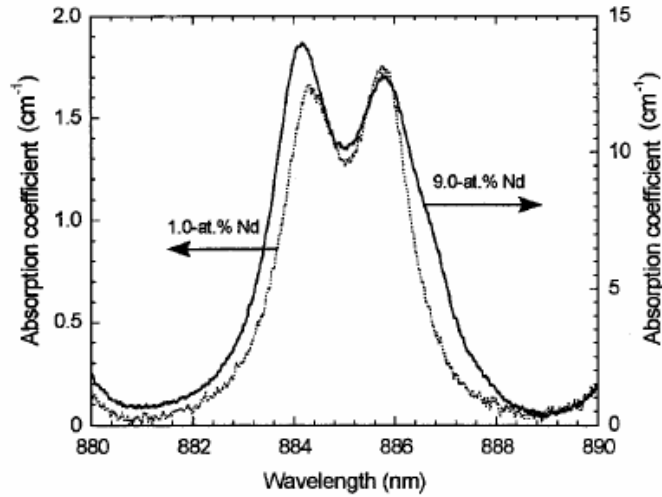


Figure 1. 6- The absorption profile of Nd:YAG ceramics (1.0 and 9.0 at. % doping) at room temperature around 885 nm [19]

1.4 Physical Properties

Physical properties of a material to be considered are density, thermal conductivity, specific heat, Poisson's ratio, Young's modulus and fracture strength.

Density of ceramics is the same as that of single crystals, 4.55 g/cm^3 [3, 20]. In ceramics, porosity is critical factor that should be controlled through the manufacturing process. Ceramics with transparency comparable to single crystals require exceptionally low pore concentration ($<0.001\%$), clean grain boundaries, and no secondary phases [14]. Ikesue et al. [11] demonstrated that a pore volume no greater than 1.5 ppm (i.e., 99.99985% theoretical density) is required to achieve equivalent optical transmission properties to single crystals. In a recent paper, Ikesue [21] reported a ceramic with $50 \mu\text{m}$ grain size and relative density of 99.9999 %.

Thermal conductivity of ceramics was reported to degrade with increase of concentration ratio. The thermal conductivity was measured to be 9.0 W/mK at 20°C at the Nd^{3+} concentration of 6.6 at. % [22], while that of a YAG single crystal was 12.9 W/mK [3]. However, in the technical data sheet of ceramics provided by

Baikowski Co. [20] thermal conductivity is approximately equal to the single crystal one. Yagi et al. [23] investigated thermal conductivity of ceramic YAG at low temperatures (Figure 1.7). Results show that there is a significant decrease in thermal conductivity of ceramics with decrease of temperature. It is observed that ceramics having small grain size have lower thermal conductivity. This implies that increased grain boundaries decrease thermal conductivity. Although there was no information for thermal conductivity at high temperatures, it is observed from Figure 1.7 that the thermal conductivity gets close to each other for single crystal and ceramics of different grain sizes as temperature gets high.

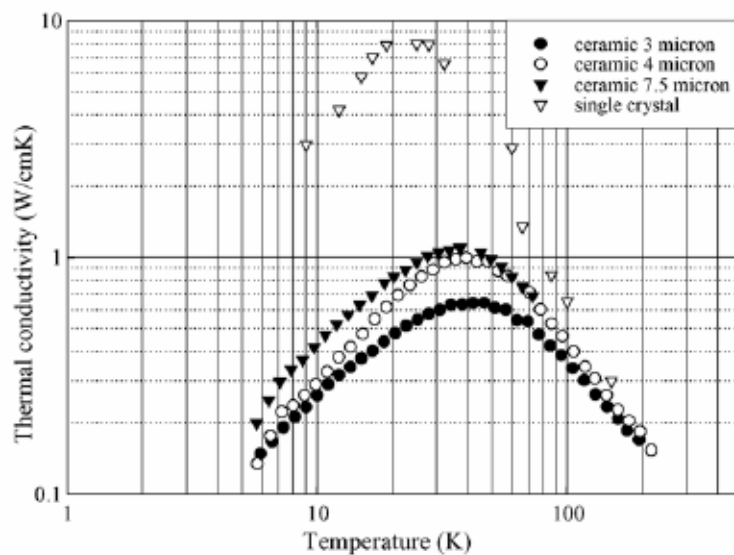


Figure 1.7- The experimental results on the thermal conductivity of the YAG single crystal and polycrystal [23]

Manufacturers of ceramic [20] and single crystal [3] YAG materials give the same value for specific heat of YAG, 590 J/kg °C. Variations in specific heat with temperature or dopant concentrations for ceramics are not reported up to date.

Young's modulus and Poisson's ratio of ceramic YAG is reported by Yagi et al. [23] as a function of temperature. Young's modulus is decreasing with increasing temperature. Results are given for temperatures from 25 °C to 1400 °C with modulus decreasing almost linearly from 308 GPa to 264 GPa respectively.

Reported Poisson's ratio has values between 0.233 and 0.216. However Mezeix et al. [24] reported that at room temperature the Young's modulus and Poisson's ration of a ceramic YAG are 283.6 GPa and 0.226 respectively. This difference may be because of porosity in different samples used.

The fracture strength of ceramic YAG is higher than that of single crystal. Fracture strength of single crystal Nd:YAG is 280 MPa [3]. For ceramics, it is reported to be 307 MPa [20] and 500 MPa [25] and this strength is constant with increasing temperature.

1.5 Laser Performance

Over one decade have passed since Ikesue et. al. [11], first reported the optical quality of ceramic Nd:YAG. Table 1.1 gives the available literature results of lasers using ceramic Nd:YAG as laser material. Output powers of the produced lasers rapidly increased from mW to kW in approximately five years. Pump sources of both 808 and 885 nm have been used. As can be observed from Table 1.1, samples with high concentration are used with 808 nm sources if ceramic thickness is small otherwise 885 nm sources are preferred. For low concentration ceramics, with large size 808 nm pump sources are used. Higher efficiencies were obtained for laser materials with high concentration and 885 nm pump sources. Table 1.1 also lists beam quality factor

M^2 [5] of beams obtained. M^2 measures how far is a beam from TEM_{00} beam, i.e. value of 1.0 indicates that beam is TEM_{00} . For the first time a solid-state laser has operated at 25000 Watts, using a ceramic Nd:YAG laser material [33]. This result indicates that ceramic lasers are candidate for high power solid-state lasers.

Table 1. 1 - Ceramic Laser Reports

Output Power (W)	Slope Efficiency (%)	Optical-Optical Efficiency (%)	Size	% at. Nd	M ²	Pump Wavelength (nm)	Ref.
0.465	57.6	52.7	2.5 mm thickness	2	-	808	[26]
0.380	53	47.6	4.8 mm thickness	1	-	808	[17]
0.090	27.4	-	0.847 mm thickness	3.4	-	808	[12]
31	18.8		φ3mmx100 mm	1	-	808	[27]
72		24.8	φ3mmx104 mm	1	28	808	[28]
236	62	52.5	φ5mmx75mm	1	-	808	[29]
210		48.7	φ3.5mmx87 mm	0.6	18.7	808	[30]
144	67	64	φ1.5mmxφ3mmx41mm	0.3		808	[31]
0.135	42	34	1.5 mm thickness	3.8	1.6x1.6	885	[32]
6	76	66	φ4mmx6mm	2.5	-	885	[33]
25000	-	-	100x100x20	-	-	-	[34]

CHAPTER 2

THERMO-OPTIC EFFECTS

2.1 Introduction

The optical pumping process in a solid-state laser material is associated with the generation of heat for a number of reasons [5]:

- The energy difference of the photons between the pump band and the upper laser level is lost as heat to the host lattice and causes the so called quantum defect heating.
- Similarly, the energy difference between the lower laser level and the ground state is thermalized.
- Since the quantum efficiency of the fluorescence processes involved in the laser transition is less than unity, heating due to quenching mechanism takes place.
- Absorption by the host material also leads to heating.

Generated heat in laser material is a source of thermal distortions. These distortions can be divided in two classes: optical distortions and fluorescence distortions. Optical distortions are thermal lensing, birefringence, and depolarization. Fluorescence distortions are increase in population of lower laser level due to excess heat, degradation in fluorescence intensity and shift in fluorescence wavelength.

The magnitude of the thermal distortion is determined by the amount of heat deposited per unit volume into the laser material. Deposited heat on the other hand is determined by the thermal, mechanical, and optical parameters of the laser material selected, beside the reasons stated above.

Thermal distortions are responsible for laser efficiency decrease and beam quality reductions in laser oscillators and amplifiers. To overcome such problems active laser medium should be cooled effectively.

2.2 Heat Dissipation Factor

Part of the energy absorbed by the active ions in laser material is lost due to the quantum defect, caused by the difference between the absorbed pump and the emitted energy quanta; all this is transformed into heat by interactions with phonons in the upper (the difference between the pump and metastable state energy) or in the lower levels (the difference between the lower laser level and the ground state). The energy transfers that determine the reduction of the emission quantum efficiency, is a source of heating in solid-state laser materials. This effect could be clearly observed in the value of the fractional thermal load, defined as the fraction of the absorbed power that is transformed into heat. In presence of laser emission with wavelength λ_L and with extraction efficiency η_L , the fractional thermal load for Nd:YAG, taking into account the emission quantum efficiency, is given by Lupei et al. [35]

$$\eta_h = 1 - (1 - \eta_L)(1 - 1.82C_{Nd}) \frac{\lambda_p}{\lambda_{av}} - \eta_L \frac{\lambda_p}{\lambda_L} \quad (2.1)$$

where λ_{av} is average fluorescence wavelength, λ_p is pump wavelength and C_{Nd} is the % Nd concentration.

Similar equation is given by Fan [36],

$$\eta_h = 1 - \eta_p \left[(1 - \eta_L) \eta_r \frac{\lambda_p}{\lambda_{av}} + \eta_L \frac{\lambda_p}{\lambda_L} \right] \quad (2.2)$$

where η_p is the pump quantum efficiency, η_r is the radiative quantum efficiency for the upper metastable level.

Comparing the two equations for heat fraction, they look to be very similar. Lupei incorporates concentration in Eq. (2.1) while Fan (Eq. 2.2) gives it as radiative efficiency factor. Fan also incorporates the efficiency of pumped light to be absorbed by active ions in the medium.

These two equations can be used for Q-switched lasers and amplifiers assuming $\eta_L=0$, while for continuous wave (CW) lasers $\eta_L=1$. For CW lasers thermal efficiency factor is the same for both equations. However, either of equations does not encounter nonradiative sites and so there are small differences between calculated and measured data.

Goldring et al. [37] uses the assumption that an excited ion has a probability to decay fluorescently (γ), (α) the probability to decay by stimulated emission and (β) to decay nonradiatively. Sum of the probabilities is equal to 1. γ can be ignored since in CW lasers fraction of pump power is almost equal to fluorescent power. The heat fraction equation can be written as

$$\eta_h = \left(1 - \frac{\lambda_p}{\lambda_L}\right) \alpha + \beta . \quad (2.3)$$

Goldring suggests that β should be found experimentally, by obtaining a value of 8% from his investigations. Fan also reports a factor of 10 % for nonradiative sites. Lupei et al. obtained very similar results for calculated and measured data, since any nonradiative decay is included in the concentration function.

So η_h determines the fraction of absorbed pump power which is responsible for thermal distortion in a laser material.

2.3 Temperature Distribution

In rod shaped laser materials, heat is removed from barrel surface, by a flowing fluid. Starting from steady state heat equation in cylindrical coordinates (2.4) and assuming constant surface temperature and uniform heat generation, equations 2.5 and 2.6 for temperature distribution in the laser rod and rod surface temperature respectively are obtained [38].

$$\frac{1}{r} \frac{d}{dr} \left(r \frac{dT}{dr} \right) + \frac{\dot{q}}{k} = 0 \quad (2.4)$$

$$T(r) = \frac{qr_o^2}{4k} \left(1 - \frac{r^2}{r_o^2} \right) + T_s \quad (2.5)$$

$$T_s = T_\infty + \frac{\dot{q}r}{2h} \quad (2.6)$$

Heat power dissipated in laser rod is given by \dot{q} in watts per volume. T_∞ is used for coolant temperature and h represents convection constant in watts per area time temperature. Convection constant is a function of coolant fluid physical properties, flow tube geometry and flow velocity [8].

Figure 2.1 shows the temperature distribution across the laser rod for different heat powers. Temperature profile has a parabolic distribution with maximum at the center of the rod. Temperature difference between the center and surface of the rod is increasing with increase in heat power.

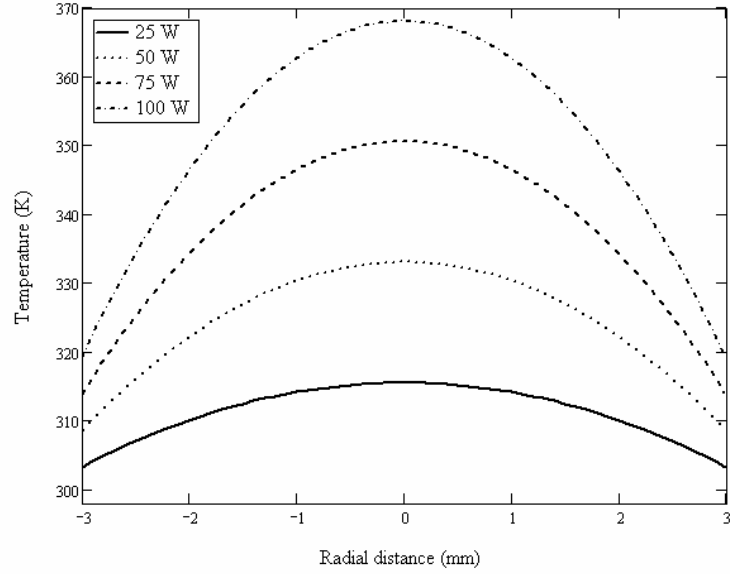


**Figure 2.1– Temperature distribution across the laser rod of f6x50mm
($h=2 \text{ W/cm}^2 \text{ }^\circ\text{K}$, $k=0.13 \text{ W/cm}^\circ\text{K}$, $T_h=298 \text{ }^\circ\text{K}$)**

2.4 Thermal Stresses

The temperature gradients generate mechanical stresses in the laser rod, since the hotter inside volume is constrained from expansion by the cooler outer volume. The stresses in a cylindrical rod, caused by a temperature distribution $T(r)$, can be calculated from the equations given by Timoshenko and Goodier [39]. Radial (σ_r), azimuthal (σ_ϕ) and axial (σ_z) stresses in an isotropic rod with free ends and uniform power density distribution are according to

$$\sigma_r(r) = QS(r^2 - r_o^2) \quad (2.7)$$

$$\sigma_\phi(r) = QS(3r^2 - r_o^2) \quad (2.8)$$

$$\sigma_z(z) = 2QS(2r^2 - r_o^2) \quad (2.9)$$

where the factor $S = \alpha E [16k(1 - \nu)]^{-1}$ contains the material parameters; E is Young's modulus; ν is Poisson's ratio; and α is the thermal coefficient of expansion. The stress components σ_r , σ_ϕ and σ_z represent compression of the material when they are negative and tension when they are positive. As plotted on Figure 2.2 the center of the rod is under compression. The radial component of the stress goes to zero at the rod surface, but the tangential and axial components are in tension on the rod surface. The tensile strength of Nd:YAG is 1800-2100 kg/cm² [5]. It is suggested that in order to avoid thermal fatigues, stress induced in the rod should be five times less than the tensile strength of material [5].

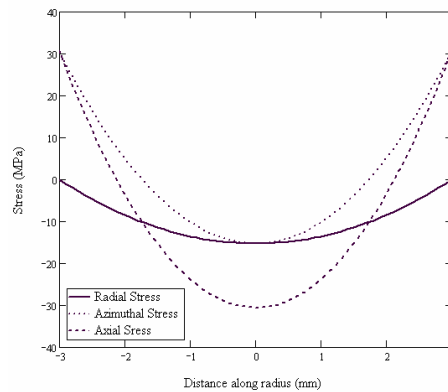


Figure 2. 2– Radial, azimuthal and axial stress components within Nd:YAG crystal rod as a function of radial distance

2.5 Stress Birefringence

When an optical isotropic material is subjected to stress, it becomes anisotropic optically. The change of the refractive index is called stress birefringence

or photo-elastic effect. The refractive index of a crystal is specified by the optical indicatrix, an ellipsoid whose coefficients are the components of the relative impermeability tensor [40]

$$\sum_{i,j=1}^3 B_{i,j} x_i x_j = 1. \quad (2.10)$$

The impermeability tensor components B_{ij} are given by

$$B_{ij} = \frac{1}{n_{ij}^2} \quad (2.11)$$

where n_{ij} are the indices. Unstressed indices are given by

$$B_{0,ij} = \frac{1}{n_{0,ij}^2}. \quad (2.12)$$

For YAG (a cubic material) which is optically isotropic in absence of stress, $n_{0,11}=n_{0,22}=n_{0,33}$ with all other $n_{0,ij}=0$. Changes in the index of refraction are specified using the difference between the unstressed and stressed impermeability components using

$$B_{ij} = B_{0,ij} + \sum_{i,j,k,l=1}^3 \pi_{ijkl} \sigma_{kl}, \quad [40] \quad (2.13)$$

where the π is the forth-rank piezo-optic coefficients and σ are the stress components.

Following the equations above will reveal the result that there will be different indices in each principal direction. Laser materials with rod shape will

exhibit different indices of refraction n_r and n_ϕ for radially and azimuthally polarized light respectively. If a linearly polarized light (in y -direction) is incident on such a laser material, the field vector will have different components in radial and azimuthal direction and relative amplitudes of the two components will depend on azimuthal and radial coordinates (Figure 2.3).

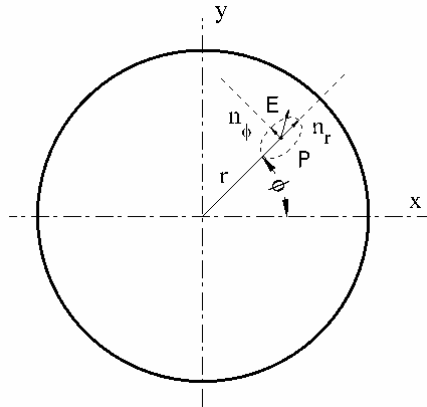


Figure 2.3 – State of refractive index in rod shaped material

2.6 Refractive Index Distribution

In rod shaped laser materials there are two distinct contributions to refractive index changes that occur when significant heating of the material is present. The first is the change in refractive index with temperature. Because the temperature of a YAG rod varies with radial distance (Figure 2.1) then so will the index of refraction. The second contribution arises from the stresses or strains that occur in solid-state laser materials. Stresses and strains also vary with radial distance, so will their contribution to the refractive index.

Total index of refraction can be written as

$$n_{r,\varphi}(r) = n_o + \Delta n_T(r) + \Delta n_{S_{r,\varphi}}(r) \quad (2.14)$$

where Δn_T is index contribution of temperature difference and $\Delta n_{S_{r,\varphi}}$ is index contribution of stress with corresponding birefringence component. Temperature contribution is given by

$$\Delta n_T(r) = [T(r) - T_s] \left(\frac{dn}{dT} \right) \quad (2.15)$$

where $\frac{dn}{dT}$ is temperature variation coefficient of refractive index. Stress contribution can be approximated by

$$\Delta n_{S_{r,\varphi}} = -\frac{n^3}{2} \pi_{ijkl} \sigma_{kl} . \quad (2.16)$$

Brown [41] derived equations of contributions to refractive index for radial and azimuthally polarized light for a rod with uniformly dissipated heat as

$$\Delta n_r(r) = \frac{dn}{dT} \left(\frac{Qr}{2h} + \frac{Qr^2}{4k} \right) - \frac{Q}{4k} \frac{dn}{dT} r^2 - \frac{n_o^3}{2} [\pi_{11}\sigma_r(r) + \pi_{12}\sigma_\varphi(r) + \pi_{13}\sigma_z(r)] \quad (2.17)$$

$$\Delta n_\varphi(r) = \frac{dn}{dT} \left(\frac{Qr}{2h} + \frac{Qr^2}{4k} \right) - \frac{Q}{4k} \frac{dn}{dT} r^2 - \frac{n_o^3}{2} [\pi_{12}\sigma_r(r) + \pi_{11}\sigma_\varphi(r) + \pi_{13}\sigma_z(r)] \quad (2.18)$$

respectively.

2.7 Depolarization

Birefringence induced in laser rod due to thermal stress is a source of loss for a laser operating with linearly polarized beam. In such lasers polarization selective optical elements are used in order to obtain linearly polarized light. When a linearly polarized light passes through laser medium that has birefringence, there will be phase difference between the components of polarization vector along the principal axes of the pumped laser material given by

$$\delta = \frac{2\pi}{\lambda} L(\Delta n_{\phi} - \Delta n_r). \quad (2.19)$$

Rate of depolarization at a point in laser material is given by

$$d(r, \phi) = \sin^2(2\phi) \sin^2\left(\frac{\delta}{2}\right) \quad (2.20)$$

where, λ is the wavelength of laser beam, L is the length of material, Δn_{ϕ} and Δn_r are the azimuthal and radial index change given in cylindrical coordinate system. Total depolarization across a rod shaped laser material is given by

$$D_b(r) = \frac{1}{\pi r^2} \int_0^r \int_0^{2\pi} d(r', \phi) d\phi dr'. \quad (2.21)$$

$D_b(r)$ gives the fraction of laser power that is reflected out of the resonator by a polarization selective optical element.

2.8 Thermal Lens Effect

The thermal lens is formed by heating in the laser rod. This heating causes a temperature gradient and a stress distribution in the rod. The effect of the stress is to bend the end face of the rod into an approximately parabolic shape giving the rod the properties of a spherical lens. The temperature gradient causes a refractive index gradient along the radius of the crystal resulting in a gradient-index (GRIN) lens. In the case of a homogeneously pumped rod the bending effect will be present at both ends of the rod resulting in a thick lens - a combination of a spherical lens formed by the end effects and a GRIN lens formed by the temperature gradient.

Focal length of a pumped laser rod is given by

$$f_{r,\phi} = \frac{1}{Q} \frac{k}{L} \left(\frac{1}{2} \frac{dn}{dT} + \alpha C_{r,\phi} n_o^3 + \frac{\alpha r_o (n_o - 1)}{L} \right)^{-1} \quad [5], \quad (2.22)$$

In *Eq. 3.1*, $C_{r,\phi}$ [5] is a result of birefringence properties of the Nd:YAG crystal. So two existing polarization in the lasing medium will be subject to two different refractive indices, which means that there will be two different focal lengths separated by 90°.

First term in *Eq. 2.1* is the effect of GRIN lens, second term is the effect of birefringence and the third term is the rod end effect. All these three constituents of thermal lens should be considered in optically pumped laser rods.

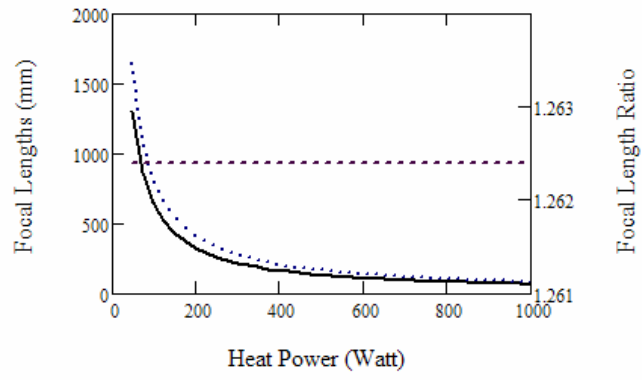
Figure 2.4 depicts the behavior of thermal lens concerning heating power, crystal length and crystal radius. Keeping crystal dimensions constant and increasing heat power there is a decrease of focal length as plotted on Figure 2.4a.

Keeping heat power constant and decreasing the length of crystal is crucial since focal length is decreasing, however increasing the length does not effect focal length much as can be understood from Figure 2.4b. On the other hand, keeping

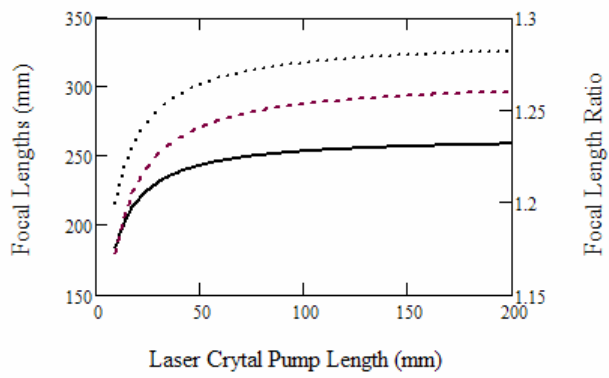
crystal length and heating power constant and increasing laser rod radius increases the focal length as depicted on Figure 2.4c.

Ratio of the focal lengths of the two polarizations is always far from unity, which implies that there is always an astigmatic beam in rod shaped solid-state lasers. Only by increasing diameter and decreasing the length of a laser rod, focal lengths ratio gets closer to unity.

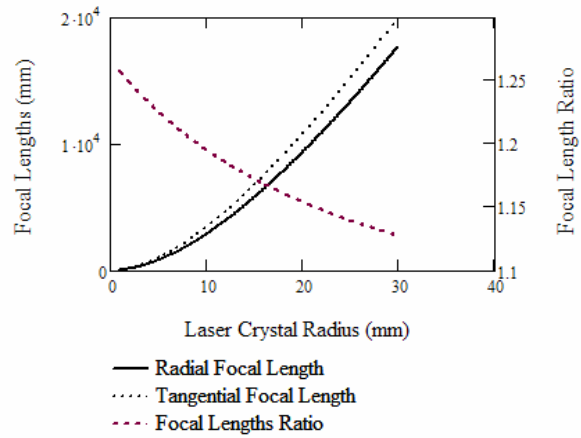
As a result, to have large focal lengths we should have less heat power, long laser rods with large diameters.



a)



b)



c)

Figure 2. 4 – Laser rod focal length dependence on a) heat power, b) crystal length and c) crystal radius

CHAPTER 3

ABSORBED POWER DISTRIBUTION

3.1 Introduction

In analytical analysis of laser material frequently it is assumed that absorbed power is uniformly distributed through the volume. Previous equations used in calculation of temperature and stress distribution are obtained also by the assumption of uniform power distribution. Therefore, thermal lens and depolarization are also the result of this assumption.

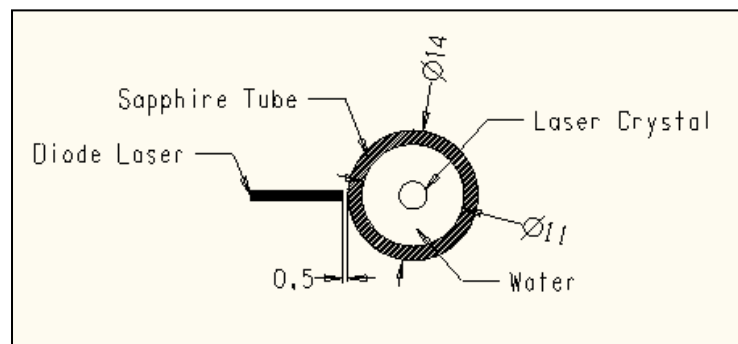
In reality, a material absorbs radiation according to Beer's Law (3.1) and absorbed power decays exponentially in the direction of pump beam propagation. Also in case of pumping with laser diode, the intensity distribution of pump beam and location of pump source also has effect on the absorbed power distribution.

In the following sections, the method used for calculating the power distribution across a rod shaped material will be presented. Results for two different rod radii materials, with four different pump structures and two different pump sources are given.

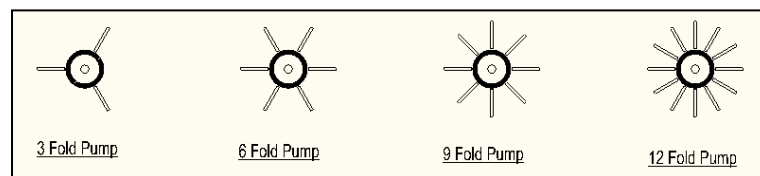
3.2 Pump Structure

In the analysis, we have assumed a flow tube with 5.5 mm inner and 7 mm outer radius. Pumping diodes are placed just 0.5 mm apart from the outer surface of the flow tube. Four different pumping structures, 3, 6, 9 and 12-fold pumping and two different rod diameters, 3 mm and 6 mm, have been considered. Laser rods have a length of 50 mm and all are side pumped as shown in Figure 3.1. Tube material is assumed to be made of sapphire. Sapphire has a lower index of refraction and a lower absorption coefficient compared to quartz, which is frequently used as tube material. In addition, sapphire has large fracture strength and chemical durability. However, it is expensive compared to quartz.

Tube structure and diode tube spacing are kept the same for the two different rods in order to eliminate the change in the beam profiles in the pump structure.



a)



b)

Figure 3. 1- Model Used for the analysis

3.3 Pump Source

In selection of pump source, the following criteria should be considered:

- Pump wavelength should be near or identical to one of the absorption peaks of laser material
- FWHM of pump wavelength should be equal or less than the FWHM of absorption peak pumped
- In order to decrease quantum defect loss, pump wavelength should be close to emission wavelength of laser material pumped

Most popular source for pumping Nd:YAG material is 808 nm diode laser. Another source is 885 nm diode, importance of which has increased with the success in production of highly doped ceramic laser materials.

In this study absorbed power distribution has been calculated for two different pump wavelengths, 808 nm and 885 nm. Figure 3.2 gives the absorption coefficient for both wavelengths as a function of Nd³⁺ %at. concentration. Analyses have been carried out for six different C_{Nd} % at. ratios, 0.6, 1.0, 2.0, 3.0, 4.0 and 6.0.

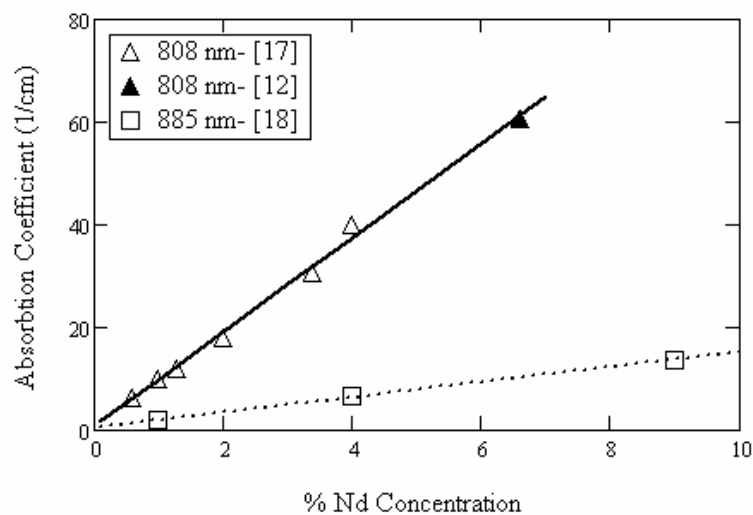


Figure 3. 2 - Absorption coefficients of ceramic Nd:YAG for 808 nm and 885 nm

For both wavelengths, absorption coefficient linearly increases with increasing dopant concentration. Absorption coefficients for 808 nm are higher than the coefficients for 885 nm. So, 808 nm beams will be absorbed in shorter distances, while 885 nm sources will travel longer distances in material before they are absorbed efficiently.

Beam intensity of diode lasers is assumed to possess a Gaussian distribution in the plane perpendicular to the rod axis and no variation is assumed in the direction of rod axis. Divergence angle of pump beam is assumed to be 30° with an emitting thickness of 1 micron. In addition, polarization of pump source is assumed to be parallel to the plane of incidence, i.e. in the plane perpendicular to the direction of rod axis.

3.4 Ray Tracing

Ray tracing pattern is obtained by assumption that all rays travel in the plane perpendicular to rod axis. Assumed beam profile is divided in s number of individual rays (Figure 3.3). Each ray has its own slope and starting height. First ray (r_0) and the last ray (r_{s-1}) have angles that are equal to half of the angle of divergence of the pump source. Heights of the two beams are equal to the half of the emitting source thickness. The rays that are emerging between the first and last ray have angles decreasing by a factor equal to the source divergence angle divided by the ray number. Ray heights also decrease by a factor equal to the source thickness divided by the ray number.

To determine the actual pattern of pump light in the rod, each ray is traced individually by using the Snell's law together with geometry. In Figure 3.4 traced rays are shown for 3 mm and 6 mm rods. Ray tracing outside the rod was not performed since it is not in the scope of the analysis. Reflected rays, except the rays

that reflect from the internal surface of the rod, are not traced. Each ray has four passes through the rod, one is refracted and the other three are reflected rays.

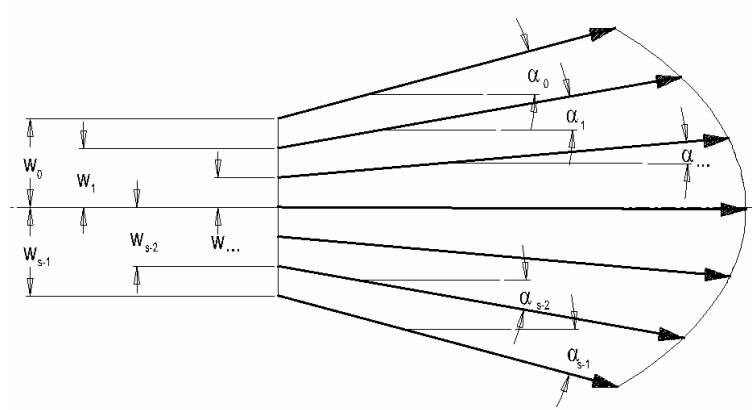


Figure 3.3 – Ray discretization for ray tracing

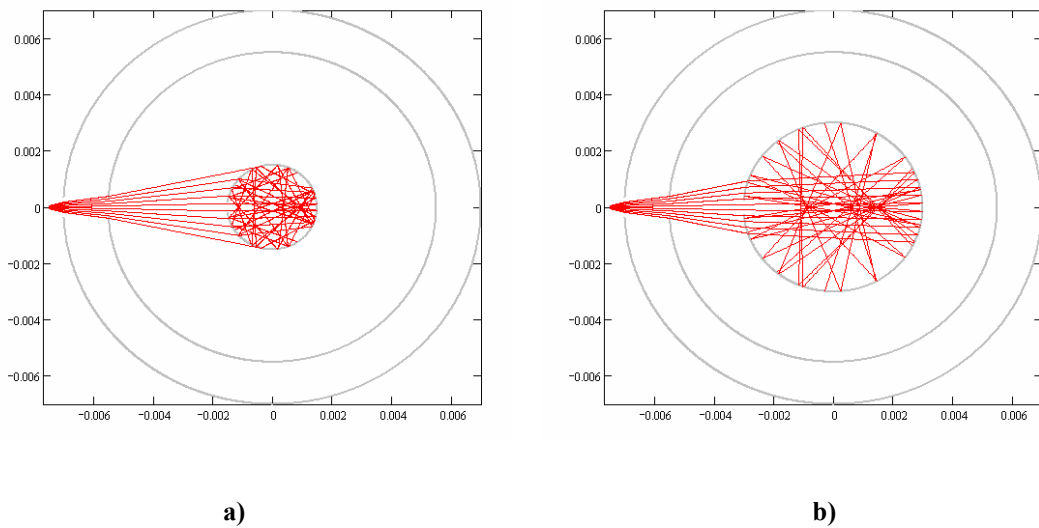


Figure 3.4 – Ray tracing results; a) 3 mm rod, b) 6 mm rod

3.5 Absorption

Distribution of absorbed power in the laser rod was determined from ray tracing pattern. Intensity distribution of a pump source, which is assumed to be Gaussian, is discretized as shown in Figure 3.5. Thus, each ray is assigned a power. Assuming that absorption of radiation obeys Beer's law (3.1) and that the intensity is distributed among the reflected and refracted beams at each surface according to Fresnel's equations (3.2), distribution of absorbed pump power can be obtained by using Eq.3.3. Coefficients of reflections are calculated for parallel polarization (TM wave) using Fresnel's equations.

$$I(x) = I_o e^{-\alpha x} \quad (3.1)$$

$$R = \frac{n_1 \cos(\theta_i) - n_2 \cos(\theta_t)}{n_1 \cos(\theta_i) + n_2 \cos(\theta_t)} \quad (3.2)$$

$$\rho(x) = \frac{I_o \chi e^{-\alpha x} (1 - e^{-\alpha \Delta x})}{(\Delta x)^3} \quad (3.3)$$

Where I_o is initial power for each ray traced, $I(x)$ is power at location x , R is coefficient of reflected light at any surface, α is the absorption coefficient at location x , n_1 index of refraction of incident ray medium, n_2 index of refraction of the transmitted ray medium, θ_i and θ_t are angles that incident and transmitted ray made with the surface normal respectively. χ is $(1-R^2)$ or R^2 for external or internal reflection respectively. $\rho(x)$ is power density at location x in power per volume. x is local coordinate in direction of ray trajectory.

Rod cross section is divided into squares (Figure 3.6a) and a power was calculated for each square using Eq. 3.3. Corresponding to the grid given in Figure 3.6a a matrix (Figure 3.6b) that contains powers absorbed at each square of the rod

cross section was formed. This matrix represents the power distribution due to a single source. In the pump structures of laser rods considered in this study, there are 3, 6, 9 and 12 fold pump source distributions. To obtain the distributions corresponding to these structures the matrix of single source is rotated by a proper angle and rotated matrices are summed to obtain the desired distribution. The procedure is illustrated in Figure 3.7 for the three-fold structure.

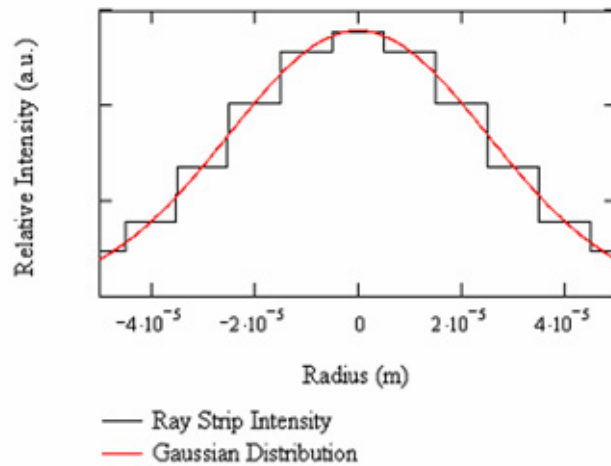


Figure 3. 5 – Intensities assigned to each individual ray

Matrix rotation is performed around the center point of the rod (matrix) and each rotated matrix has the same size and total power. This ensures that the sources at all folds are identical.

Total power absorbed by the rod is the same in each pump structure. So in each pump structure, a single pump source has a power that is equal to total pump power divided by the fold number.

Calculated power distributions are plotted as shown in Tables A2.1-4. In each table, rows represent corresponding Nd % at. concentration, while columns represent the pump structure. It should be noted that absorbed power density plots given in the following tables are independent from pump power value, i.e. they represent the normalized power densities. As can be observed from these four tables

pump structure has an evident impact on the absorbed pump power distribution. Also absorption coefficient determines the effective pump length in the material.

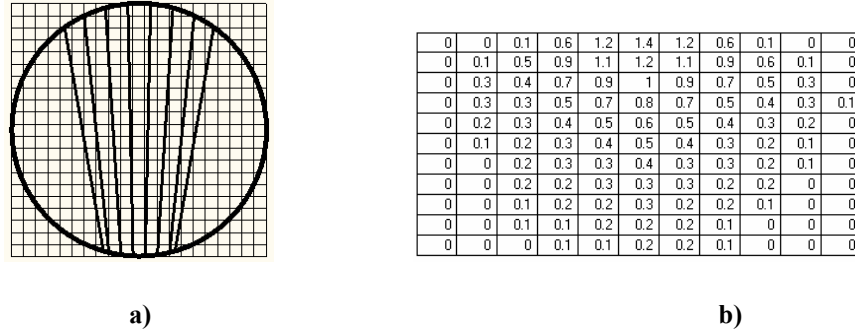


Figure 3. 6 – Grid used in power distribution calculations (a) , b)representative power matrix for 11x11 grid

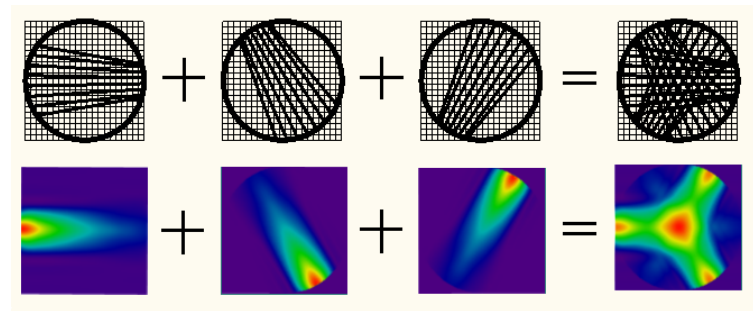
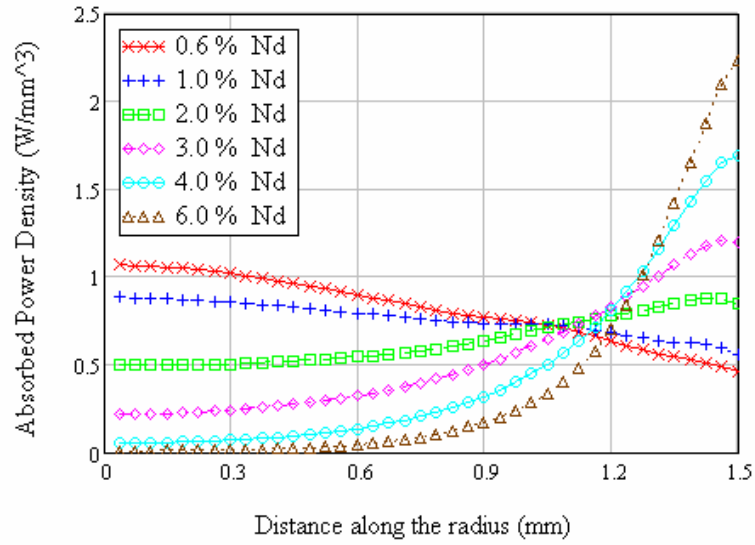


Figure 3. 7 – Step wise power density matrix construction

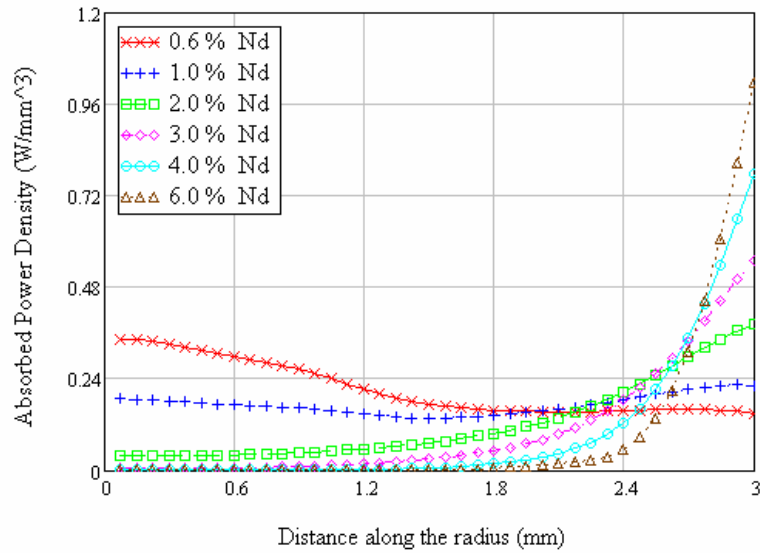
Power density distributions of 3 mm and 6 mm rods pumped with the 808 nm source are given in Tables A2.1 and Table A2.2, respectively. As can be observed from these tables, as Nd % at. concentration increases, the high power density regions (in red) move toward the outer surface of the rod. This situation facilitates the heat removal process, but from lasing point of view, makes it difficult to obtain beams with Gaussian profile or uniform intensity. This observation is not valid for the rods pumped with 885 nm source (Table A2.3, Table A2.4). Both rods (3 mm and 6 mm) can be pumped up to high concentration without any unpumped region in the rod centre by 885 nm pump source.

It can be concluded that 808 nm pump sources are suitable for low concentration large size materials or for laser materials with small size and high dopant concentration. On the other hand 885 nm sources are suitable for large size high concentration laser materials.

Figures 3.8 and 3.9 give the radial variation of absorbed power density. Each rod has its own distribution that will affect the beam quality of laser obtained.

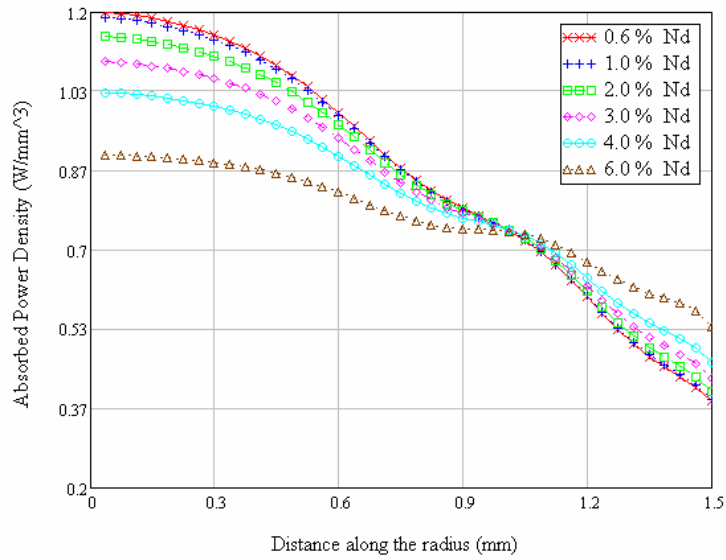


a)

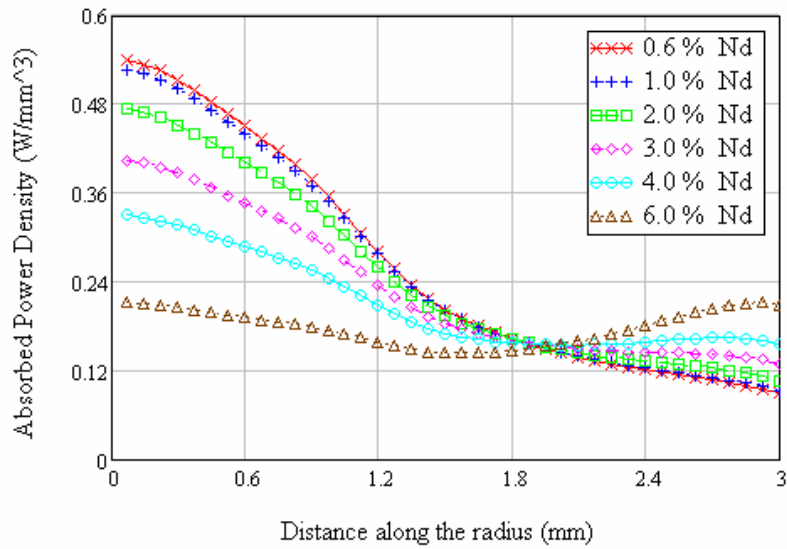


b)

Figure 3. 8– Absorbed power density distributed along the radius of rod a) 3 mm and b) 6 mm using 808 nm pump source



a)



b)

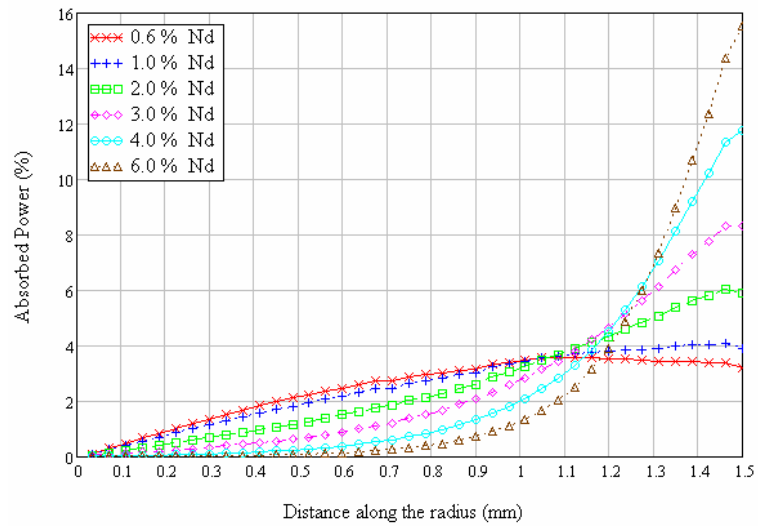
Figure 3. 9 - Absorbed power density distributed along the radius of rod a) 3 mm and b) 6 mm using 885

In the rods considered (3 mm and 6 mm), distribution of pump power beside power density is also important. Figure 3.10 and Figure 3.11 give the percentage of absorbed power as a function of radial distance. Using Eq. 3.4 power absorbed in a

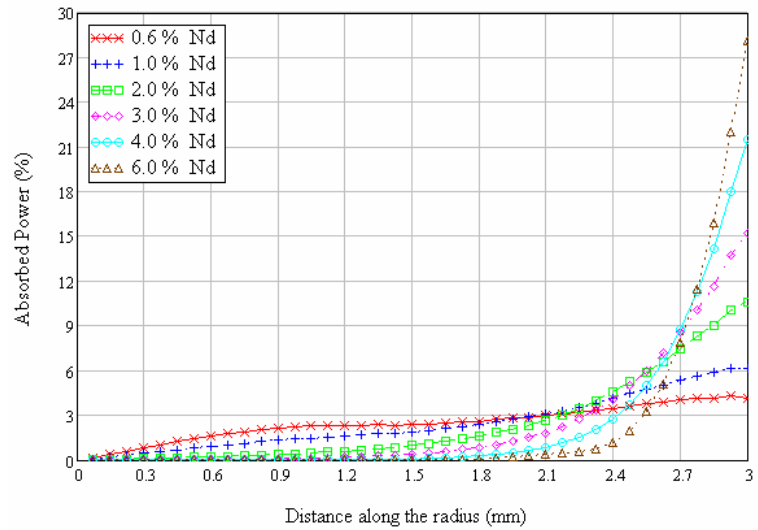
shell of thickness Δr is calculated. Related figures are plotted by dividing the calculated power by total absorbed power.

$$P(r) = \int_0^L \int_0^{2\pi} \int_{r-\frac{\Delta r}{2}}^{r+\frac{\Delta r}{2}} \rho(r, \theta) r dr d\theta dz \quad (3.4)$$

As can be observed from Figures 3.10 and 3.11, in 808 nm pumped rods power is accumulated near the rod surface where in 885 nm source pumped rods most of the power is located in the inner parts of the rods.

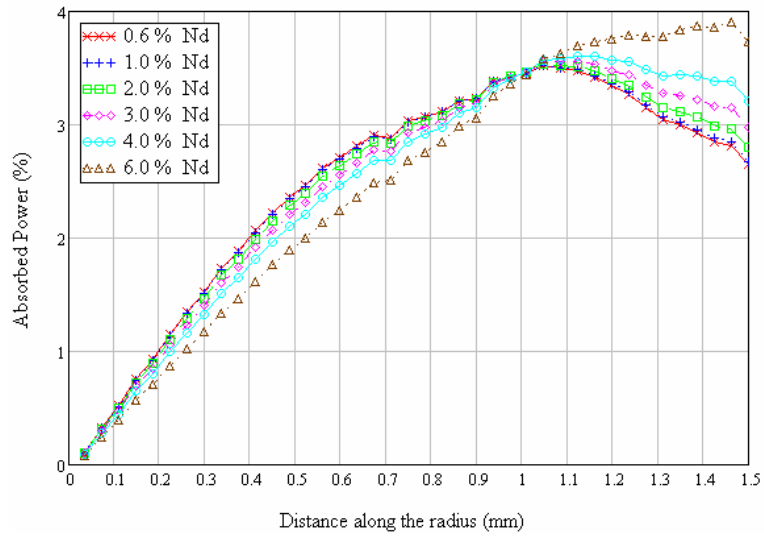


a)

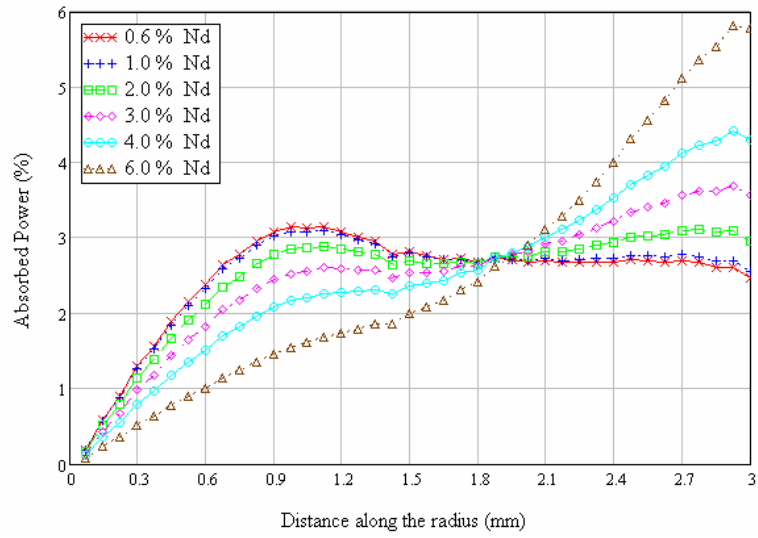


b)

Figure 3. 10 – Percent of absorbed power distributed along the radius of rod a) 3 mm and b) 6 mm using 808 nm pump source



a)



b)

Figure 3. 11 - Percent of absorbed power distributed along the radius of rod a) 3 mm and b) 6 mm using 885 nm pump source

CHAPTER 4

THERMO-ELASTICITY ANALYSIS

4.1 Introduction

Absorbed pump power in a laser crystal is the source of heat generation in a laser material. Although in Chapter 2, absorbed power was assumed to be uniformly distributed through the material volume, in Chapter 3 it was shown that absorbed power has nonuniform variations in a rod shape laser materials.

Also material properties of Nd:YAG are not constant but a function of temperature.

Temperature-dependent material properties and spatial variation of absorbed power introduce nonlinearities in temperature and stress equations. These nonlinearities make it impossible to solve these governing equations analytically. In order to obtain a solution, numerical methods should be used. In this study, finite element analysis (FEA) method is used to calculate temperature, thermal gradient and stress distributions in the laser rods pumped. In the following sections, we develop the mathematical model used for the calculation of the aforementioned distributions. The results obtained are then presented and discussed.

4.2 Heat Equation

General heat equation in cylindrical coordinates is given by Eq. 4.1 [38] as

$$\frac{1}{r} \frac{\partial}{\partial r} \left(kr \frac{\partial T}{\partial r} \right) + \frac{1}{r^2} \frac{\partial}{\partial \phi} \left(k \frac{\partial T}{\partial \phi} \right) + \frac{\partial}{\partial z} \left(k \frac{\partial T}{\partial z} \right) + \dot{q} = \delta c_p \frac{\partial T}{\partial t} , \quad (4.1)$$

where r , ϕ and z are radial, azimuthal and axial distances in cylindrical coordinate system, respectively. In addition, T is temperature, k is heat conduction coefficient, δ is material density, c_p is specific heat and \dot{q} is volumetric power generation.

Since our calculations are for continuous wave (cw) lasers and we assume no absorbed power variation in the rod axis direction (z direction) Eq. 4.1 can be written as

$$\frac{1}{r} \frac{\partial}{\partial r} \left(kr \frac{\partial T}{\partial r} \right) + \frac{1}{r^2} \frac{\partial}{\partial \phi} \left(k \frac{\partial T}{\partial \phi} \right) + \dot{q} = 0 \quad (4.2)$$

Also we should include the temperature dependence of heat conduction coefficient k , and coordinate dependence of absorbed power density. In this case, heat equation has a form of

$$\frac{1}{r} \frac{\partial}{\partial r} \left(k(T(r, \phi)) r \frac{\partial T(r, \phi)}{\partial r} \right) + \frac{1}{r^2} \frac{\partial}{\partial \phi} \left(k(T(r, \phi)) \frac{\partial T(r, \phi)}{\partial \phi} \right) + \eta_h \rho(r, \phi) = 0 , \quad (4.3)$$

where η_h is heat dissipation factor and $\rho(r, \phi)$ is absorbed power density per volume.

In order to solve Eq. 4.3 boundary conditions should be imposed. Rods are cooled from their barrel surface with a flowing liquid coolant (water in our case). Boundary conditions on the barrel surface are given by

$$\frac{\partial T(r, \phi)}{\partial \phi} = -\frac{h}{k(T(r, \phi))}(T(r, \phi) - T_\infty), \quad \text{at } r = r_o. \quad (4.4)$$

$$\frac{\partial T(r, \phi)}{\partial r} = -\frac{h}{k(T(r, \phi))}(T(r, \phi) - T_\infty), \quad \text{at } r = r_o.$$

Since Eq. 4.3 is nonlinear in both temperature and coordinate basis, analytical solutions are difficult to obtain, however numerical solutions are possible and easier.

4.3 Elasticity Equations

Stress equations of equilibrium in cylindrical coordinates are given by

$$\frac{\partial \sigma_{rr}}{\partial r} + \frac{1}{r} \frac{\partial \sigma_{\phi r}}{\partial \phi} + \frac{\partial \sigma_{zr}}{\partial z} + \frac{\sigma_{rr} - \sigma_{\phi\phi}}{r} + F_r = 0$$

$$\frac{\partial \sigma_{r\phi}}{\partial r} + \frac{1}{r} \frac{\partial \sigma_{\phi\phi}}{\partial \phi} + \frac{\partial \sigma_{z\phi}}{\partial z} + 2 \frac{\sigma_{r\phi}}{r} + F_\phi = 0 \quad [42] \quad (4.5)$$

$$\frac{\partial \sigma_{rz}}{\partial r} + \frac{1}{r} \frac{\partial \sigma_{\phi z}}{\partial \phi} + \frac{\partial \sigma_{zz}}{\partial z} + \frac{\sigma_{rz}}{r} + F_z = 0.$$

where $\boldsymbol{\sigma}$ and \mathbf{F} are the stress and force, respectively in the corresponding direction.

Strain equations are given by

$$2 \frac{\partial^2 (r \varepsilon_{r\phi})}{\partial r \partial \phi} = \frac{\partial^2 \varepsilon_{rr}}{\partial \phi^2} + r \frac{\partial^2 (r \varepsilon_{\phi\phi})}{\partial r^2} - r \frac{\partial \varepsilon_{rr}}{\partial r}$$

$$2 \frac{\partial^2 \varepsilon_{zr}}{\partial r \partial z} = \frac{\partial^2 \varepsilon_{zz}}{\partial r^2} + \frac{\partial^2 \varepsilon_{rr}}{\partial z^2}$$

$$2 \frac{\partial^2 (r \varepsilon_{\phi z})}{\partial \phi \partial z} = r^2 \frac{\partial^2 \varepsilon_{\phi\phi}}{\partial z^2} - 2r \frac{\partial \varepsilon_{zr}}{\partial z} + r \frac{\partial \varepsilon_{zz}}{\partial r} + \frac{\partial^2 \varepsilon_{zz}}{\partial \phi^2}$$

[42] (4.6)

$$\frac{\partial}{\partial z} \left(-\frac{\partial \varepsilon_{r\phi}}{\partial z} + \frac{1}{r} \frac{\partial \varepsilon_{zr}}{\partial \phi} + \frac{\partial \varepsilon_{\phi z}}{\partial r} \right) = \frac{\partial^2}{\partial r \partial \phi} \left(\frac{\varepsilon_{zz}}{r} \right) + \frac{1}{r} \frac{\partial \varepsilon_{\phi z}}{\partial z}$$

$$\frac{\partial}{\partial \phi} \left(\frac{\partial \varepsilon_{r\phi}}{\partial z} - \frac{1}{r} \frac{\partial \varepsilon_{zr}}{\partial \phi} + \frac{\partial \varepsilon_{\phi z}}{\partial r} \right) = \frac{\partial^2 (r \varepsilon_{\phi\phi})}{\partial r \partial \phi} - \frac{\partial \varepsilon_{rr}}{\partial z} - \frac{1}{r} \frac{\partial \varepsilon_{\phi z}}{\partial \phi}$$

$$\frac{\partial}{\partial r} \left(\frac{\partial \varepsilon_{r\phi}}{\partial z} + \frac{1}{r} \frac{\partial \varepsilon_{zr}}{\partial \phi} - \frac{\partial \varepsilon_{\phi z}}{\partial r} \right) = \frac{1}{r} \frac{\partial^2 \varepsilon_{rr}}{\partial \phi \partial z} - \frac{2}{r} \frac{\partial \varepsilon_{r\phi}}{\partial z} + \frac{\partial}{\partial r} \left(\frac{\varepsilon_{\phi z}}{r} \right)$$

where $\boldsymbol{\varepsilon}$ is the strain in corresponding direction.

The constitutive equations (Hook's Law) for a homogeneous, isotropic body in cylindrical coordinate system are

$$\varepsilon_r = \frac{1}{E} [\sigma_r - \nu(\sigma_\phi + \sigma_z)] + \alpha\tau,$$

$$\varepsilon_\phi = \frac{1}{E} [\sigma_\phi - \nu(\sigma_r + \sigma_z)] + \alpha\tau,$$

$$\varepsilon_z = \frac{1}{E} [\sigma_z - \nu(\sigma_r + \sigma_\phi)] + \alpha\tau,$$

$$\varepsilon_{r\phi} = \frac{1+\nu}{E} \sigma_{r\phi}, \quad \varepsilon_{\phi z} = \frac{1+\nu}{E} \sigma_{\phi z}, \quad \varepsilon_{zr} = \frac{1+\nu}{E} \sigma_{zr} \quad [42], \quad (4.7)$$

where $\tau = T - T_0$.

In analysis plain strain approximation is applied since we have rod radius that is less than the rod length. So, 3D structure is reduced to 2D. Also $\varepsilon_{rz} = 0$, $\varepsilon_{\phi z} = 0$, $\varepsilon_{zz} = \varepsilon_0$, and our equation are now given by

Equilibrium stress equations

$$\frac{\partial \sigma_{rr}}{\partial r} + \frac{1}{r} \frac{\partial \sigma_{\phi r}}{\partial \phi} + \frac{\sigma_{rr} - \sigma_{\phi\phi}}{r} + F_r = 0$$

$$\frac{\partial \sigma_{r\phi}}{\partial r} + \frac{1}{r} \frac{\partial \sigma_{\phi\phi}}{\partial \phi} + 2 \frac{\sigma_{r\phi}}{r} + F_\phi = 0$$

$$\frac{\partial \sigma_{zz}}{\partial z} = 0 \quad (4.5)$$

Strain equations,

$$2 \frac{\partial^2 (r \varepsilon_{r\phi})}{\partial r \partial \phi} = \frac{\partial^2 \varepsilon_{rr}}{\partial \phi^2} + r \frac{\partial^2 (r \varepsilon_{\phi\phi})}{\partial r^2} - r \frac{\partial \varepsilon_{rr}}{\partial r}$$

Hook's Law,

$$\varepsilon_r = \frac{1}{E} [\sigma_r - \nu(\sigma_\phi + \sigma_z)] + \alpha \tau ,$$

$$\varepsilon_\phi = \frac{1}{E} [\sigma_\phi - \nu(\sigma_r + \sigma_z)] + \alpha \tau ,$$

$$\varepsilon_z = \frac{1}{E} [\sigma_z - \nu(\sigma_r + \sigma_\phi)] + \alpha \tau ,$$

$$\varepsilon_{r\phi} = \frac{1+\nu}{E} \sigma_{r\phi} ,$$

To obtain a solution for thermo-elastic problem differential equations of equilibrium together with compatibility equation, the generalized Hook's law and boundary conditions should be solved.

Generalized Hook's law is also temperature dependent as material properties like Young's modulus of elasticity, Poisson's ratio and thermal expansion coefficient.

From the governing equations for stress, it is evident that to obtain results close to the real, thermal and elasticity equations should be solved simultaneously.

4.4 Finite Element Analysis

Numerical analysis are performed using the commercial FEA software ANSYS[®]. Newton-Raphson method is utilized through nonlinear analysis. 2D couple field element PLANE 13 [43] with four degree of freedom is selected to discretize the system. Each node has 2 structural (UX and UY) and one temperature degree of freedom. Plain strain solution type is selected for structural analysis. Models used in the analysis have 14583 nodes and 28764 elements. Model boundary conditions are given in Table 4.1. Material properties used in the analysis are given in Appendix 1. Nodal heat generation loads are applied using absorption power density distributions obtained in Chapter 3 and multiplied by heat coefficient defined by the pump and the stimulated emission wavelength. Heat coefficients are 0.241 and 0.168 for 808 nm and 885 nm pump sources, respectively.

Table 4. 1– Boundary conditions

Boundary Condition Type	Thermal	Convection coefficient on barrel surface	2 kW/m ² K
		Temperature of coolant fluid	298 K
		Material initial Temperature	298 K
	Structural	Pressure on barrel surface	2 kg/cm ²

4.5 Results

4.5.1 Temperature distributions

Results of temperature distribution in the rods are given in Tables A3.1 to A3.4. Temperature distribution is not dependent on azimuthal coordinate for rods pumped with 885 nm sources (Table A3.3 and Table A3.4). However, rods pumped with 808 nm sources have dependence on azimuthal coordinate with 3 and 6 fold pump structure. This dependence increases with increasing % at. Nd dopant concentration. As observed from these tables, with increase in dopant concentration area of maximum temperature (in rod central parts) is increasing and this means a decrease in thermal gradient in these parts.

Maximum temperatures developed in the rods are plotted as a function of dopant concentration in Figure 4.1. From the figure, it is observed that there is decrease in maximum temperature with increasing dopant concentration. There is no effect of pump structure on maximum temperature generated in rods pumped with 885 nm sources (Figures 4.1c and 4.1d). But this not the case for 808 nm pumped ones. For 3 mm rod at 6 % at. Nd concentration maximum temperature of 3-fold pump structure is higher than the other three (Figure 4.1a). For 6 mm rod the same situation is observed for 6-fold structure also beside 3-fold one (Figure 4.1b). As can be observed from the absorbed pump power density plots in Table A2.1, after 1 % at. Nd concentration for 3- fold structure and after 3% at. Nd for 6-fold structure (Table A2.2), absorbed power is localized close to the surface resulting in thermal spots as given in Table A3.1 and Table A3.2, respectively.

Temperature variations with respect to radial distance are plotted on Figure 4.2 for 9-fold pump structure. In 3 mm rods, central temperatures are higher than for 6 mm rods. In addition, temperature dispersion (considering dopant concentration) is higher for rods pumped with 808 nm sources. As concentration increases, there are constant temperature regions as it is more easily seen for 808 nm pumped rods.

Constant temperature also means that at these regions there is no absorbed pump power and no contribution to simultaneous emission during lasing.

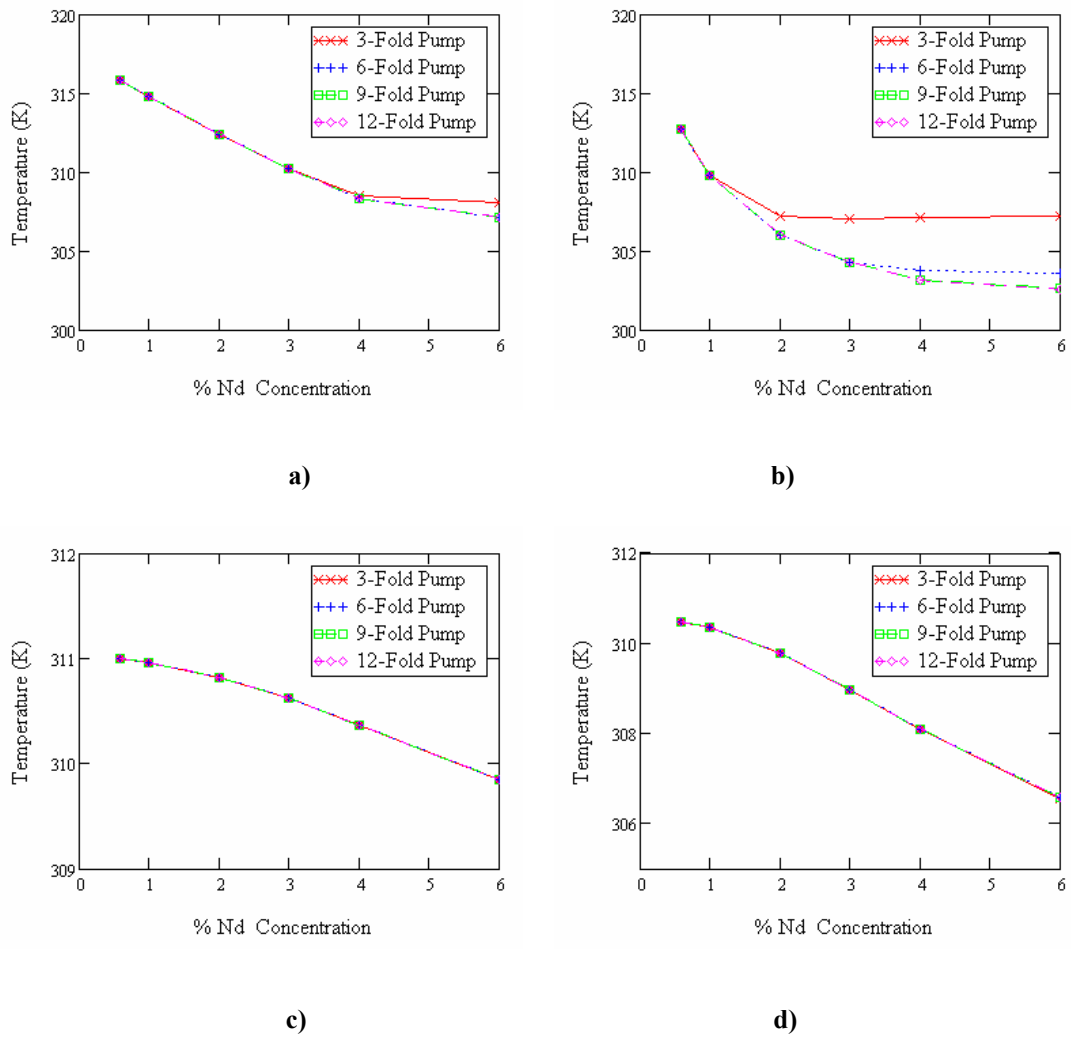
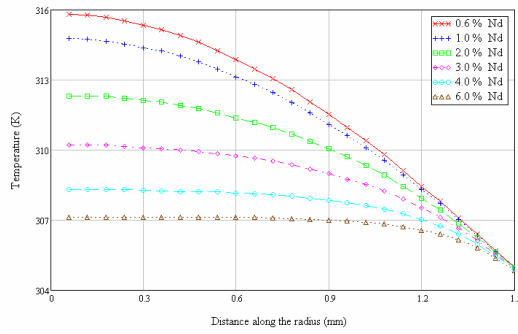
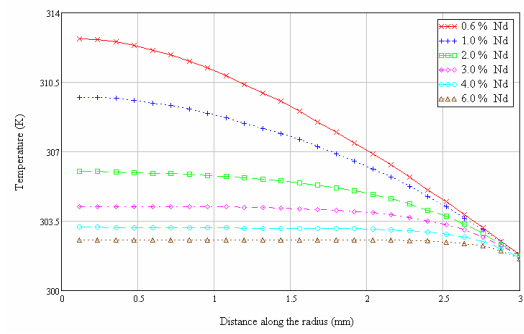


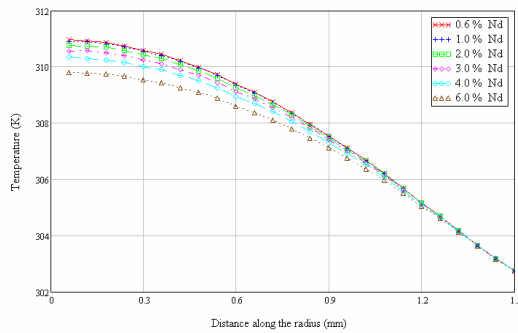
Figure 4. 1 – Maximum temperature in rods a) 3 mm and b) 6 mm using 808 nm pump source and in rods c) 3mm and d) 6 mm using 885 nm pump source as a function of % at. Nd concentrations.



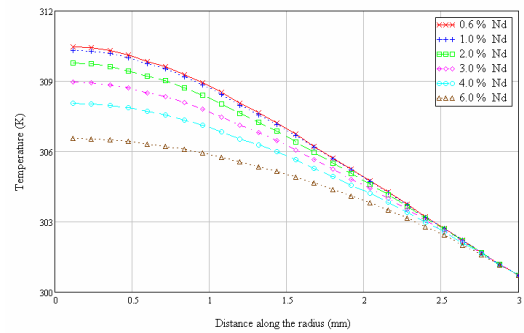
a)



b)



c)



d)

Figure 4. 2 – Temperature distribution as a function of radial distance of 9-fold pump structure a) 3mm and b) 6mm rods with 808 nm pump source and c) 3mm and d) 6mm rods with 885 nm pump source

4.5.2 Thermal Gradient Distribution

Thermal gradient describes the change in temperature within a unit distance. Results of thermal gradient are shown in Tables A4.1-A4.4. Rods with 3 mm diameter and 885 nm pump source have radial dependent thermal gradient (Table A4.3) independent of pump structure. Also rods with 9 and 12-fold pump structures have azimuthal angle free distribution for all diameters and pump sources. 3 and 6-fold structures lose their azimuthal angle free distribution with increase in dopant concentration. Maximum thermal gradients are located close to the rod surface, while minimum gradients are located in the center or at maximum heat regions. High

thermal gradients point out the maximum heat flow regions and low gradients regions where heat flow is low.

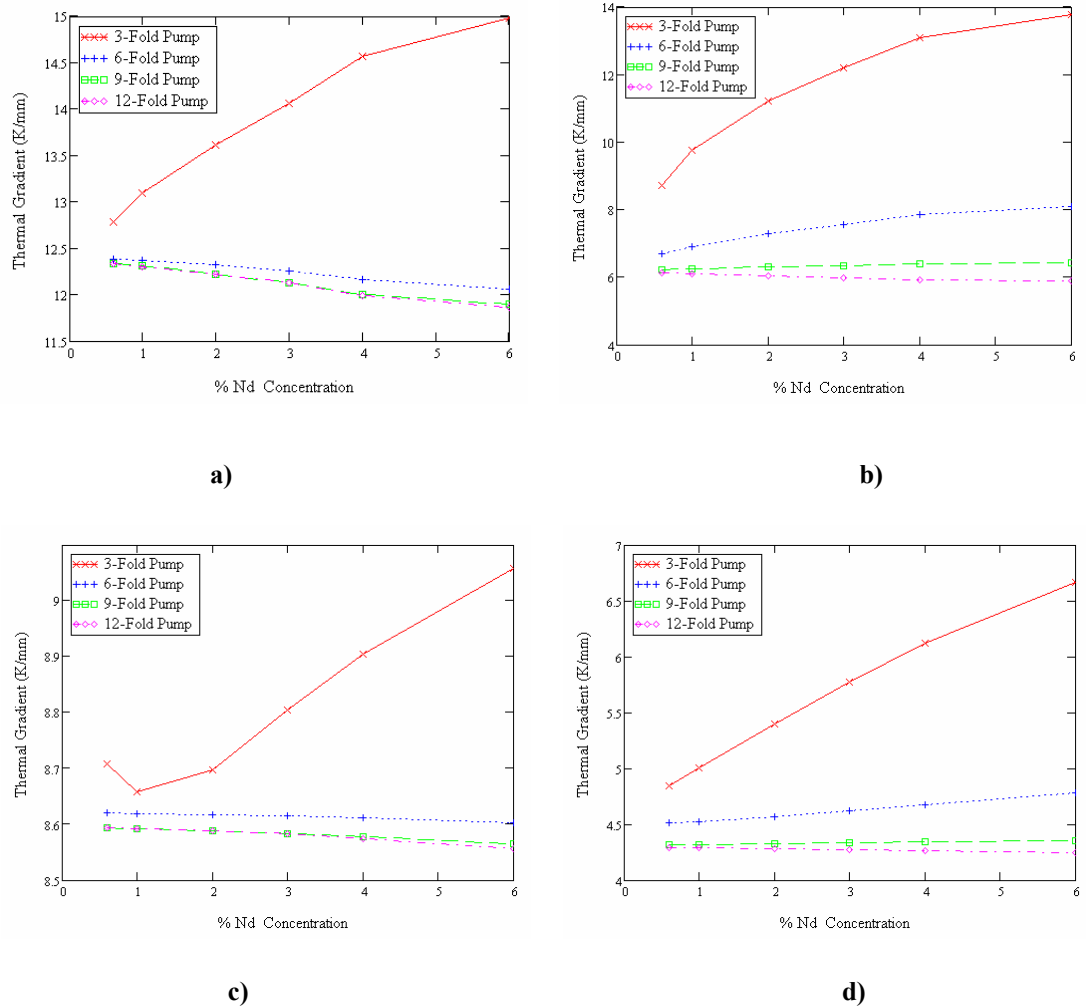


Figure 4.3- Maximum thermal gradient in rods a) 3 mm and b) 6 mm using 808 nm pump source and in rods c) 3mm and d) 6 mm using 885 nm pump source as a function of % at. Nd concentrations.

Figure 4.3 depicts maximum thermal gradient behavior in laser ceramic rods as a function of dopant concentration. From this figure the difference between pump structures is apparent, thermal gradient is inversely proportional to fold number of pump structure. In 3-fold structure, thermal gradient is increasing with the concentration ratio for both pump sources. Thermal gradient in 3 mm rod slightly

decreases with increasing concentration ratio for 6,9 and 12-fold pump structures for both pump sources. However, with the 6 mm rod the situation is not the same, thermal gradient is increasing with increasing concentration for 6-fold pump but slightly decreases for 9 and 12-fold pump structures.

Variation of thermal gradient with radial distance is given in Figure 4.4. Generally getting close to the rod surface thermal gradient is increasing. Type of increase, changes from converging to exponential with increasing dopant concentration.

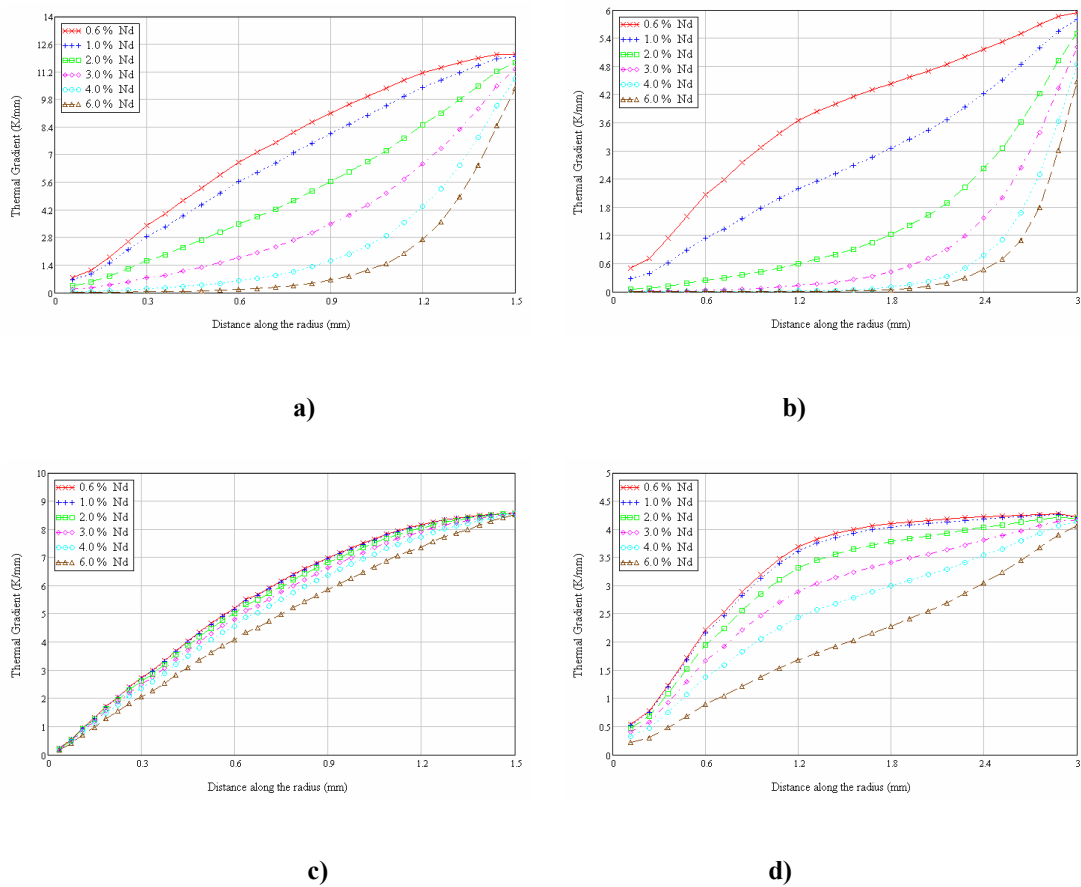


Figure 4. 4 - Thermal gradient distribution as a function of radial distance of 9-fold pump structure a) 3mm and b) 6mm rods with 808 nm pump source and c) 3mm and d) 6mm rods with 885 nm pump source

4.5.3 Radial Stress

Radial stress distributions are given in Tables A5.1-A5.4. Radial stress in 3 mm and 808 nm pumped rod (Table A5.1) is independent from azimuthal coordinate for all structures but 3-fold one. The same is situation for 6 mm and 885 nm pumped rod (Table A5.4). In Table A5.2 (6 mm, 808 nm), radial stress is dependent on azimuthal coordinate for all pump structures except for 12-fold one. For 3 mm and 885 nm pumped rod, radial stress is independent from azimuthal coordinate for all pump structures (Table A5.3).

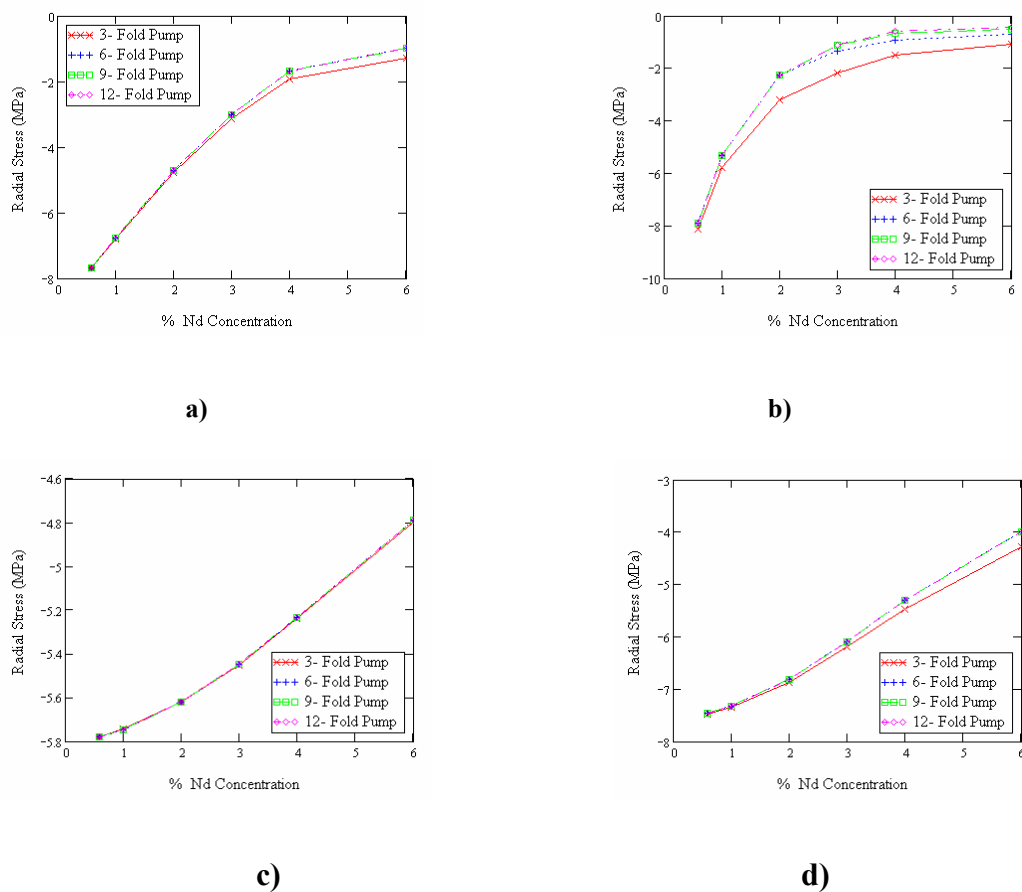
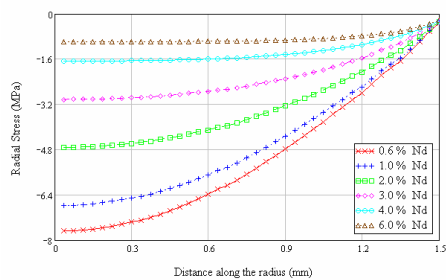


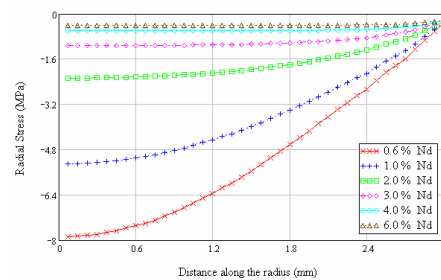
Figure 4.5 - Maximum radial stress in rods a) 3 mm and b) 6 mm using 808 nm pump source and in rods c) 3mm and d) 6 mm using 885 nm pump source as a function of % at. Nd concentrations.

Figure 4.5 depicts the variation of maximum azimuthal stress with dopant concentration. There is a decrease in stress for all rods with increase in dopant concentration. Maximum radial stress in all rods is compressive. Comparing the pump structures maximum stress is developed in 3-fold pump structure.

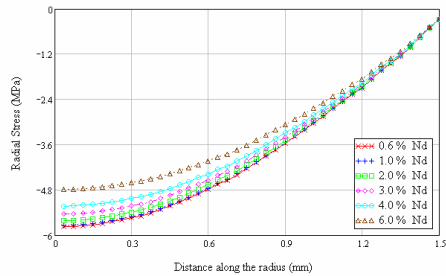
In Figure 4.6 variation of radial stress with radial distance is given. Stress is negative through the rod and decreasing to zero at the rod surface. Maximum is located at the center of the rod.



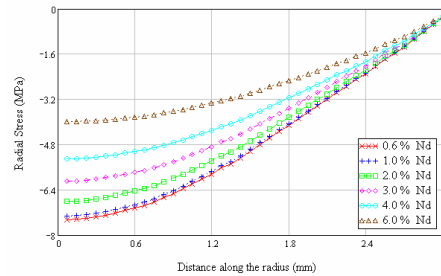
a)



b)



c)



d)

Figure 4. 6 – Radial stress distribution as a function of radial distance of 9-fold pump structure a) 3mm and b) 6mm rods with 808 nm pump source and c) 3mm and d) 6mm rods with 885 nm pump source

4.5.4 Azimuthal Stress

Azimuthal stress distributions are given in Tables A6.1-A6.4. Radial stress does not have an azimuthal dependence except for 3-fold pump structure at high concentrations. Inner parts of rods are under compression and outer parts are in tension for all rods pumped.

Variation of maximum azimuthal stress as a function of dopant concentration is given on Figure 4.7. With increasing dopant concentration there is decrease in maximum azimuthal stress. Stress decreases with slope up for 808 nm pumped rods and with slope down for 885 nm pumped ones. 3-fold pump structure has higher stress compared to others. There is decrease in stress with increase in fold number.

Figure 4.8 depicts the stress variations along the radius of a rod. As observed from the figure central part of rod is under negative stress meaning compression and outer part is under positive stress meaning tension. Almost at the center of the radial distance of each rod, azimuthal stress is zero, point where stress is changing from compression to tension.

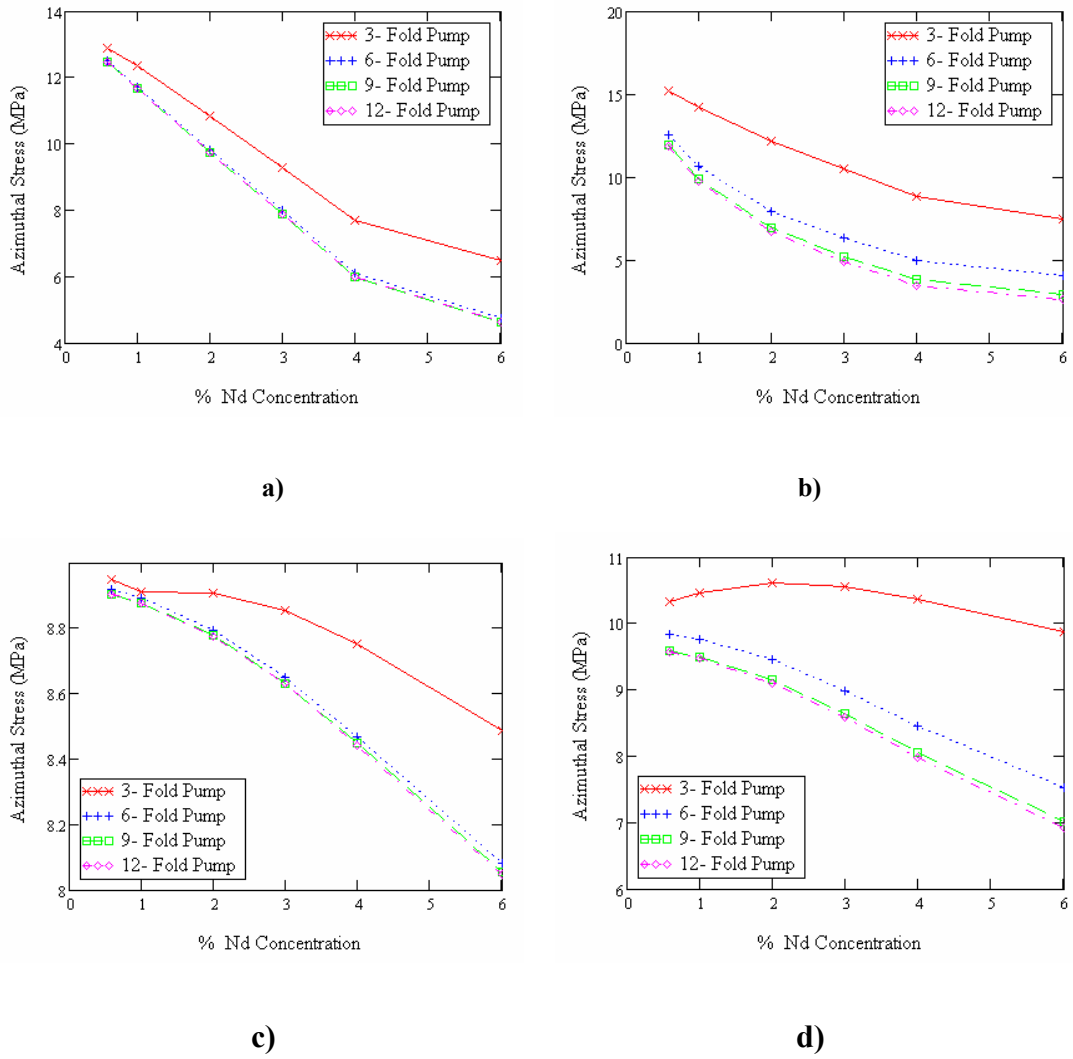
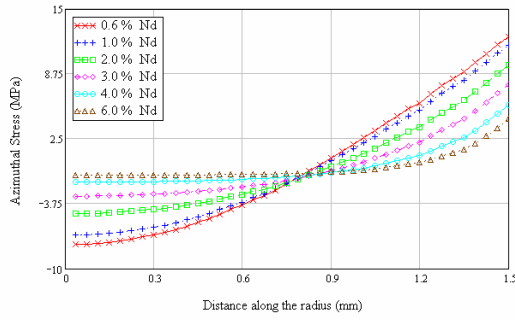
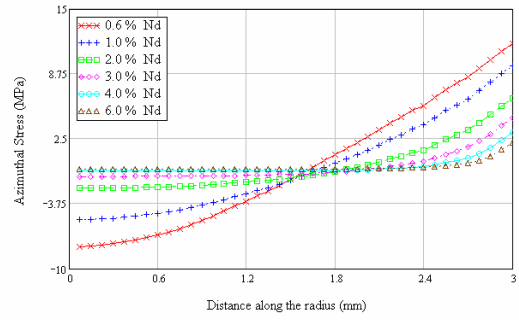


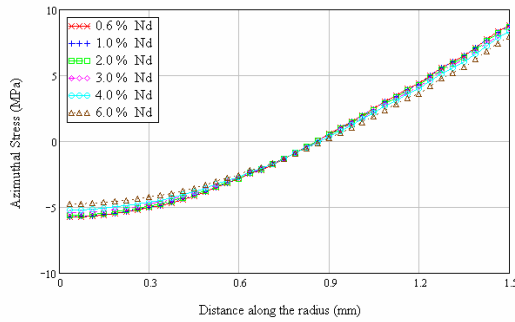
Figure 4. 7 - Maximum azimuthal stress in rods a) 3 mm and b) 6 mm using 808 nm pump source and in rods c) 3mm and d) 6 mm using 885 nm pump source as a function of % at. Nd concentrations.



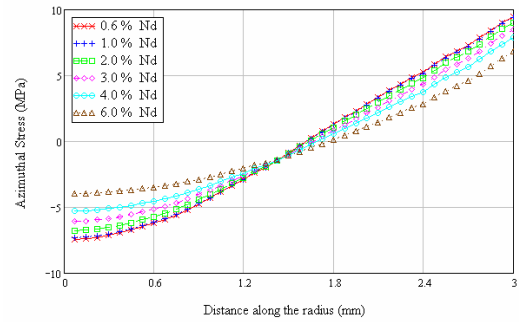
a)



b)



c)



d)

Figure 4. 8 - Azimuthal stress distribution as a function of radial distance of 9-fold pump structure a) 3mm and b) 6mm rods with 808 nm pump source and c) 3mm and d) 6mm rods with 885 nm pump source

4.5.5 Axial Stress

Axial stress distributions are given in Tables A7.1-A7.2. Axial stress in 3 mm and 808 nm pumped rod (Table A7.1) is independent from azimuthal coordinate for all structures but 3-fold one. The same is situation for 6 mm and 885 nm pumped rod (Table A7.4). In Table A7.2 (6 mm, 808 nm), axial stress is dependent on azimuthal coordinate for all pump structures except for 12-fold one. For 3 mm and 885 nm pumped rod, axial stress is independent from azimuthal coordinate for all pump structures (Table A7.3).

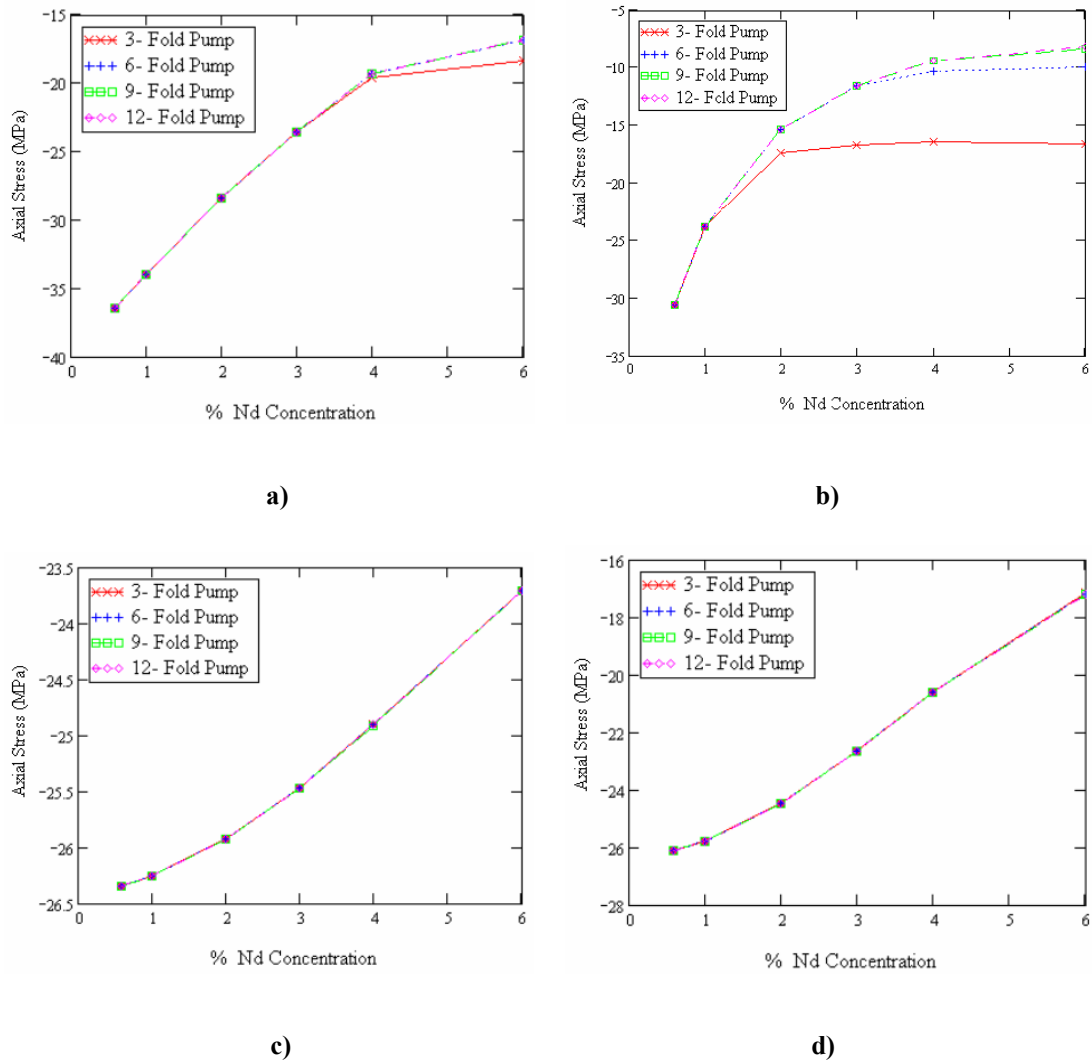
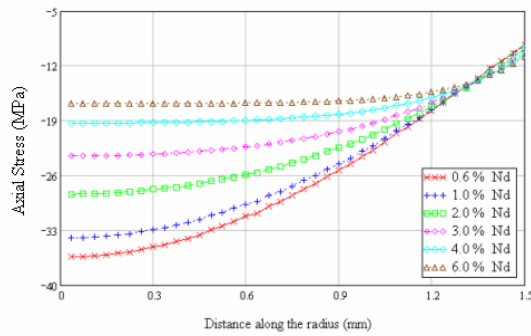


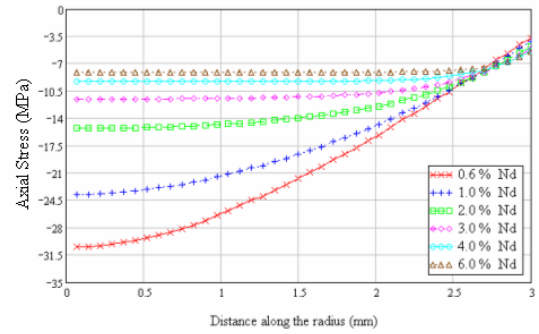
Figure 4.9 - Maximum axial stress in rods a) 3 mm and b) 6 mm using 808 nm pump source and in rods c) 3mm and d) 6 mm using 885 nm pump source as a function of % at. Nd concentrations.

Maximum axial stresses resulted in the rods are plotted as a function of dopant concentration in Figure 4.9. From the figure, it is observed that there is decrease in maximum stress with increasing dopant concentration. There is no effect of pump structure on maximum stress generated in rods pumped with 885 nm sources (Figures 4.9c and 4.9d). But this is not the case for 808 nm pumped ones. For 3 mm rod at 6 % at. Nd concentration maximum stress of 3-fold pump structure is higher than the other three (Figure 4.9a). For 6 mm rod the same situation is observed for 6-fold structure also beside 3-fold one (Figure 4.9b).

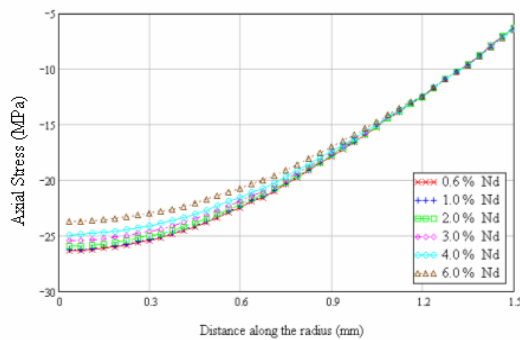
In Figure 4.10 variation of axial stress with radial distance is given. Stress is negative and increasing to zero at the rod surface. Maximum is located at the center of the rod as for azimuthal stress.



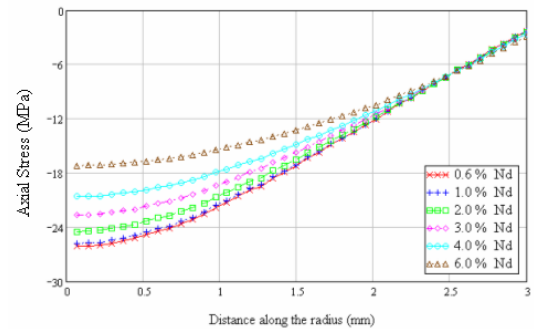
a)



b)



c)



d)

Figure 4. 10 - Axial stress distribution as a function of radial distance of 9-fold pump structure a) 3mm and b) 6mm rods with 808 nm pump source and c) 3mm and d) 6mm rods with 885 nm pump source

4.5.6 Shear Stress

Shear stress distributions across pumped rods are given in Tables A8.1-A8.4.

Maximum shear stresses resulted in the rods are plotted as a function of dopant concentration in Figure 4.11. From the figure, it is observed that there is decrease in maximum stress with increasing dopant concentration. 3-fold pump structure has higher stress compared to others. There is decrease in stress with increase in fold number.

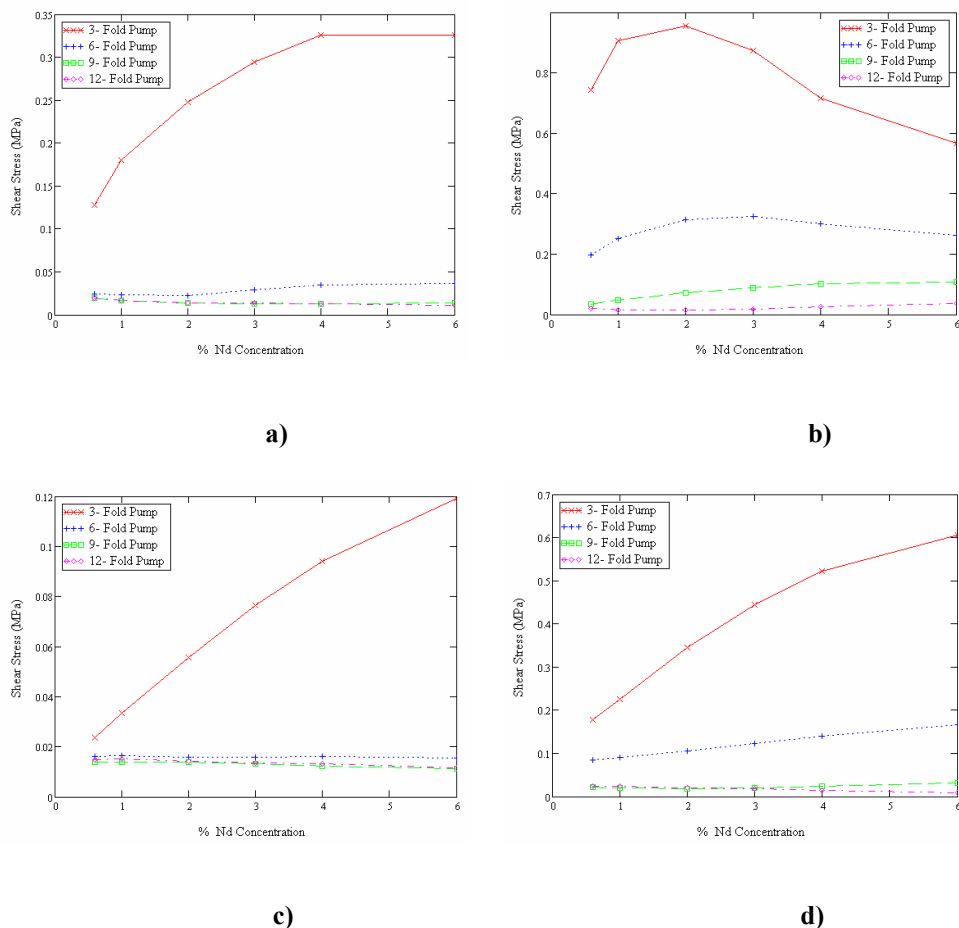


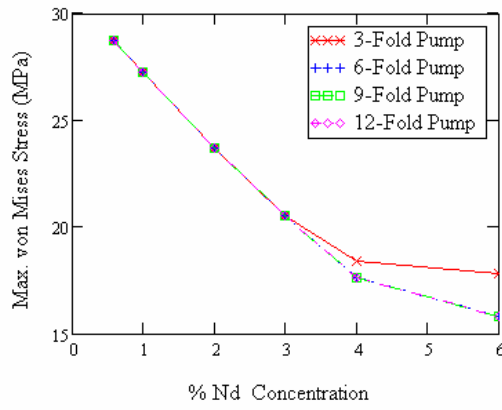
Figure 4. 11 - Maximum shear stress in rods a) 3 mm and b) 6 mm using 808 nm pump source and in rods c) 3mm and d) 6 mm using 885 nm pump source as a function of % at. Nd concentrations.

4.5.7 Von Mises Stress

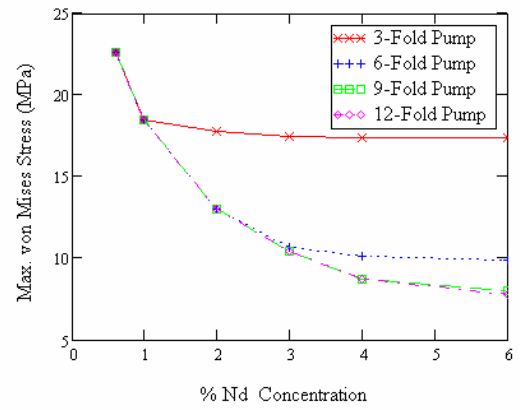
Results of von Mises stress distribution through the rods are given in Tables A9.1 to A9.4. Stress distribution is not dependent on azimuthal coordinate for 885 nm pump source (Table A9.3 and Table A9.4). 808 nm source pumped rods have dependence on azimuthal coordinate with 3 and 6-fold pump structure. This dependence increases with increasing % at. Nd dopant concentration. As observed from these tables with increase in dopant concentration, area of maximum stress (in rod central parts) is increasing.

Maximum stresses resulted in the rods are plotted as a function of dopant concentration in Figure 4.12. From the figure, it is observed that there is decrease in maximum stress with increasing dopant concentration. There is no effect of pump structure on maximum stress generated in rods pumped with 885 nm sources (Figures 4.12c and 4.12d). However, this not the case for 808 nm pumped ones. For 3 mm rod at 6 % at. Nd concentration, maximum stress of 3-fold pump structure is higher than the other three (Figure 4.12a). For 6 mm rod the same situation is observed for 6-fold structure also beside 3-fold one (Figure 4.12b).

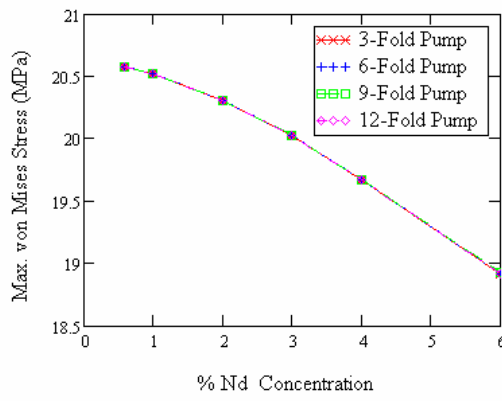
Stress variations with respect to radial distance are plotted on Figure 4.13 for 9-fold pump structure. In 3 mm rods, central stresses are higher than for 6 mm rods. Stress in 885 nm source pumped rods is less than 808 nm pumped ones.



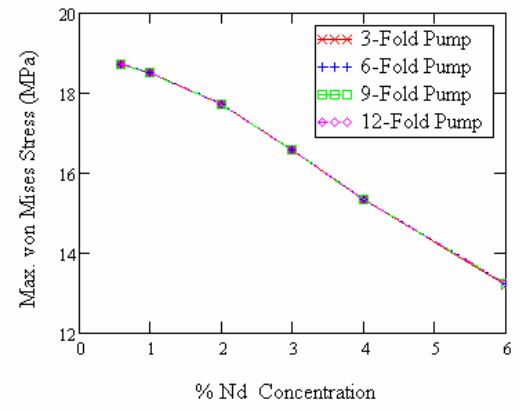
a)



b)

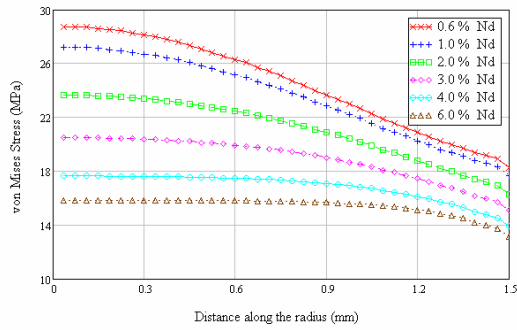


c)

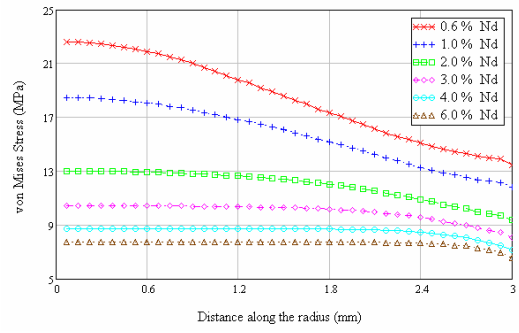


d)

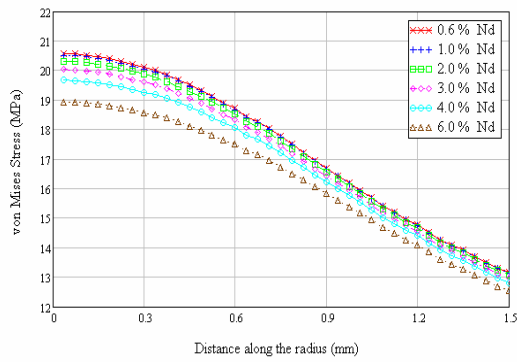
Figure 4. 12 - Maximum von Mises stress in rods a) 3 mm and b) 6 mm using 808 nm pump source and in rods c) 3mm and d) 6 mm using 885 nm pump source as a function of % at. Nd concentrations.



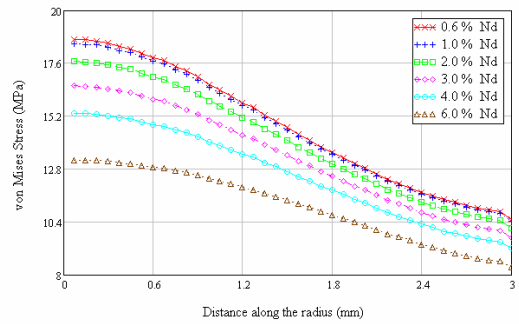
a)



b)



c)



d)

Figure 4. 13 – von Mises stress distribution as a function of radial distance of 9-fold pump structure a) 3mm and b) 6mm rods with 808 nm pump source and c) 3mm and d) 6mm rods with 885 nm pump source

CHAPTER 5

OPTICAL ANALYSIS

5.1 Introduction

Stress and temperature developed in materials have influence on the optical properties of that material. Stress causes index variations that result in change in refractive index differently in each principal direction, known as birefringence effect. Temperature also causes refractive index changes, which do not result in birefringence, since temperature is independent of direction. Birefringence causes a depolarization of a polarized light, which results in loss for linearly polarization operating lasers.

Temperature and stress are different at each point through out the pumped laser material resulting in refractive index variations. Since index of refraction is different at each point laser material behaves like a GRIN lens, trying to focus light passing through it. Also focused light is highly aberrated, which is the effect of different focal distances of each point in the material.

Results of Chapter 4 will be used in calculation of optical properties of materials through the following sections of this chapter.

5.2 Temperature Index Variations

Refractive index of material is dependent on temperature through thermal coefficient of refraction. This coefficient is also temperature dependent, and its variation as a function of temperature is given by Eq. 5.1, [44]. This equation is derived by curve fitting to data reported by many researchers in temperature range 50-450 °K.

$$\frac{\partial n}{\partial T}(T) = -3.5 \cdot 10^{-6} \cdot (T - T_{ref}) + 5.48 \cdot 10^{-8} \cdot (T - T_{ref}) \cdot T - 0.5 \cdot 10^{-10} \cdot (T - T_{ref}) T^2 \quad (5.1)$$

In Eq. 5.1, n is refractive index, T is temperature at which thermal coefficient of refraction will be calculated and T_{ref} is reference temperature. Figure 5.1 gives the plot of Eq. 5.1. Thermal coefficient of refraction is increasing with increase in temperature. Therefore, refractive index is dependent on temperature distribution and on thermal coefficient of refraction as given in Eq.5.2, where n_o is the refractive index of material at T_{ref} .

$$n(T) = n_o + T \cdot \frac{\partial n}{\partial T}(T) \quad (5.2)$$

Using the temperature distribution results of FEA performed previously refractive index distributions are given in Tables A10.1-A10.4.

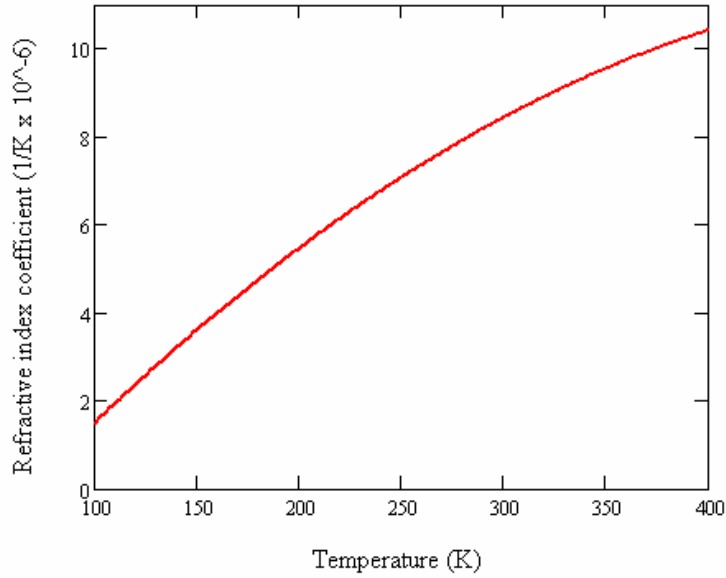


Figure 5. 1 – Dependence of thermal refractive coefficient on temperature

5.3 Birefringence

Stress also has influence on refractive index but, unlike temperature, it is a vectorial quantity. So different directions will have different refractive indices. Impermeability matrix of a material defines its refractive index (Assuming magnetic permeability to be 1). There are two ways of calculating the stress-induced index change. One is to use stress data and Eq. 2.13, the other is to use strain data and Eq. 5.3. The first way requires piezo-optic matrix, which is a function of elasticity modulus and Poisson’s ratio, both temperature dependent quantities. The second method is actually the same with first one but uses directly the results of FEA.

$$B_{ij} = B_{0,ij} + \sum_{i,j,k,l=1}^3 p_{ijkl} \epsilon_{kl} \quad (5.3)$$

In Eq. (5.3), \mathbf{B} is indicatrix matrix, \mathbf{p} is material stress optic coefficients in $\langle 111 \rangle$ Nd:YAG single crystal direction [40] and ε is strain obtained by stress analysis.

Results of Eq. 5.3 will reveal the difference in refractive indices in radial and azimuthal direction, which results in birefringence.

5.4 Depolarization

Birefringence has effect on polarization of light passing through the material. In ceramics, single crystals are oriented randomly so it is difficult to calculate depolarization effect. Shoji and Taira [45] analytically show that it is possible to decrease depolarization by using $\langle 110 \rangle$ cut single crystals. In addition, maximum depolarization was found for $\langle 111 \rangle$ grown single crystal Nd:YAG [45]. Shoji et.al. [46] experimentally show that total depolarization induced in ceramic materials is similar to single crystals in value. Khazanov [47] was the first to point out theoretically the effect of beam spatial modulation (both amplitude and phase) in ceramics, which is dependent on average grain size to material length ratio. This prediction is verified experimentally by Mukhin et.al. [48].

In calculations of depolarization, total depolarization is the primary concern and it is assumed ceramics to behave like $\langle 111 \rangle$ oriented single crystals. Eqs 2.19, 2.20 and 2.21 are used to determine state of depolarization.

5.5 Focal Length

Temperature and stress developed in laser material results in index variations, which cause focusing of a beam passing through it. Focusing is a result of optical path difference of individual rays passing through the material. Optical path difference (OPD) is a function of index change and length of path traveled. Although there are many analytical expressions for calculation of focal length of a laser rod [5],[41],[49] , they are not suitable if azimuthal variation of OPD is present. Numerical calculation of focal length is usually done by first assuming a lens profile (i.e. spherical) and then fitting a spherical curve to OPD data [50], [51], [52]. Equation is given as

$$OPD(r) = OPD_o - \frac{r^2}{R} \quad (5.4)$$

where OPD_o is optical path difference at the center of the rod and R is the curvature of a spherical mirror. A.E. Siegman [53] defines the index variation across a laser rod as

$$n(r) = n_o - \frac{1}{2} \frac{r^2}{f \cdot L_{rod}} \quad (5.5)$$

where L_{rod} is rod length and f is laser rod focal length. Again by [41] and [53], inverse of focal length is defined as second order differential of OPD given as

$$\frac{1}{f} = \frac{\partial^2 OPD(r, \phi)}{\partial r^2} \quad (5.6)$$

Also Chen et al. [54], defines focal length as

$$\frac{1}{f} = -\frac{-2(OPD(r, \phi) - OPD(r_o, \phi))}{(r - r_o)^2} \quad (5.7)$$

The four equations given above are actually the same. Eq. (5.4) and (5.5) are the same if (5.5) is multiplied by rod length. In addition, Eq. (5.7) is equal to (5.4) if r_o is assumed to be at $r=0$. The three equations 5.4, 5.5 and 5.7 are definitions of second differential of OPD, that is, they are equal to Eq. (5.6).

5.6 Results

5.6.1 Temperature Index Variations

Temperature variations of refractive index are calculated using Eq. (5.2). Tables A10.1 and A10.2 give the results of 3 mm and 6 mm rods respectively for 808 nm pump source. Moreover, Tables A10.3 and A10.4 give the results of 3 mm and 6 mm rods respectively for 885 nm pump source. Maximum index is at the center of the rod for all pump structures for 885 nm pumped rods and 9 and 12-fold pump structures for 808 nm source. Index variations have radial dependence except for 3 and 6- fold pump structures of 808 nm pumped rods.

Figure 5.2 depicts index variations averaged to radial distance. Highest index develops at center of the rod. Lower % Nd concentrations have higher refractive index. Index is the same for all concentrations at the surface of the rod. Rods pumped with 808 nm sources have higher indexes compared to 885 nm

pumped ones. In addition, 3 mm diameter rods have higher indexes compared to 6 mm rods.

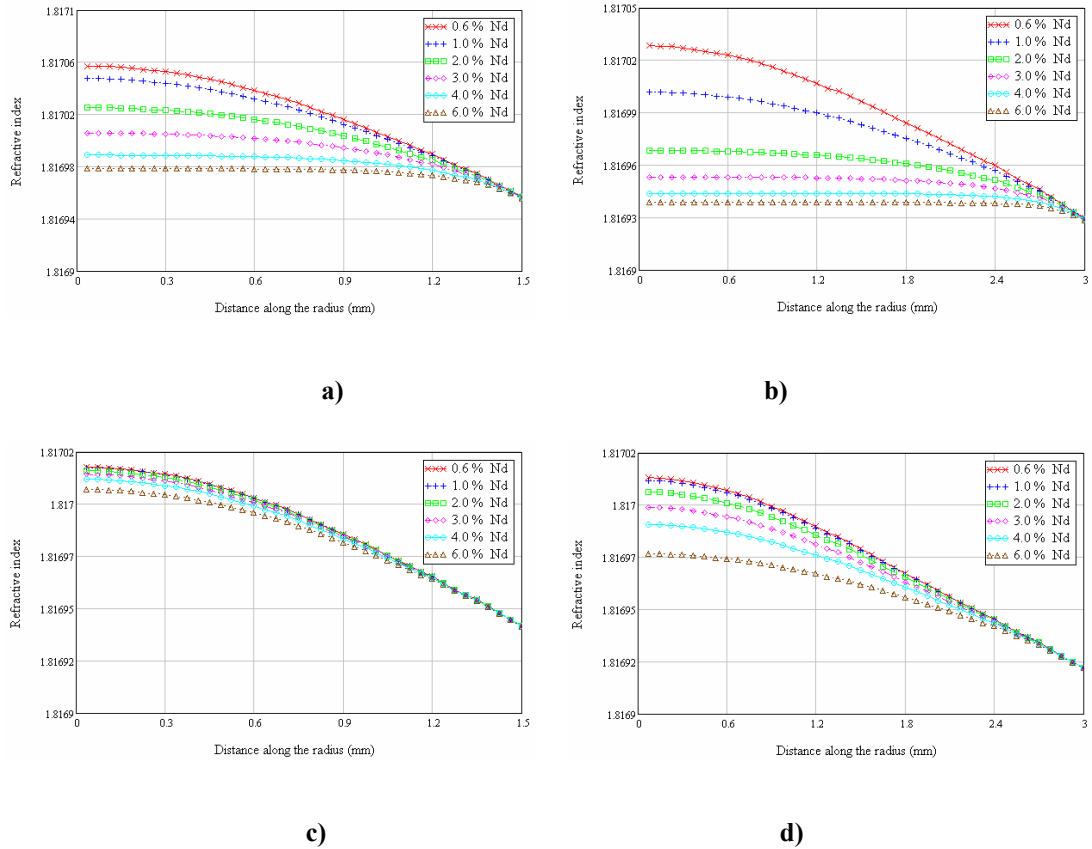


Figure 5.2– Thermal index variation as a function of radial distance of 9-fold pump structure a) 3mm and b) 6mm rods with 808 nm pump source and c) 3mm and d) 6mm rods with 885 nm pump source

5.6.2 Birefringence

In Tables A11.1-A11.4 and Tables A12.1-A12.4 refractive index distributions across the rods for radially and azimuthally polarized light is given, respectively.

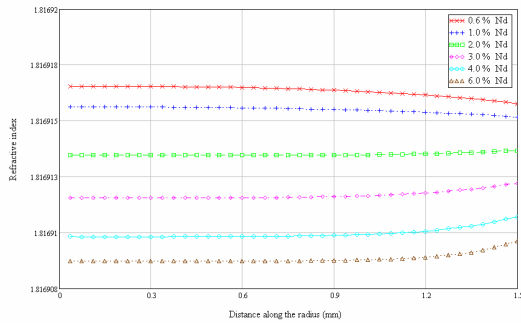
Higher refractive indexes occur at the center of the rod for 3 mm and 885

nm source pumped materials of azimuthally polarized light. Other rods and pump sources have radial and azimuthal coordinate dependent index variations except for: 3 mm 808 nm pumped rods with 0.6 and 1.0 % Nd concentration using 9 and 12 fold pump structure, 6 mm 808 nm pumped rods with 0.6 % Nd concentration using 9 and 12 fold pump structure, 6 mm 885 nm pumped rods with 0.6, 1.0, 2.0, 3.0, 4.0 % Nd concentration using 9 and 12 fold pump structure.

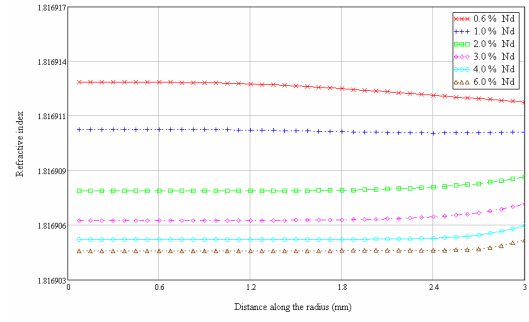
Radially polarized light index distribution is free of azimuthal angle dependence for 885 nm source pumped rods. Maximum refractive index is located at the center of the rods. For 808 nm pumped 3 mm rods with 6, 9 and 12-fold pump structure and 6 mm rods with 9 and 12-fold pump structure also have azimuthal angle free index distribution. While the rest of 808 nm pumped rods possess, both azimuthal and radial coordinate dependent refractive index distributions.

Figure 5.3 depicts the variation of refractive index for azimuthally polarized light along the rod radius. For 808 nm pumped rods, having low Nd concentration maximum index is at the rod center and decreasing at the rod surface. Nevertheless, as Nd concentration increases maximum is located at the rod surface while there is constant index in the rod inner parts. However, for 885 nm pumped rods maximum occurs at the rod center and decreasing at the rod surface for both rod diameters.

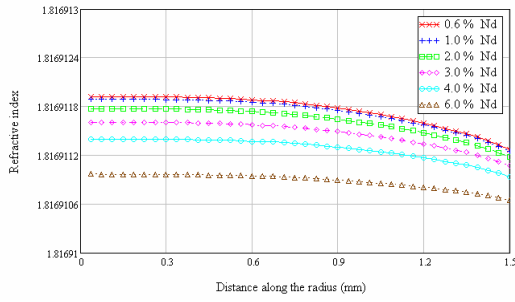
Variations of refractive index for radially polarized light are given in Figure 5.4. For all rods and pump sources maximum occurs at the rod center and minimum at the rod surface. Considering Nd concentration, maximum refractive index at the rod center is for low Nd concentrated rods while at the rod surface maximum is for high Nd concentrated rods.



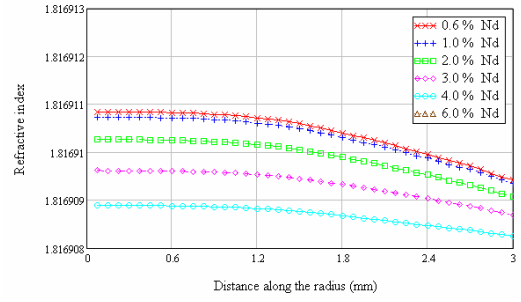
a)



b)

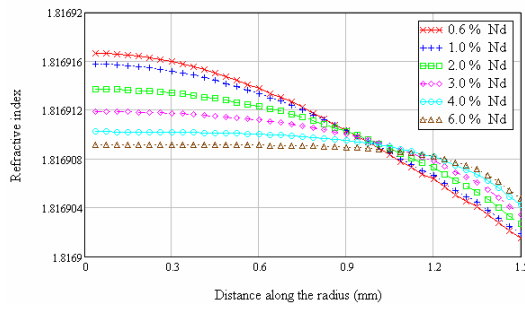


c)

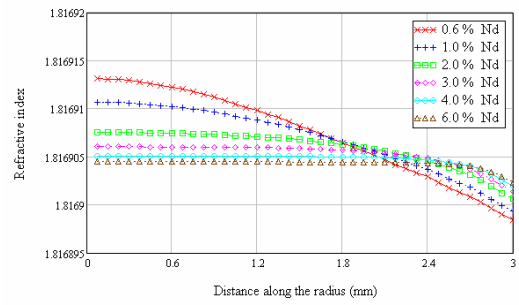


d)

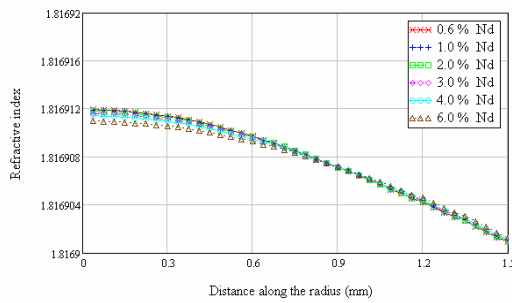
Figure 5.3 – Azimuthally polarized light index variation as a function of radial distance of 9-fold pump structure a) 3mm and b) 6mm rods with 808 nm pump source and c) 3mm and d) 6mm rods with 885 nm pump source



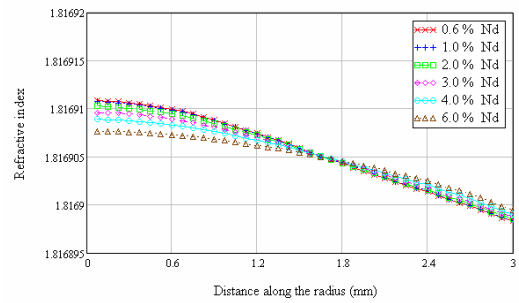
a)



b)



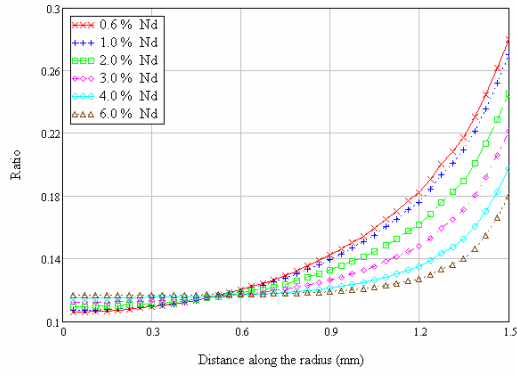
c)



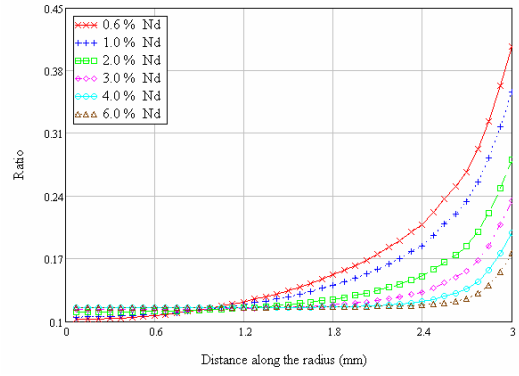
d)

Figure 5. 4 – Radially polarized light index variation as a function of radial distance of 9-fold pump structure a) 3mm and b) 6mm rods with 808 nm pump source and c) 3mm and d) 6mm rods with 885 nm pump source

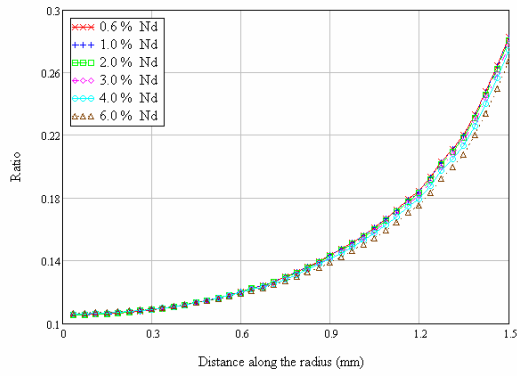
Compared to temperature induced refractive index change, stress induced ones are less. Figure 5.5 gives the ratio between OPD resulted stress induced refractive index change for azimuthally polarized light to temperature induced one. At rod center ratio is low and it is high at the surface. The ratio of stress induced refractive index change for radially polarized light to temperature induced one is given in Figure 5.6. At the rod center maximum occurs and minima are located at rod surface.



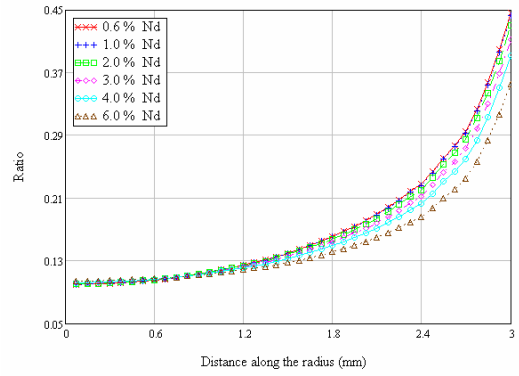
a)



b)

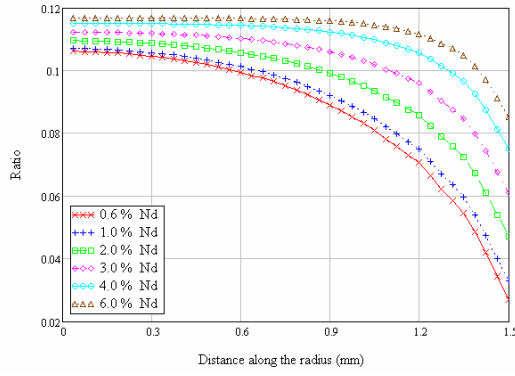


c)

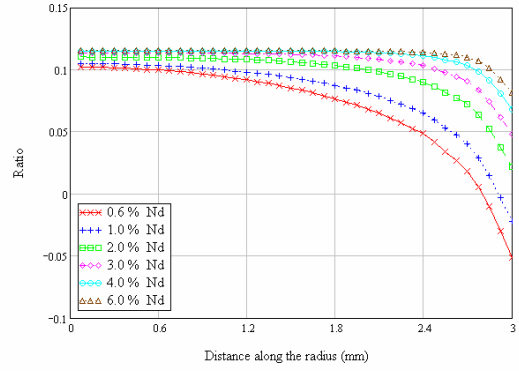


d)

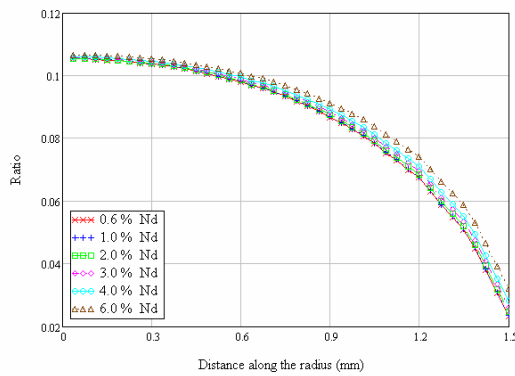
Figure 5.5- Ratio of stress induced index variations of azimuthally polarized light to temperature induced index variations as a function of radial distance of 9-fold pump structure a) 3mm and b) 6mm rods with 808 nm pump source and c) 3mm and d) 6mm rods with 885 nm pump source



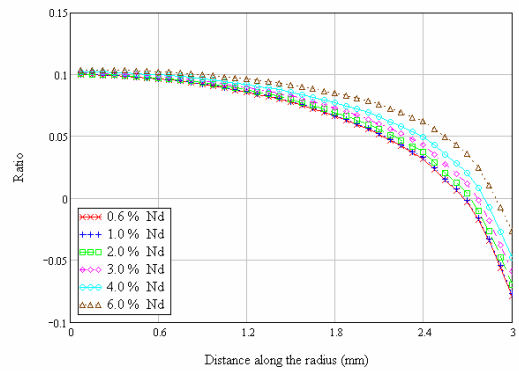
a)



b)



c)



d)

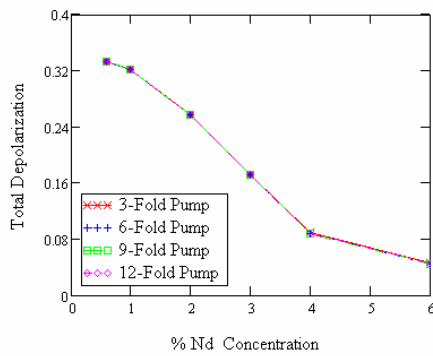
Figure 5.6 - Ratio of stress induced index variations of radially polarized light to temperature induced index variations as a function of radial distance of 9-fold pump structure a) 3mm and b) 6mm rods with 808 nm pump source and c) 3mm and d) 6mm rods with 885 nm pump source

5.6.3 Depolarization

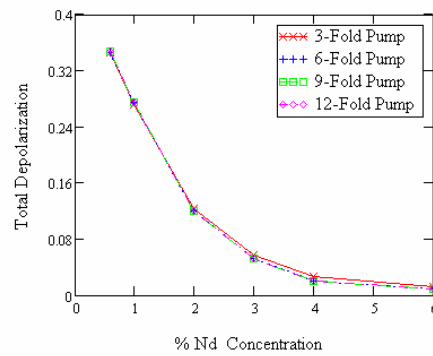
Depolarization distribution is given in Tables A13.1-A13.4. Regions of depolarization are located at four regions separated by 90° azimuthally. Unpolarized regions are in the form of cross and located between the depolarization regions. Depolarization regions move the surface for all rods as Nd concentration is increasing. Comparing rods with same Nd concentration, highly depolarized regions of 808 nm source are close to the surface than the 885 nm pumped ones. In 3-fold

pumped rods as the Nd concentration increases there are still four depolarization regions but in two of the depolarization is higher the other two.

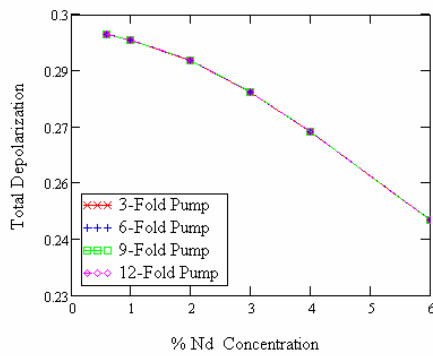
Total depolarization of light passing through the rods is given in Figure 5.7. Total depolarization is decreasing with increase in Nd concentration. There is no difference between total depolarization values of light passing through the rods with different pump structures. Rods pumped with 885 nm sources have higher depolarization values compared to 808 nm pumped ones.



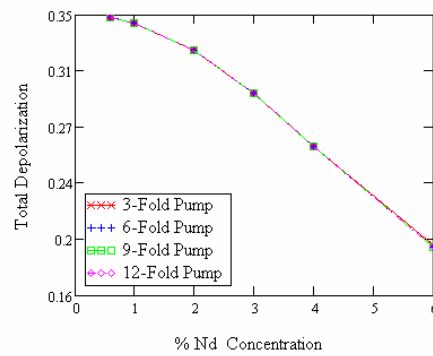
a)



b)



c)



d)

Figure 5. 7 - Depolarization as a function of % Nd³⁺ at. concentration a) 3mm and b) 6mm rods with 808 nm pump source and c) 3mm and d) 6mm rods with 885 nm pump source

5.6.4 Focal Length

Focal length results are given in Figures 5.8 and 5.9 for azimuthally and radially polarized lights, respectively. For both polarizations, focal length is increasing with increasing Nd concentration. Rods with 3 mm diameter have short focal lengths compared to 6 mm ones. In addition, rods pumped with 808 nm sources have longer focal lengths compared to 885 nm source pumped ones.

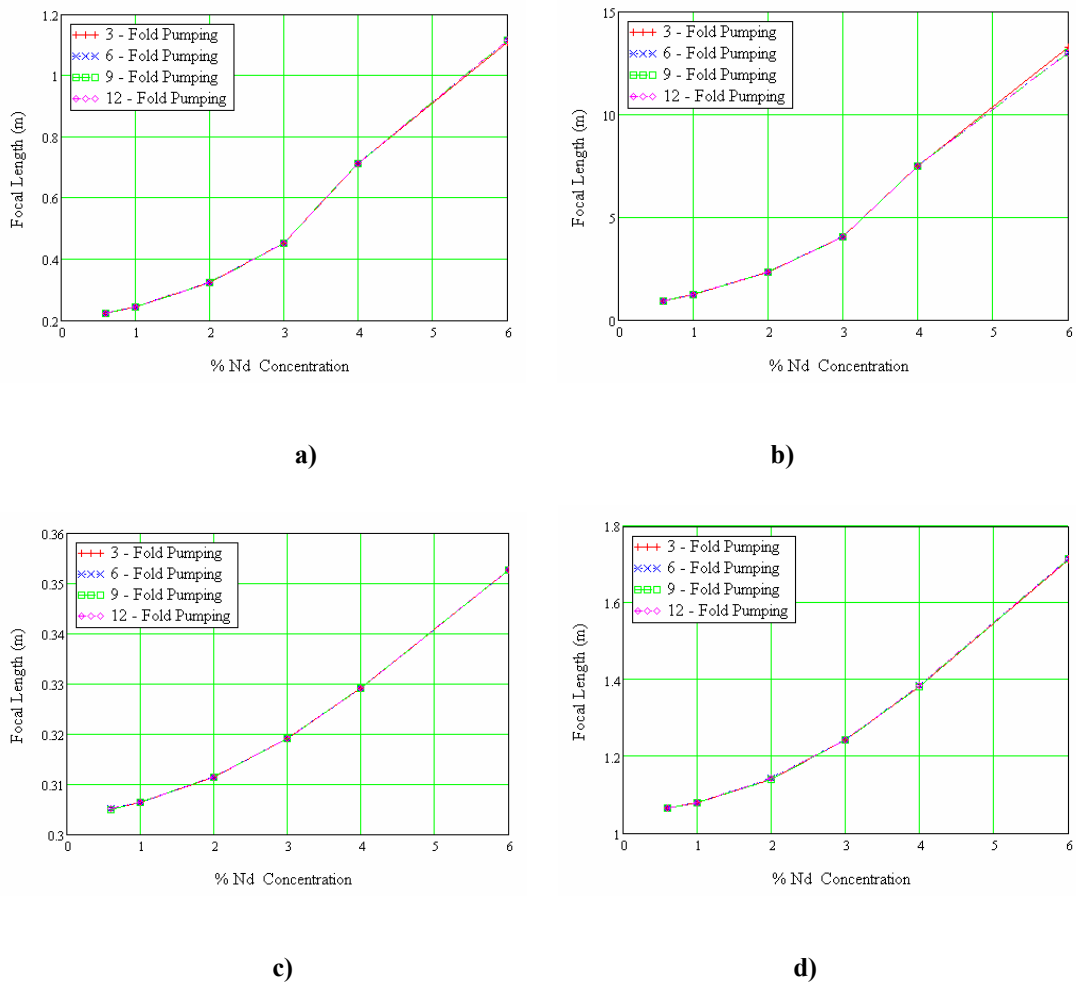
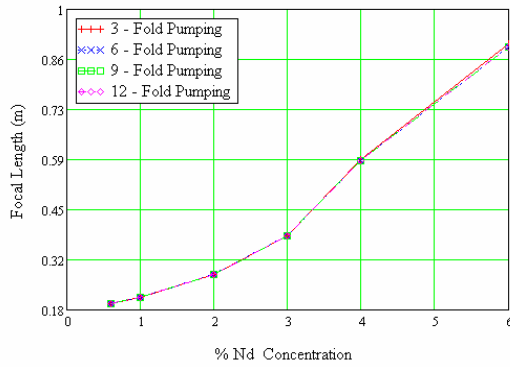
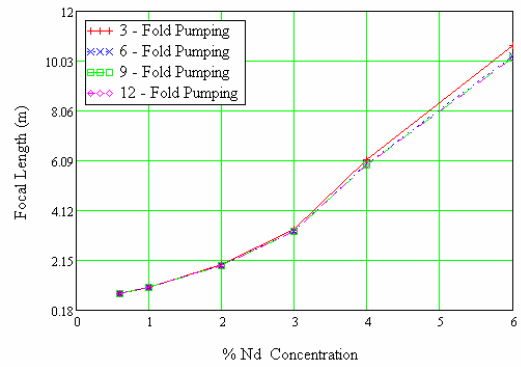


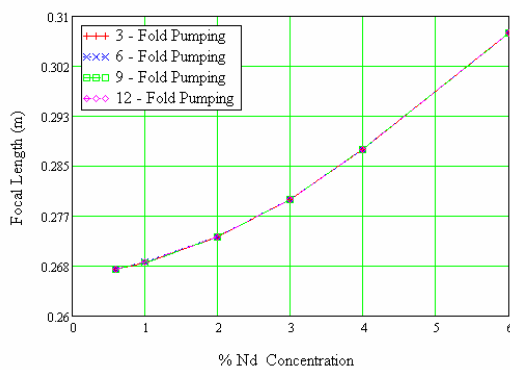
Figure 5. 8- Azimuthally polarized light focal length as a function of % Nd³⁺ at. concentration a) 3mm and b) 6mm rods with 808 nm pump source and c) 3mm and d) 6mm rods with 885 nm pump source



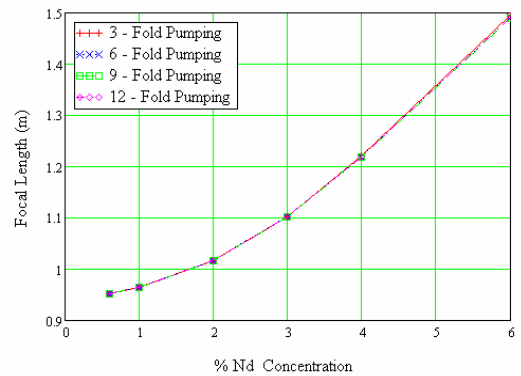
a)



b)



c)



d)

Figure 5. 9- Radially polarized light focal length as a function of % Nd³⁺ at. concentration a) 3mm and b) 6mm rods with 808 nm pump source and c) 3mm and d) 6mm rods with 885 nm pump source

Percentage difference between focal lengths of radially and azimuthally polarized lights is given in Figure 5.10. Ratio is increasing with increasing Nd concentration. In addition, ratio is higher for 808 nm source pumped compared to 885 nm source pumped ones, which means that polarization astigmatism is higher for 808 nm source pumped rods.

It is known that contribution of temperature to focal length is larger compared to stress induced focal lengths. The influence of stress is generally to reduce the focal length of laser rod. Figures 5.11 and 5.12 show the percentage influence of stress induced OPD on focal length. In the figures, negative percentage

indicates the reducing while positive one indicates increasing effect of stress on focal length.

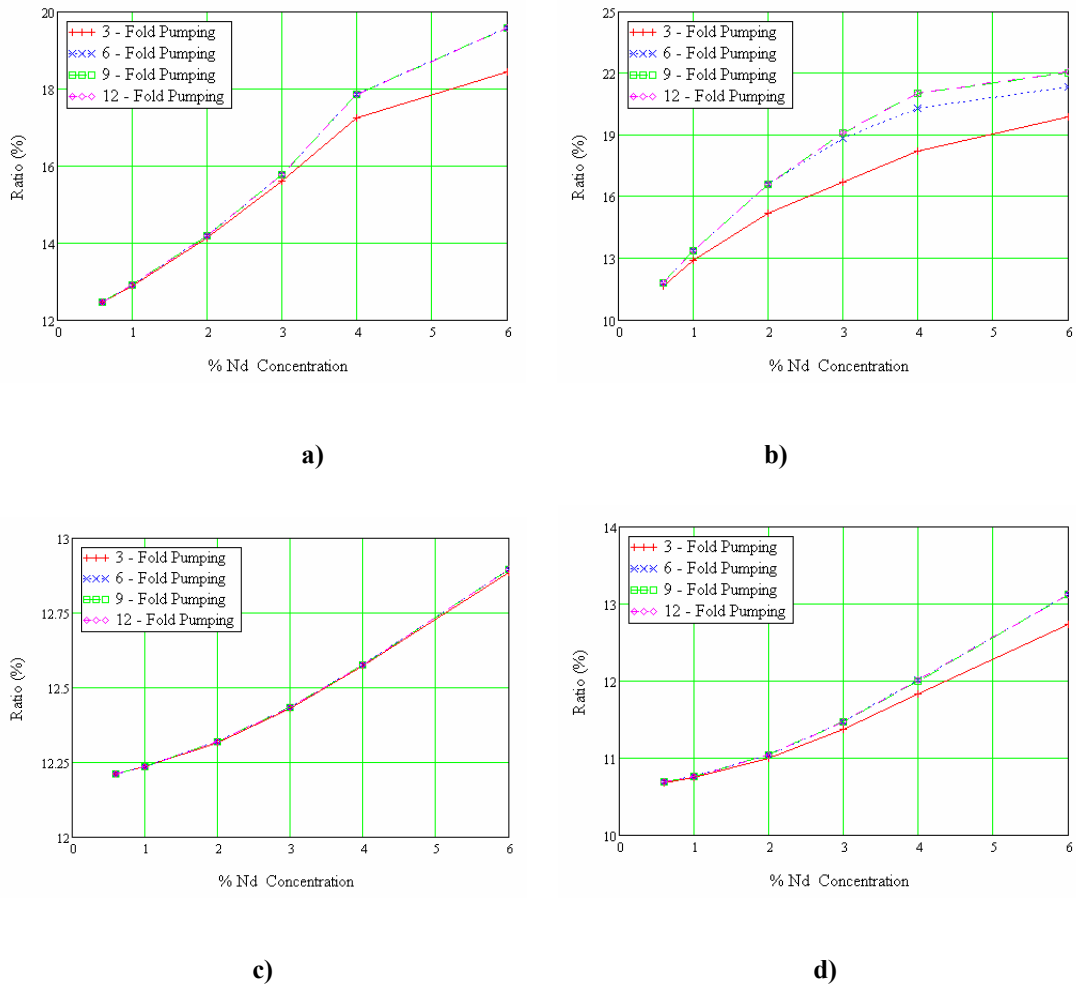


Figure 5.10- Ratio of the difference of radially polarized light focal length and azimuthally polarized light focal length to the azimuthally polarized light one as a function of % Nd³⁺ at concentration a) 3mm and b) 6mm rods with 808 nm pump source and c) 3mm and d) 6mm rods with 855 nm pump source

Contribution of stress to the azimuthally polarized light focal length is positive for rods with Nd³⁺ concentration above 1 % at. and pumped with 808 nm sources. In all other cases studied stress induced OPD reduces the focal length of a laser rod. Reducing effect of stress is larger for radially polarized light (Figure 5.12), in contrast to OPD ratios given in Figures 5.5 and 5.6 where stress induced OPD to

temperature induced OPD is higher for azimuthally polarized light. Generally it can be assumed that higher OPD will have larger effects on focal length. However, the location of higher OPD is more important in such cases. Stress induced OPD for azimuthally polarized light (Figure 5.5) is less in the rod center while increases towards the rod surface. This condition results in an approximately equal contribution at each point on the rod to the temperature induced OPD. This contribution does not change the temperature induced OPD distribution but only increases the value of it (Figure 5.13a). While the stress induced OPD for radially polarized light is higher at the rod center and is decreasing towards the rod surface. This contribution increases total OPD at the rod center and does not affect the OPD induced by temperature in regions close to rod surface, which results in different OPD distribution (Figure 5.13b).

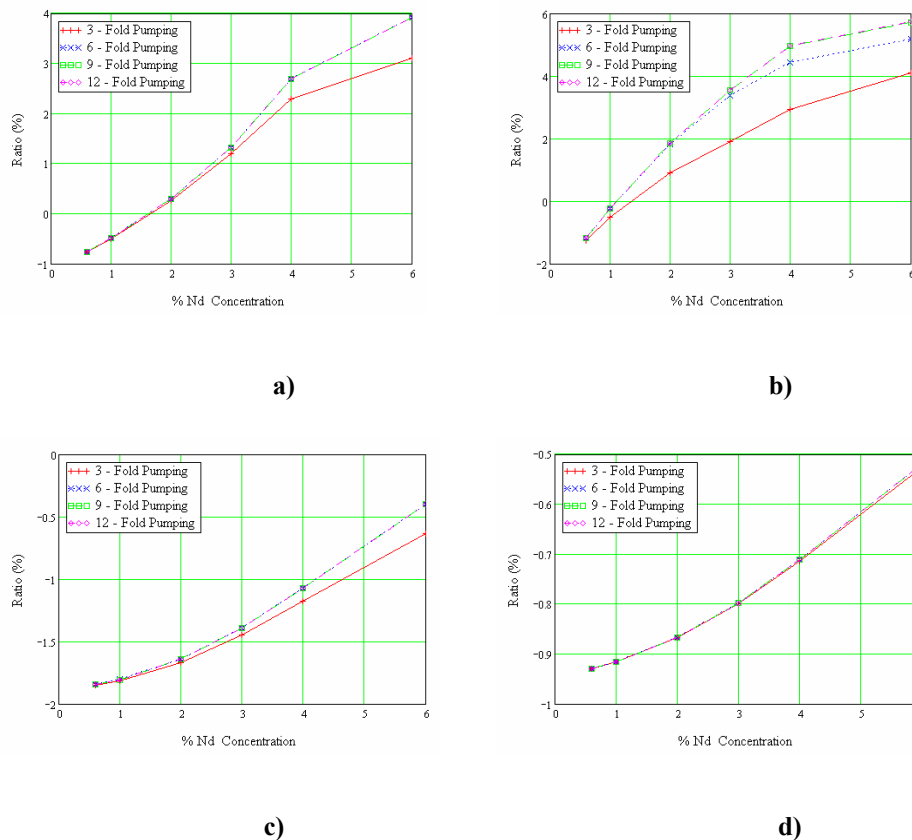
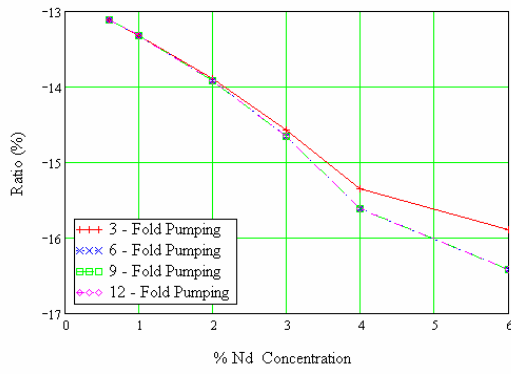
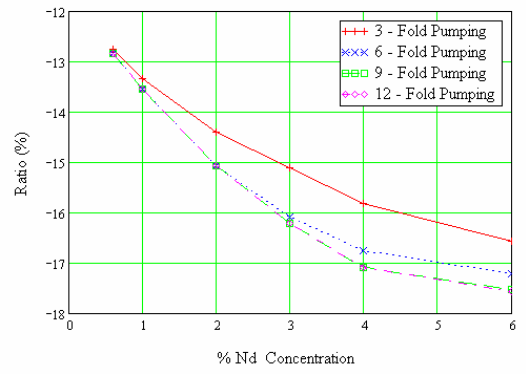


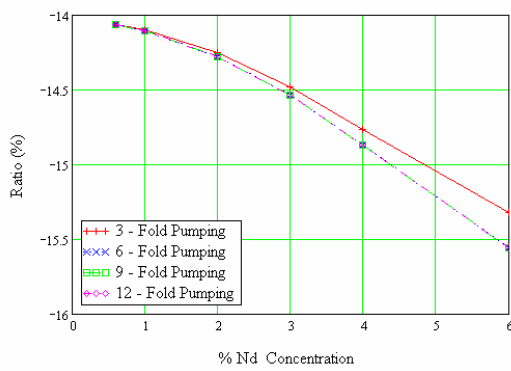
Figure 5. 11 – Percentage contribution of stress induced OPD to the focal length calculated from temperature induced OPD of azimuthally polarized light as a function of % Nd³⁺ at. concentration a) 3mm and b) 6mm rods with 808 nm pump source and c) 3mm and d) 6mm rods with 885 nm pump source



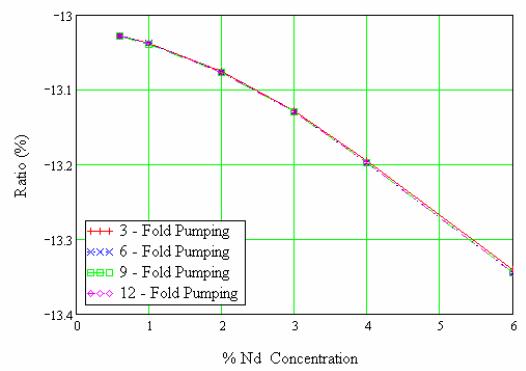
a)



b)

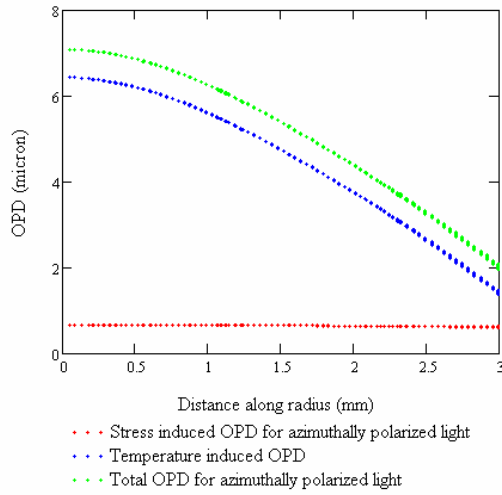


c)

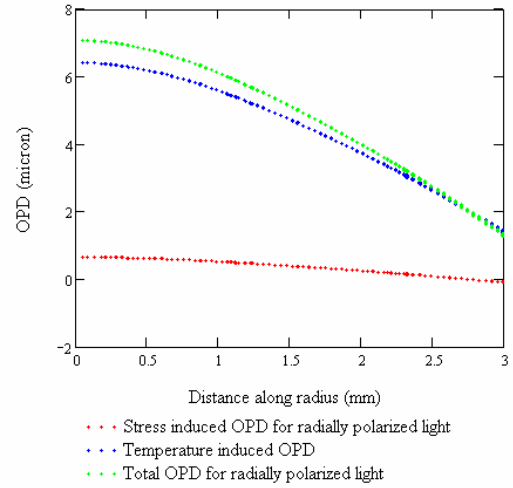


d)

Figure 5.12 - Percentage contribution of stress induced OPD to the focal length calculated from temperature induced OPD of radially polarized light as a function of % Nd³⁺ at. concentration a) 3mm and b) 6mm rods with 808 nm pump source and c) 3mm and d) 6mm rods with 885 nm pump source



a)



b)

Figure 5. 13 Related OPD distributions of 6 mm rod in 9-fold pump structure pumped with 808 nm source, a) azimuthally polarized light, b) radially polarized light.

CHAPTER 6

DISCUSSION

6.1 Introduction

In the preceding chapters, results obtained from the analysis are individually presented. In this chapter effect of dopant concentration, pump structure and pump wavelength on the optical behavior of laser medium will be discussed considering the calculated absorbed power, temperature and stress distribution. In addition, computed results will be compared with the available knowledge on the subject in the literature.

6.2 Effect of Dopant Concentration

Dopant concentration is included in analytical equations of focal length for end pumped rod laser crystals [55], and side pumped slab lasers [56]. However, for side pumped rod lasers dopant concentration was not included since it is difficult to define analytically the ray tracing structure on the barrel surface of a rod, since it depends on the cooling tube, used laser rod size, distance of pump source etc. In addition, calculations computed in order to define the effect of thermal distortions on laser, started with the assumption that absorbed power density is uniformly

distributed throughout the crystal volume [5]. However, absorption profile of pump radiation is dependent on pump structure and dopant concentration (Table A2.1-4). Although it is difficult to include dopant concentration in analytical calculations, it is possible to include it in numerical calculations as it was done throughout this work.

Calculations carried out in this study reveal the effect of dopant concentration in Nd:YAG ceramics on continuous wave operating lasers with rod shaped active medium and side pumped pump structure. Material properties of single crystal Nd:YAG were used but the results can be applied to ordinary ceramic materials as well.

Our results show that by increasing dopant concentration it is possible to decrease maximum temperature (Figure 4.1) and stress (Figure 4.12) in laser medium and consequently it is possible to improve efficiency and beam properties, since temperature and stress are the main cause of optical distortions.

We showed that by increasing dopant concentration there is possibility to decrease the effects of thermal distortions on laser beam (Figure 5.7), which seems to be in contradiction with the results of Sennaroglu [57], where it was observed that in end-pumped Nd:YVO₄ continuous wave (cw) lasers, increase in dopant concentration tends to decrease both efficiency and output power of a laser. However, it should be noted that in that study [57], laser rods, having lengths inversely proportional to doping concentration, were end pumped. Absorbed power was almost equal for each sample and laser crystals were conductively cooled through a cooper case kept at constant temperature. Copper case temperature was the same for each sample, but since the cooling surface is decreasing with increase in dopant concentration, cooling efficiency is decreasing. Therefore, by that study it is difficult to conclude on the effects of dopant concentration since more heat is stored in the sample with high dopant concentration due to insufficient cooling.

In our computations, we kept the material size the same for each dopant concentration. So the power that can be extracted is directly related to the absorbed power distribution that is a function of dopant concentration.

Birefringence which results in loss through depolarization in linearly polarized lasers is one of the inherent problems in solid-state lasers. In our study,

depolarization is found to decrease in $\langle 111 \rangle$ oriented ceramic laser materials by increase in dopant concentration (Figure 5.7). However, Shoji et al. [46], experimentally show that depolarization is increasing with increase in dopant concentration under non-lasing condition. In a later study by Shoji et al. [58] it was shown that under lasing conditions depolarization is much less than those under non-lasing conditions, but different dopant concentrations were not considered. Also Khazanov [47] theoretically and Mukhin et al. [48] experimentally showed that by increase in rod length to average grain size ratio in ceramics it is possible to decrease depolarization. Although dopant concentration is not mentioned in these two studies, it is known that to obtain ceramics with high dopant concentrations, average grain size should be decreased [59].

Shoji et al. [45] showed that depolarization in $\langle 100 \rangle$ and $\langle 110 \rangle$ crystals, is low than the $\langle 111 \rangle$ oriented single crystals. Since ceramics are constituted from differently oriented single crystal grains, it should be expected that depolarization will decrease compared to $\langle 111 \rangle$ oriented single crystals.

It can be concluded that in ceramic laser materials there is a 3-fold mechanism that decreases total depolarization; (1) different grain orientations, (2) increase in rod length to average grain size ratio and (3) increase in dopant concentration.

In this study, efficiency of laser was not considered directly, but Ikesue [16] has showed that laser efficiency is decreasing with increase in dopant concentration. Again, samples were end-pumped and sample sizes are not mentioned. It was concluded that increase in grain boundary is the reason for efficiency decrease [16]. Since there is decrease in average grain size in ceramic material with increase in dopant concentration [59], there is increase in grain boundary also, giving rise to scattering loss of laser radiation. However, it is possible to increase efficiency in linearly polarized laser, through decrease in depolarization with increase in dopant concentration.

Up to date, there are no reports on variation of M^2 value with dopant concentration. However, there are analytical equations that relate M^2 to resonator stability parameters [60] and to rod diameter and dioptric power of thermal lens [61].

M^2 value of a laser beam is affected from both resonator parameters and thermal lens induced through pumping. Wyss et. al. [62] related both resonator and thermal lensing parameters to predict the M^2 value in plane-plane resonators. Equation given in [62] can be modified as a function of thermal lens as given in Eq. (6.2).

$$M^2(f) = \frac{\pi r^2}{4\lambda} \sqrt{\frac{1}{f} \left(\frac{4}{L_R} - \frac{1}{f} \right)} + \frac{1}{2} \quad (6.2)$$

From this equation it can be stated that with increase in focal length there will be decrease in M^2 value, which means improvement in beam quality. In our work it was shown that, by increasing dopant concentration it is possible to increase the focal length of thermal lens induced under lasing conditions with increase in dopant concentration. This will cause decrease in M^2 and beam quality of laser beam can be increased.

TEM₀₀ mode operation can be considered for rods that have pumped central regions for all dopant concentrations. That is, it is hard to state that it is possible to obtain TEM₀₀ mode oscillation in rods with high dopant concentration and 808 nm pump source since the central parts of the rods are completely unpumped (Table A2.1 and Table A2.2). Also it was shown that as dopant concentration is increasing absorbed pump power moves towards the rod surface leaving central parts with less absorbed power or even unpumped, leading to efficiency decrease. Efficiency decrease is a consequence of the limiting size of operation of the fundamental mode. Murdough and Denman [63] calculated that the radius of a cylindrical volume in which TEM₀₀ oscillation can be obtained is limited to 1.1 mm independent of rod diameter. Also in [61], it was stated that fundamental mode can be only obtained in regions where there is no depolarization. In addition, while absorbed power is increasing there is decrease in available volume for the operation of TEM₀₀ mode [61].

Our results show that, there is increase in available region of TEM₀₀ mode with increase in dopant concentration but this leads to decrease in available laser power in that region. Therefore, there is need for optimization of available laser

power and laser beam size in case of TEM₀₀ operation. In addition, laser rods with small radius and low dopant concentration are more suitable for TEM₀₀ operation since absorbed power and power density at central regions are higher compared to rods with high radius and high dopant concentration (Figure 3.8-3.11)

6.3 Effect of Pump Structure

Pump structure is not of consideration in literature; however the distribution of absorbed power is discussed [5], [64]. Best beam of a solid-state laser can be obtained if absorbed power is uniformly distributed through the lasing region. Due to this fact in analytical calculations, assumption of uniformly absorbed power is used [5].

Distribution of absorbed power depends on the intensity distributions of pump source, geometry and refractive index of cooling sleeve, laser rod size, and the distance of pump source from the cooling tube surface. In computations carried out through this work, four different fold structures were used. Geometrical values of cooling tube, distance of pump source from cooling tube surface and pump beam intensity distribution were kept constant since we are interesting in influence of dopant concentration. However, from our investigations we can obtain some general rules about side pumping of solid-state laser rods with laser diodes.

From our results we can observe that keeping all other factors constant higher fold structures result in more uniform absorbed power distribution (Table A2.1-4). However, if the distance between cooling tube and laser diode is increased in lower fold structures, uniformity of absorbed power can be enhanced.

One of the main advantages of solid-state lasers is their compactness. To obtain desired absorbed power distribution there should be a decision between using high or lower fold structures. Since lower fold structures will result in larger resonators while high fold structures will produce compact resonators with more parts.

In addition, it should be noted that, due to the intensity distribution of laser diode pump sources it is not possible to obtain uniform absorbed power distribution through the active laser volume.

In pumping of small rod diameters it will be preferable to use lower fold structure but as the rod size is increasing fold structure should be increased.

Our result show that as far as the uniformity of absorbed power is considered there is no much difference in the temperature values induced in the rod (Figure 4.1). However as the uniformity is destroyed temperatures are higher in lower fold structures (Figure 4.1).

Temperature gradients are in direct relation with the pump structure, higher gradients are induced in lower fold pump structures (Figure 4.3). In addition, stress components like radial (Figure 4.5), azimuthal (Figure 4.7) and shear (Figure 4.11) stresses are affected from the pump structure. However, axial (Figure 4.9) and von Mises (Figure 4.12) stresses like temperature are not affected by pump structure if absorbed power is almost uniform.

Focal lengths (Figure 5.8, Figure 5.9) seem to be not affected from pump structure if uniformity is obtained but components of focal length (Figure 5.11, Figure 5.12) are affected. This implies that aberrations induced in lower fold structures are higher than the ones induced in higher fold structure.

So fold structure should be optimized considering the beam properties of the laser to be obtained and number of components, which lead to difficulties in construction of a laser resonator.

6.4 Effect of Pump Wavelength

Two different pump wavelengths were used through the computations, 808 nm and 885 nm. Quantum defect between 808 nm pump wavelength and 1064 nm laser wavelength is higher compared to 885 nm one, which increases the loss of

available laser power in the laser medium of 808 nm pumped Nd:YAG lasers. This leads to higher temperatures (Figure 4.1), higher stresses (Figure 4.12), higher depolarization (Figure 5.7) and lower thermal lens focal lengths (Figure 5.8, Figure 5.9) in 808 nm source pumped laser Nd:YAG materials compared to 885 nm source pumped ones.

In addition 808 nm wavelength has higher absorption coefficients compared to 885 nm one (Figure 3.2). This difference in absorption coefficient leads to different application places of the two pump source. Generally we can state that 808 nm pump sources are suitable for pumping of laser rods with smaller diameter, while 885 nm is suitable for rods with large diameters. This division of application places arises from the fact that as the absorption coefficient is increasing distance in which it will be completely absorbed is decreasing, according to Beer's law, and vice versa.

Availability of highly doped ceramic Nd:YAG laser materials make it possible to replace Nd:YVO₄ crystal with ceramic Nd:YAG pumped with 808 nm source in high power microchip laser [65]. Furthermore, 885 nm pump source that have lower absorption coefficient, can be used effectively in large area pumped solid-state lasers [34].

CHAPTER 7

CONCLUSION

In this thesis, numerical calculations were carried out to predict the effect of dopant concentration in Nd:YAG ceramics on continuous wave operating lasers with rod shaped active medium and side pumped pump structure. Material properties of single crystal Nd:YAG were used but the results can be applied to ordinary ceramic materials as well.

Our results show that by increasing dopant concentration it is possible to decrease maximum temperature and stress in a solid-state laser medium and consequently to improve efficiency and beam properties of a solid-state laser, since temperature and stress are the main cause of optical distortions.

Birefringence, which results in loss through depolarization in linearly polarized lasers is one of the inherent problems in solid-state lasers. In our study, depolarization is found to decrease in $\langle 111 \rangle$ oriented ceramic laser materials by increase in dopant concentration. So, decrease in depolarization with increase in dopant concentration results in increase of efficiency in linearly polarized lasers.

Furthermore, it was shown that, by increasing dopant concentration it is possible to increase the focal length of thermal lens induced under lasing conditions with increase in dopant concentration. This will possibly cause decrease in M^2 value of a multi-mode laser beam.

It is observed that when TEM_{00} mode operation is considered, low concentration rods are more suitable, since efficiency will be greater compared to highly doped ones.

Pump structure was also one of the parameters considered in the calculations. In pumping of small rod diameters, it is preferable to use lower fold

structure but as the rod size increases number of folds should be increased in order to get desired absorbed pump power uniformity.

Two different pump wavelengths were used through the computations, 808 nm and 885 nm. Generally, we can state that 808 nm pump sources are suitable for pumping of laser rods with smaller diameter and higher concentration, while 885 nm is suitable for rods with large diameters and low concentration.

Although numerical results state that it is possible to improve laser beam properties it is not verified experimentally yet. Future work of this study should include 3D numerical analysis and experimental verification of the results obtained.

REFERENCES

- 1- J.E. Guesic, H.M. Marcos, L.G. Van Uiter, *Appl. Phys. Lett.* 4, 182-184 (1964)
- 2- K. Shiroki and Y. Kuwano, *J. Jpn. Chem. Soc.*, 7, 940 (1978)
- 3- VLOC Incorporated, YAG Brochure, <http://www.vloc.com/PDFs/YAGBrochure.pdf>, 21.12.2006
- 4- M. Katsurayama, Y. Anzai, A. Sugiyama, M. Koike, and Y. Kato, *J. Cryst. Growth*, 229 [1] 193–198 (2001)
- 5- W. Koechner, *Solid-State Laser Engineering*, Springer-Verlag, Berlin, (1999)
- 6- C. Greskovich, K. N. Woods, and J. P. Chernoch, *Am. Ceram. Soc. Bull.*, 51 [4] 324–325 (1972)
- 7- C. D. Greskovich and J. P. Chernoch, *J. Appl. Phys.*, 44, [10], 4599–4606 (1973)
- 8- G. DeWith and H. J. VanDijk, *Mater. Res. Bull.*, 19, [12], 1669–674 (1984)
- 9- M. Sekita, H. Haneda, S. Shirasaki, and T. Yanagitani, *J. Appl. Phys.*, 69 [6] 3709–3718 (1991)
- 10- A. Ikesue, A. Furusato, and K. Kamata, *J. Am. Ceram. Soc.*, 78 [1] 225–228 (1995)
- 11- A. Ikesue, T. Kinoshita, K. Kamata, and K. Yoshida, *J. Am. Ceram. Soc.*, 78 [4] 1033–1040 (1995)
- 12- I. Shoji, S. Kurimura, Y. Sato, T. Taira, A. Ikesue and K. Yoshida, *Appl. Phys. Lett.* 77, 939-941 (2000)
- 13- G. A. Kumar, J. Lu, A. A. Kaminski, K. Ueda, H. Yagi, T. Yanagitani, and N. V. Unnikrishnan, *IEEE J. Quantum Electron.* 40, 747-758 (2004)
- 14- M. Dubinskii, L. D. Merkle, J. R. Goff, G. J. Quarles, V. K. Castillo, K. L. Schepler, D. Zelmon, S. Guha, L. P. Gonzalez, M. R. Rickey, J. J. Lee, S. M. Hegde, J. Q. Dumm, G. L. Messing, and S. Lee, *Laser Source and System Technology for Defense and Security, Proc. SPIE 5792*, 1-9 (2005)

- 15- S. Lee, S. Kochawattana, G. L. Messing, J. Q. Dumm, G. Quarles and V. Castillo, *J. Am. Ceram. Soc.* 89, 1945–1950 (2006)
- 16- A. Ikesue and Y. L. Aung, *J. Am. Ceram. Soc.*, 89, 1936–1944 (2006)
- 17- J. Lu, M. Prabhu, J. Song, C. Li, J. Xu, K. Ueda, A.A. Kaminskii, H. Yagi and T. Yanagitani, *Appl. Phys. B* 71, 469–473 (2000)
- 18- V. Lupei, A. Lupei, S. Georgescu, T. Taira, Y. Sato and A. Ikesue, *Phys. Rev. B* 64, 092102(1-4) (2001)
- 19- V. Lupei, A. Lupei, N. Pavel, T. Taira, I. Shoji and A. Ikesue, *Appl. Phys. Lett.* 79, 590-592 (2001)
- 20- Baikowski Chimie, Technical Data, http://www.baikowski.com/components/pdf/ceramic_yag/YAG_DATA_SHEET.pdf, 21.12.2006
- 21- A. Ikesue, *Opt. Mat.*, 19, 183-187 (2002)
- 22- T. Taira, A. Ikesue, and K. Yoshida, in *OSA Trends in Optics and Photonics, Vol 19, Advanced Solid-State Lasers*, edited by W. R. Bosenberg and M. M. Fejer (Optical Society of America, Washington, DC, 1998), p.430
- 23- H. Yagi, T. Yanagitani, T. Numazawa, and K. Ueda, *Ceramics International*, (2006)
- 24- L. Mezeix, D. J. Green, *Int. J. Appl. Ceram. Technol.*, 3 ,166-176 (2006)
- 25- Konoshima Chemical Co. Ltd., Materials, <http://www.konoshima.co.jp/en/yag.html>, 21.12.2006
- 26- J. Lu, M. Prabhu, J. Xu, K. Ueda, H. Yagi, T. Yanagitani, A.A. Kaminskii, *Appl. Phys. Lett.* 77, 3707-3709 (2000)
- 27- J. Lu, J. Song, M. Prabhu, J. Xu, K. Ueda, H. Yagi, T. Yanagitani, A.A. Kaminskii, *Jpn. J. Appl. Phys.*, 39, 1048-1050 (2000)
- 28- J. Lu, T. Murai, K. Takaichi, T. Uematsu, K. Misawa, M. Prabhu, J. Xu, K. Ueda, H. Yagi, T. Yanagitani, A. A. Kaminskii and A. Kudryashov, *Appl. Phys. Lett.* 78, 3586-3588 (2001)
- 29- Y. Qi, X. Zhu, Q. Lou, J. Ji, J. Dong, and Y. Wei, *Opt. Express* 13, 8725-8729 (2005)
- 30- S. Lee, D. Choia, C. Kim and J. Zhou , *Optics & Laser Technology* (2006)
- 31- D. Kracht, D. Freiburg, R. Wilhelm, M. Frede, C. Fallnich, *Opt. Express* 14, 2690-2694 (2006)

- 32- V. Lupei, A. Lupei, N. Pavel, T. Taira, I. Shoji and A. Ikesue, *Appl. Phys. Lett.* 79, 590-592 (2001)
- 33- V. Lupei, N. Pavel, in *Solid State Lasers and Amplifiers II*, A. Sennaroglu, eds., *Proc. SPIE* 6190, 1-8 (2006)
- 34- Lawrence Livermore National Laboratory, Science&Technology, <http://www.llnl.gov/str/April06/Soules.html>, 21.12.2006,
- 35- V. Lupei, A. Lupei, *Opt. Eng.* 35, Iss. 5, pp. 1252-1257, (1996)
- 36- T.Y. Fan, *IEEE Journal of Quantum Electronics*, Vol. 29, No. 6, (1993)
- 37- S. Goldring, R. Lavi, A. Tal, E. Lebiush, Y. Tzuk, and S. Jackel, *IEEE Journal of Quantum Electronics*, Vol. 40, No. 4, (2004)
- 38- F.P. Incropera, *Fundamentals of heat and mass transfer*, 4th Ed., John Willey & Sons, New York, (1996)
- 39- S. Timoshenko, J.N. Goodier, *Theory of Elasticity*, 3rd Ed. , McGraw- Hill, Singapore, (1982)
- 40- J.E. Nye, *Physical Properties of Crystals*, 2nd Ed., Oxford University Press, London, (1964)
- 41- D.C. Brown, *IEEE Journal of Quantum Electronics*, Vol. 34, No. 12, 1998,
- 42- N. Noda, R. B. Hetnarski, Y. Tanigawa, *Thermal Stresses*, 2nd Ed., Taylor&Francis, New York, (2003)
- 43- ANSYS Release 9.0 Documentation, (2004)
- 44- LIGO-Wave Observatory, Index of docs/G, <http://www.ligo.caltech.edu/docs/G/G010362-00.pdf>, 15 Aug 2001
- 45- I. Shoji and T.Taira, *Appl. Phys. Lett.*, Vol. 80, No.17, pp.3048-3050, (2002)
- 46- I. Shoji, Y. Sato, S.Kurimura, V. Lupei, T. Taira, A. Ikesue, K. Yoshida, *Opt. Lett.* , Vol. 22, No.4, pp.234-236, (2002)
- 47- E.A. Khazanov, *Opt. Lett.* , Vol. 27, No.9, pp.716-718, (2002)
- 48- I.B. Mukhin, O.V. Palashov, E.A. Khazanov, A. Ikeseu and Y.L. Aung, *Opt. Express* Vol. 13, No.16, pp. 5983-5987, (2006)
- 49- M.P.MacDonald, Th. Graf, J.E. Balmer, H.P. Weber, *Opt. Commun.*, Vol.178, pp. 383-393, (2000)
- 50- C.Pfistner, R. Weber, H.P. Weber, S. Merazzi, R. Gruber, *IEEE Journal of Quantum Electronics*, Vol. 30, No. 7, (1994)

- 51- R. Weber, B. Neuenschwander, M. Mac Donald, M.B. Roos, H.P. Weber, IEEE Journal of Quantum Electronics, Vol. 34, No.6, pp.1046-1053 , (1998)
- 52- R. Weber, B. Neuenschwander, H.P. Weber, Opt. Materials, Vol.11, pp.245-254, (1999)
- 53- A.E. Siegman, Lasers, University Science Books, California, (1986)
- 54- B. Chen, Y. Chen, J. Simmons, T.Y. Chung, M. Bass, Appl. Phys. B, Vol. 82, pp. 413-418, (2006)
- 55- M.E. Innocenzi, H.T. Yura, C.L. Fincher, R.A. Fields, Appl. Phys. Lett. 56, 1831-1833, (1990)
- 56- T. S. Rutherford, W. M. Tulloch, E. K. Gustafson, R. L. Byer, IEEE J. Quantum Electron. 36, 205-219, (2000)
- 57- A. Sennaroglu, Optical and Quantum Electron. 32, 1307-1317, (2000)
- 58- I. Soji, T. Taira, A. Ikesue, K. Yoshida, OSA Trends in Optics and Photonics Series, Advanced Solid State Photonics 94, 416-418, (2004)
- 59- R. Kawai, Y. Miyasaka, K. Otsuka, T. Ohtomo, T. Narita, J.Y. Ko, I. Shoji, T. Taira, Opt. Express 12, 2293-2302, (2006)
- 60- N. Hodgson, H. Weber, Laser Resonators and Beam Propagation, Springer-Verlag, New York, (2005)
- 61- G. Mann, S. Seidel, H. Weber, in Laser Resonators Novel Design and Development, Ed. A.V. Kudryashov, H. Weber, SPIE, Washington, (1999)
- 62- E. Wyss, T. Graf, H. P. Weber, IEEE J. Quantum Electron. 41, 671-676, (2005)
- 63- M. P. Murdough, C. A. Denman, Appl. Opt. 35, 5925-5936, (1996)
- 64- R. Ifflander, Solid-State Lasers for Materials Processing, Springer-Verlag, Berlin, (2001)
- 65- A. Ikesue, Y. L. Aung, T. Taira, T. Kamimura, K. Yoshida, G.L. Messing, Annu. Rev. Mater. Res. 36, pp. 397-429, (2006)
- 66- Weber, M.J., Handbook of Optical Materials, CRC Press, New York, (2003)

APPENDIX I

MATERIAL PROPERTIES

A1.1 Mechanical Properties

Density – 4.55 g/cm³ [20]

Table A1. 1 - Youngs Modulus and Poissons Ratio [23]

Temperature (°C)	25	200	400	600	800	1000	1200	1400
Young's Modulus (GPa)	308	304	300	293	287	281	274	264
Poisson's Ratio	0.233	0.238	0.234	0.224	0.228	0.216	0.221	0.23

A1.2 Thermal Properties

Thermal Conductivity

$$k(T) = \frac{a}{\ln(b \cdot T)^c} - \frac{d}{T} \quad , [41] \quad (A1.1)$$

Thermal Expansion

$$\alpha(T) = a \cdot T^b \quad , [41] \quad (A1.2)$$

Thermal variation of refractive index

$$\frac{dn(T)}{dT} = (-3.5 \cdot K^{-1} + 0.0548 \cdot K^{-2} \cdot T - 0.00005 \cdot K^{-3} \cdot T^2) \cdot 10^{-6} \quad , [44] \quad (A1.3)$$

A1.3 Optical Properties

Sellemier Equation for YAG

$$n = \sqrt{1 + \frac{2.293 \cdot \lambda^2}{\lambda^2 - 0.1095^2} + \frac{3.705 \cdot \lambda^2}{\lambda^2 - 17.825^2}} \quad , [66] \quad (A1.4)$$

Elasto-Optic Constants of Nd:YAG

$$p_{11} = -0.029, p_{12} = 0.0091, p_{44} = -0.0615, [5]$$

APPENDIX II

ABSORBED POWER DENSITY DISTRIBUTION

Table A2. 1- Absorbed power density distribution of 3mm rod pumped with 808 nm source

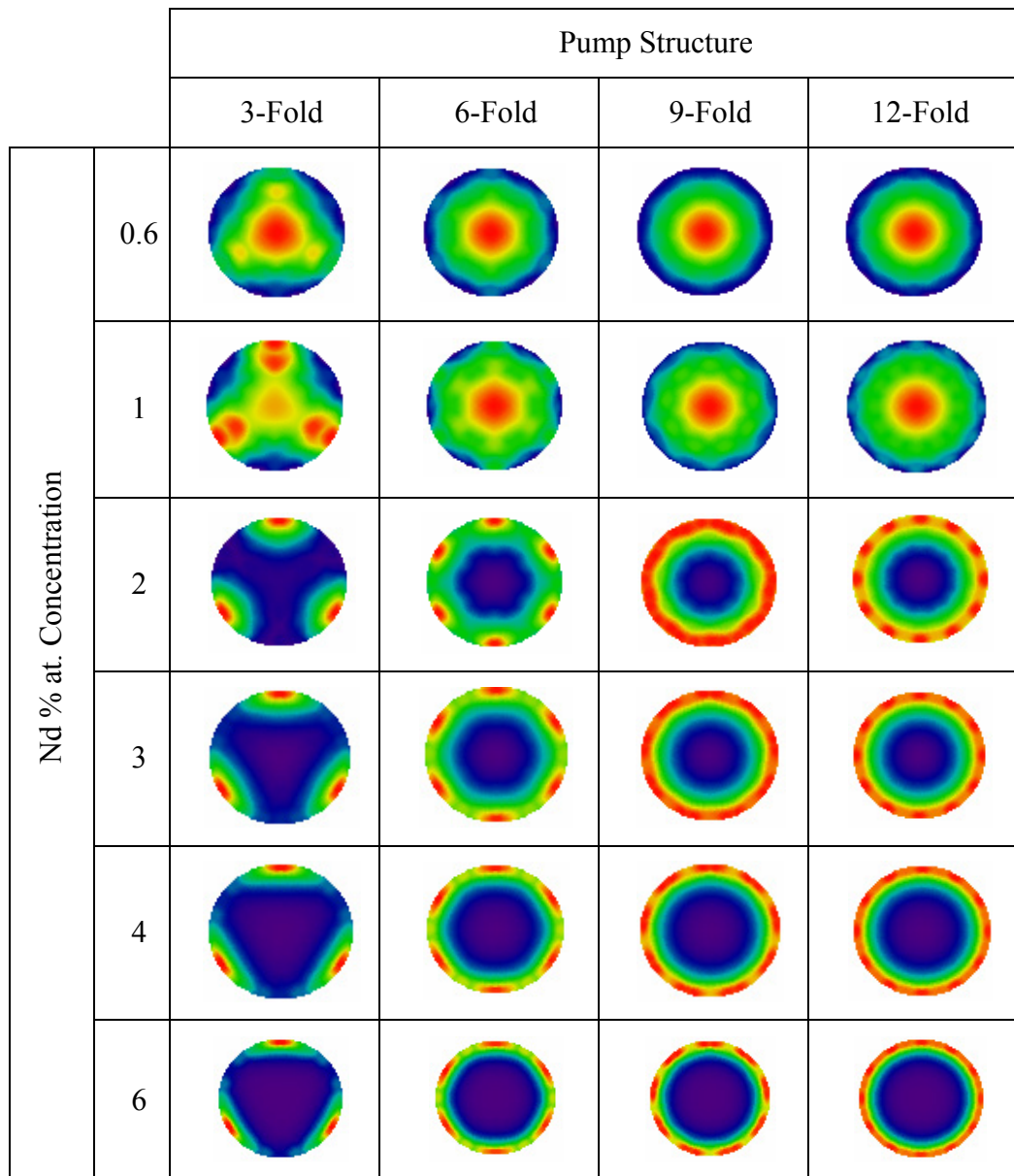


Table A2. 2 - Absorbed power density distribution of 6 mm rod pumped with 808 nm source

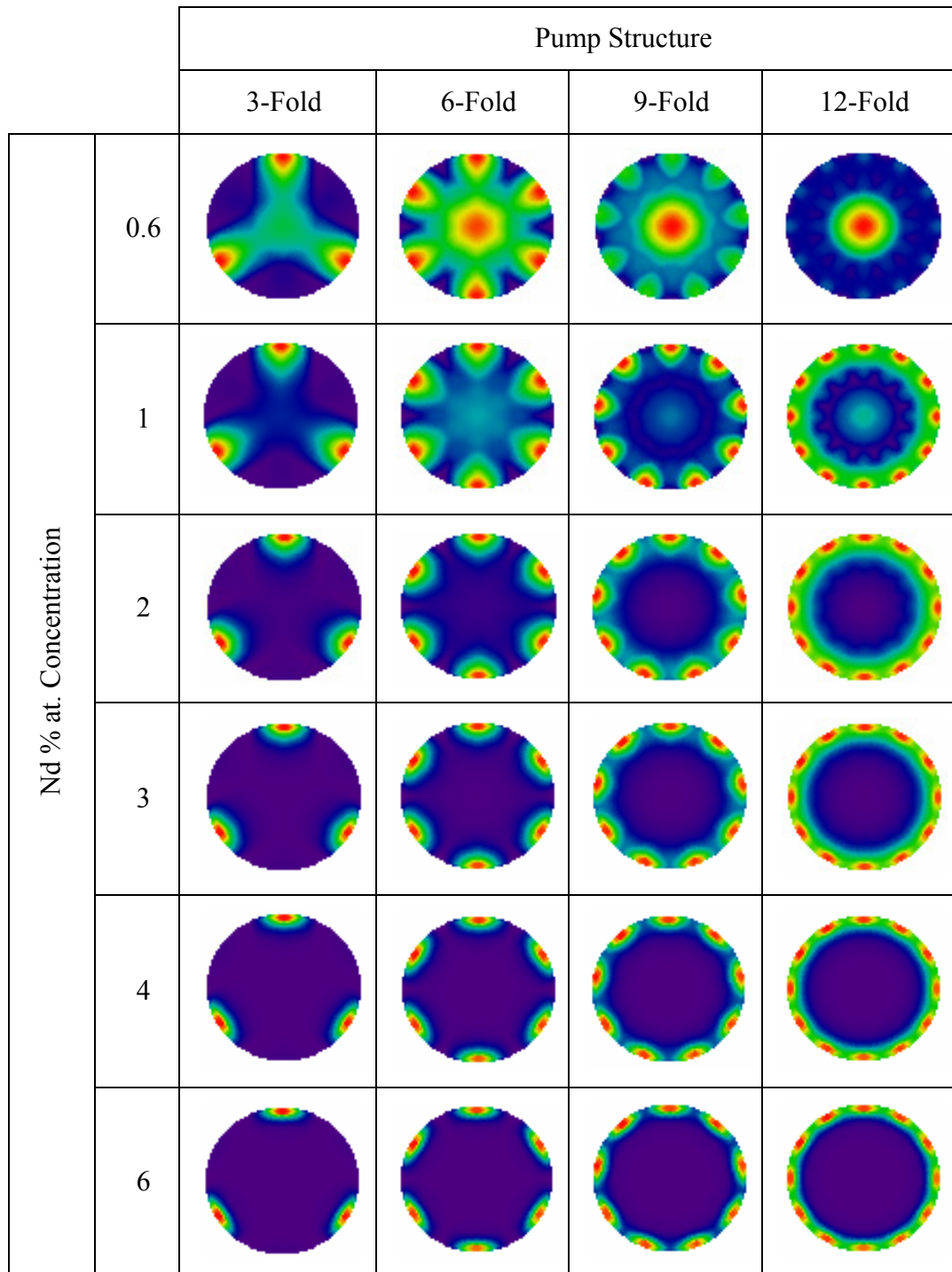


Table A2. 3 - Absorbed power density distribution of 3 mm rod pumped with 885 nm source

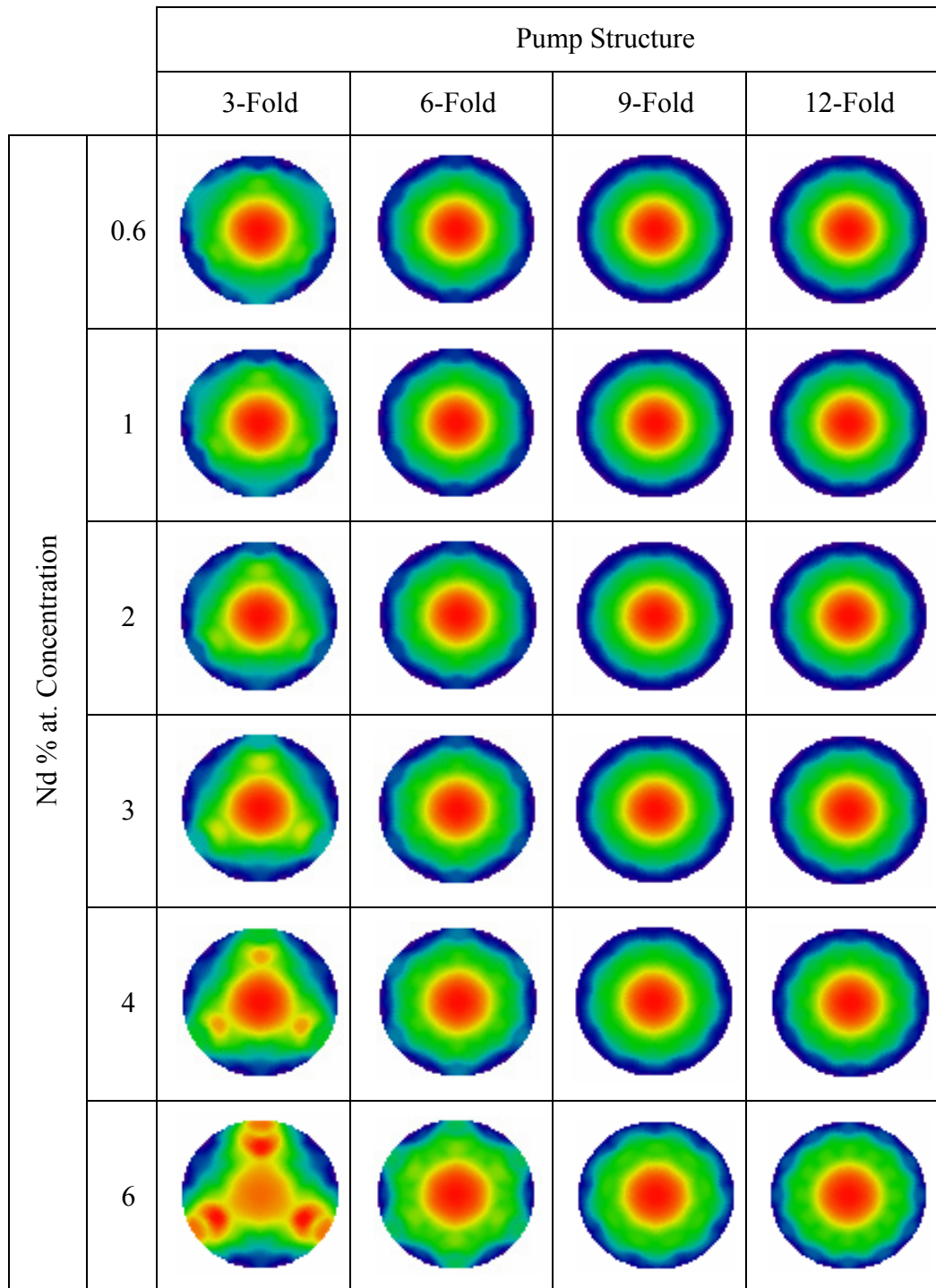
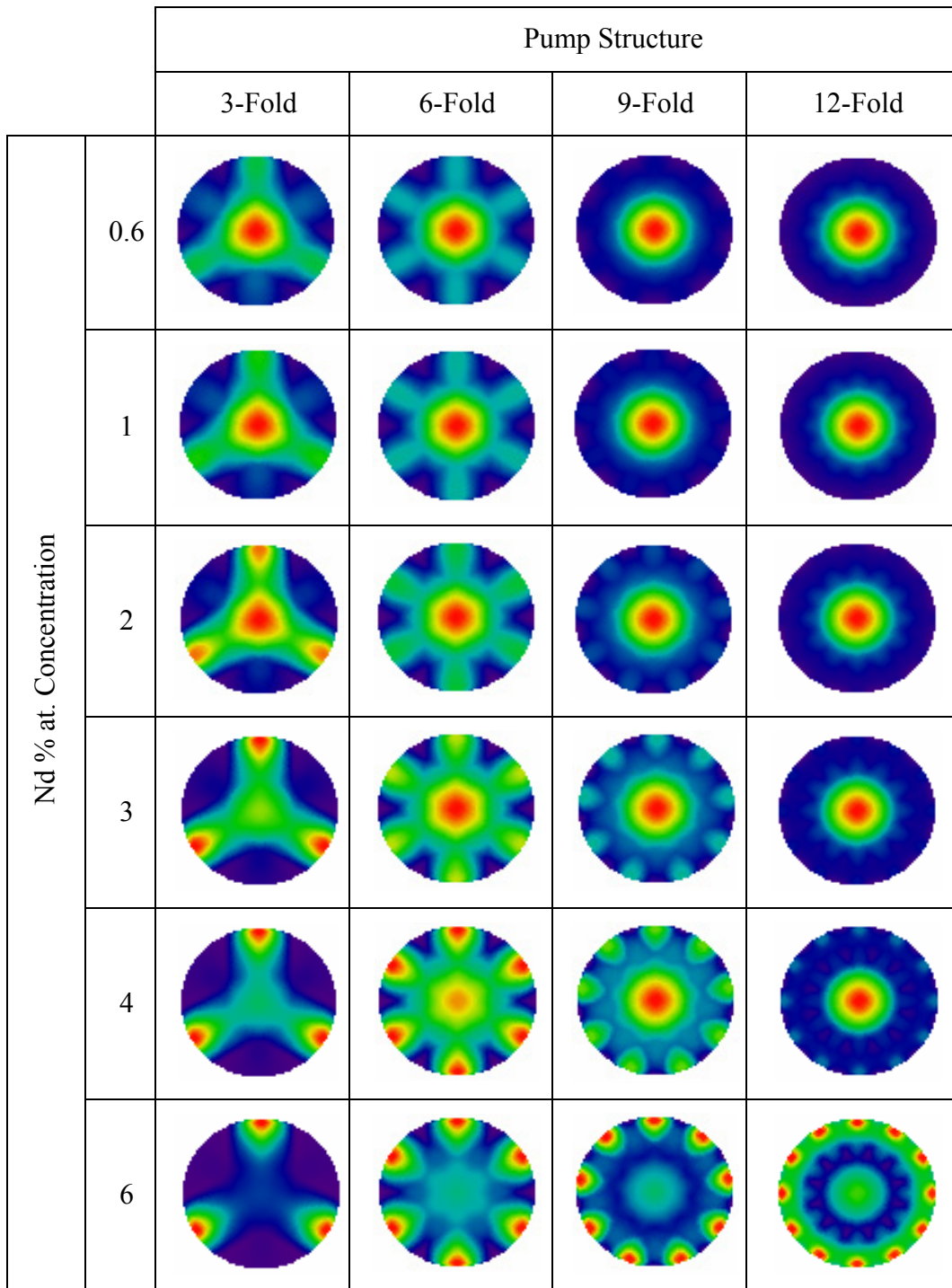


Table A2. 4 - Absorbed power density distribution of 6 mm rod pumped with 885 nm source



APPENDIX III

TEMPERATURE DISTRIBUTION RESULTS

Table A3. 1- Temperature distribution of 3mm rod pumped with 808 nm source

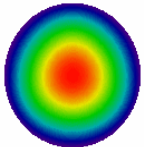
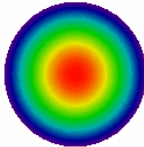
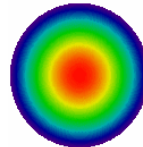
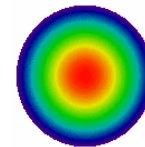
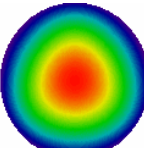
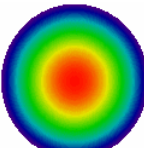
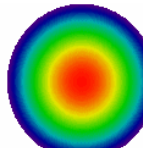
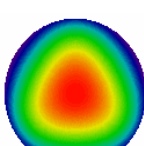
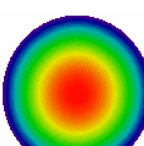
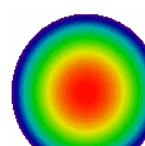
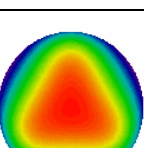
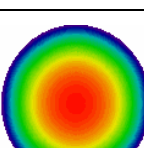
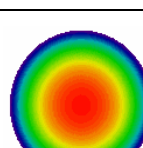
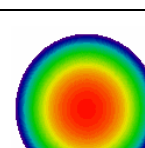
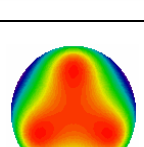
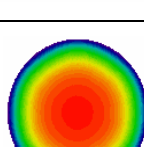
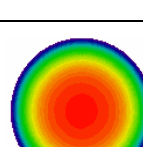
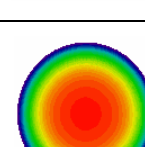
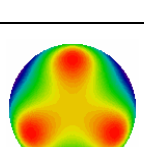
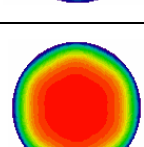
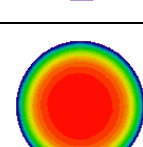
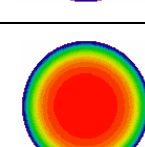
		Pump Structure			
		3-Fold	6-Fold	9-Fold	12-Fold
Nd % at. Concentration	0.6				
	1				
	2				
	3				
	4				
	6				

Table A3. 2- Temperature distribution of 6 mm rod pumped with 808 nm source

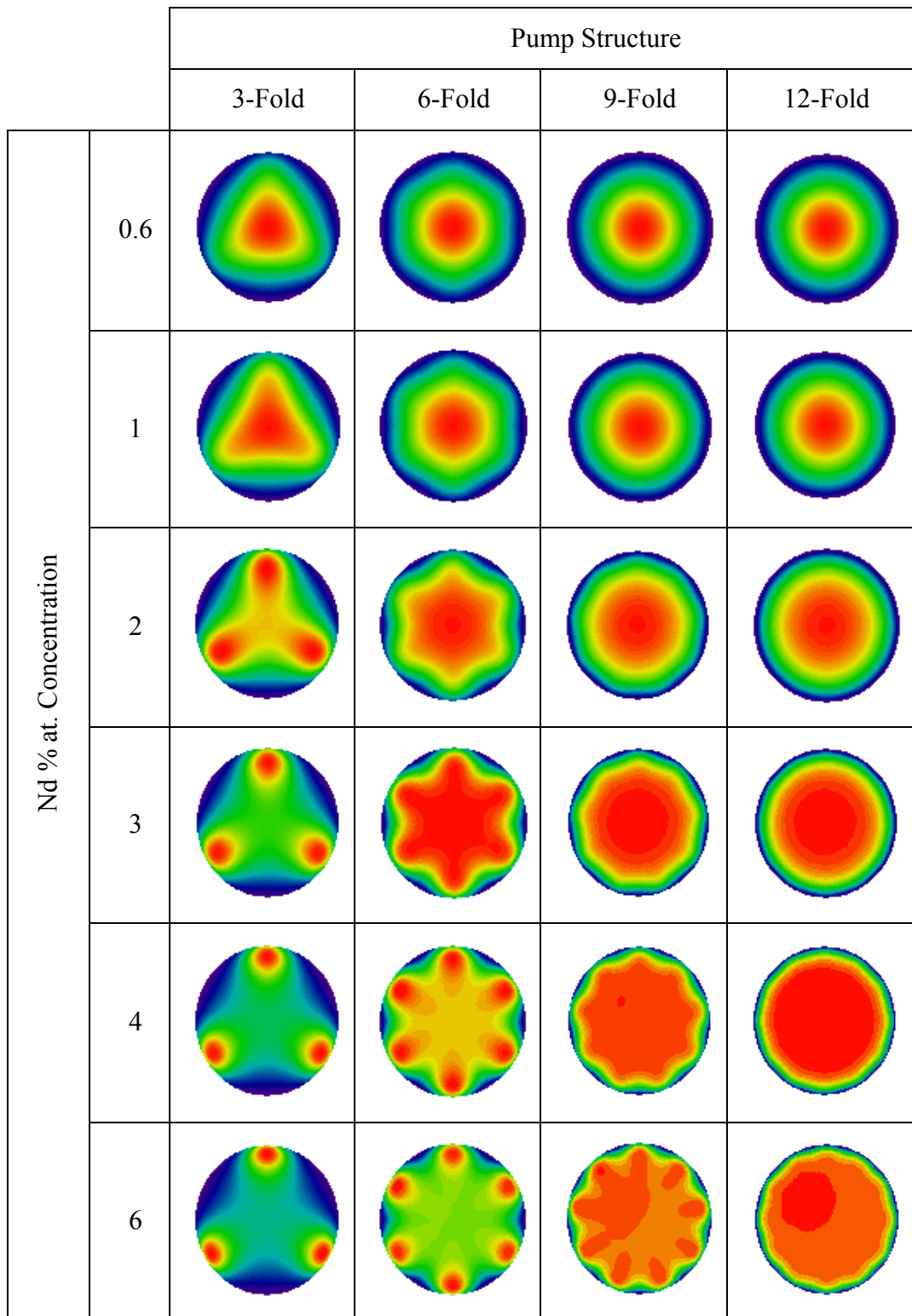


Table A3. 3- Temperature distribution of 3 mm rod pumped with 885 nm source

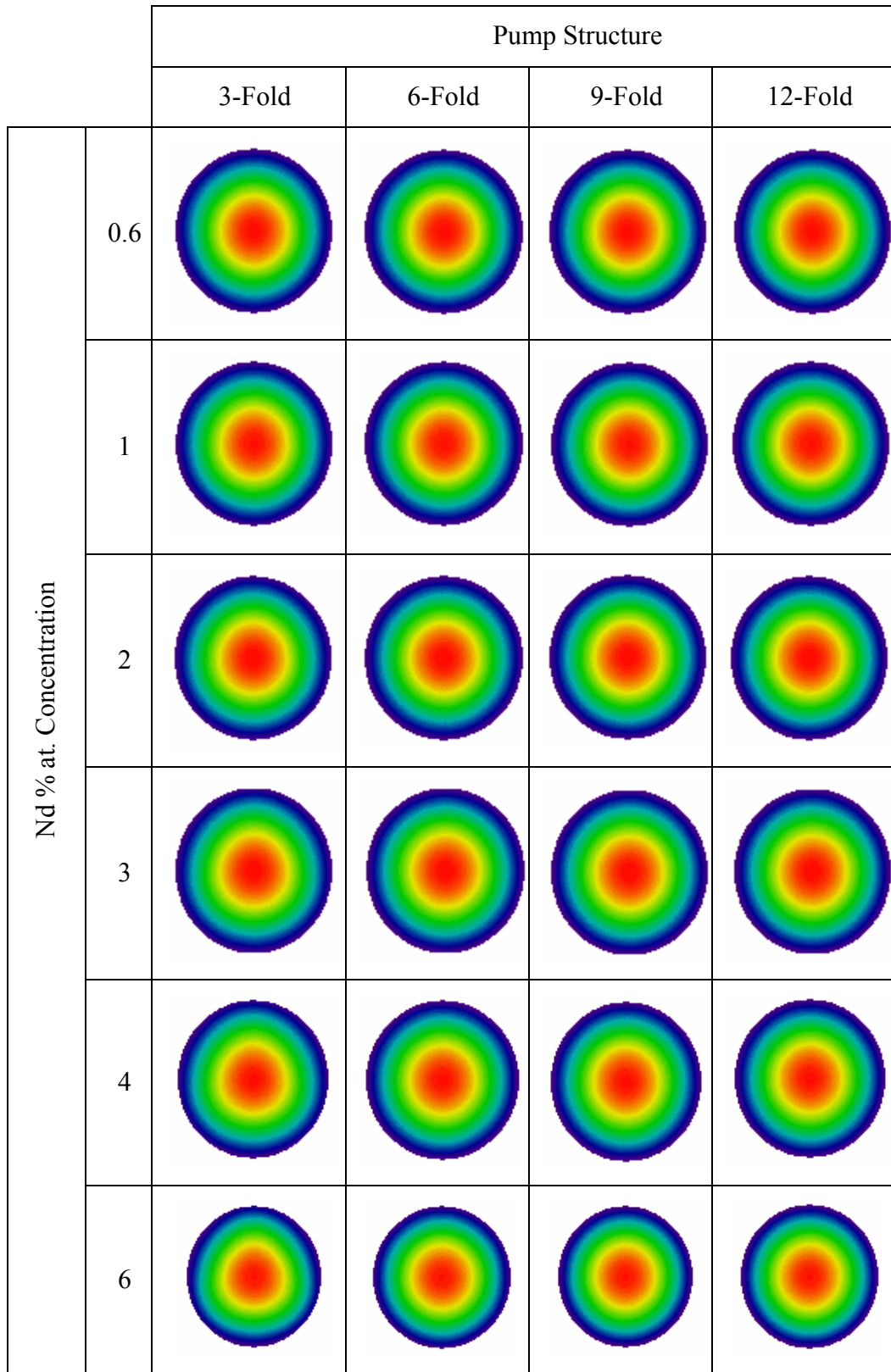
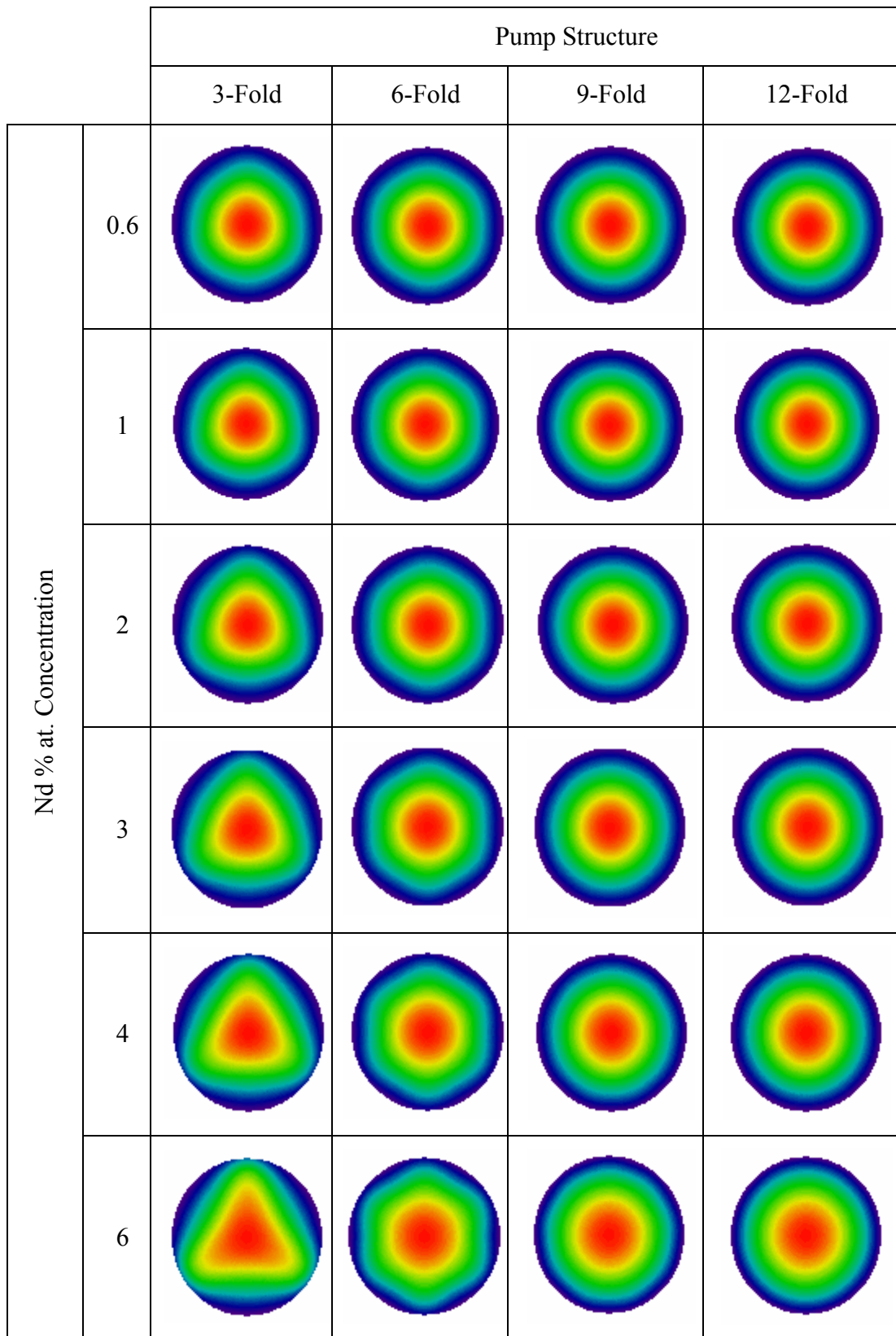


Table A3. 4- Temperature distribution of 6 mm rod pumped with 885 nm source



APPENDIX IV

TEMPERATURE GRADIENT RESULTS

Table A4. 1– Thermal gradient distribution of 3 mm rod pumped with 808 nm source

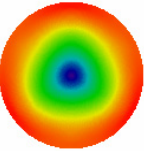
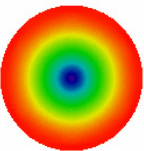
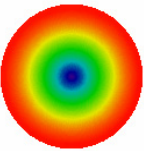
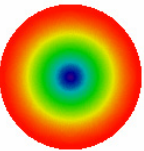
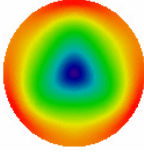
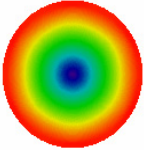
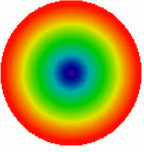
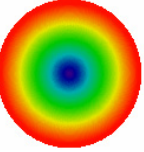
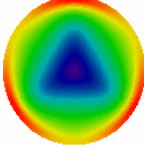
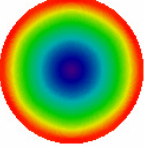
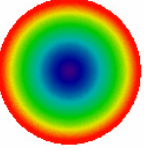
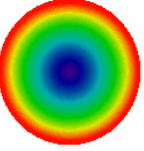
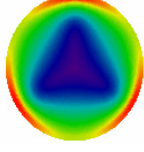
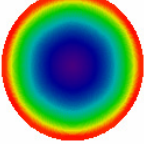
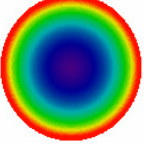
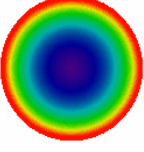
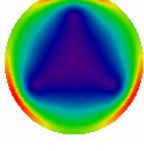
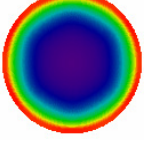
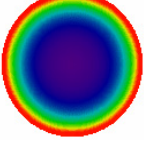
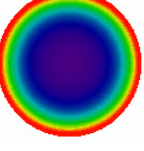
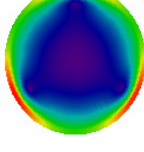
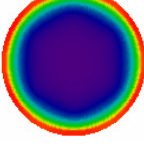
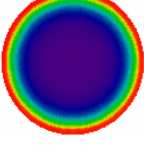
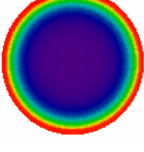
		Pump Structure			
		3-Fold	6-Fold	9-Fold	12-Fold
Nd % at. Concentration	0.6				
	1				
	2				
	3				
	4				
	6				

Table A4. 2- Thermal gradient distribution of 6 mm rod pumped with 808 nm source

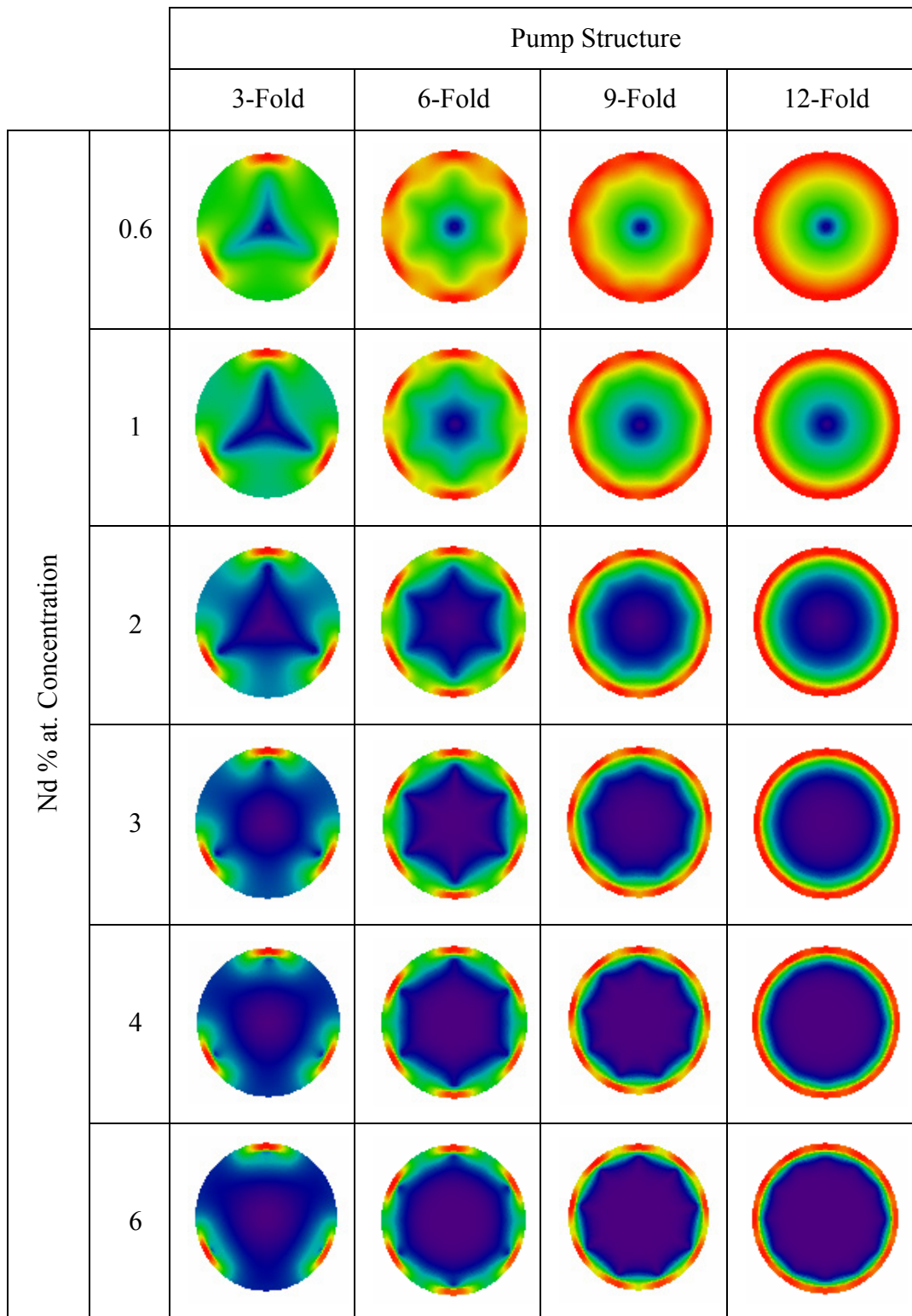


Table A4. 3- Thermal gradient distribution of 3 mm rod pumped with 885 nm source

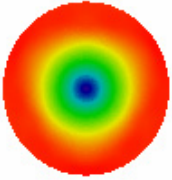
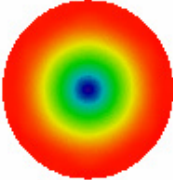
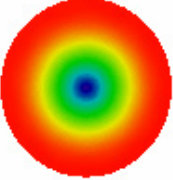
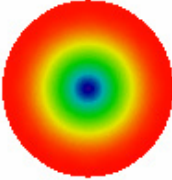
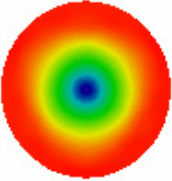
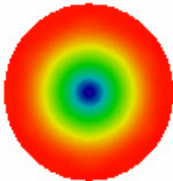
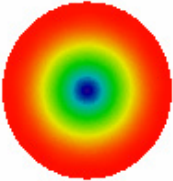
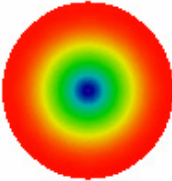
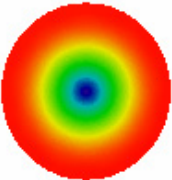
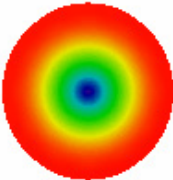
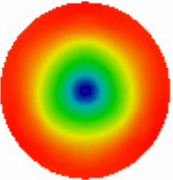
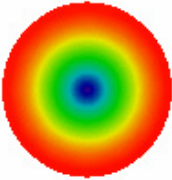
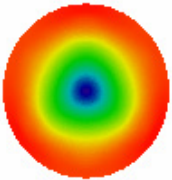
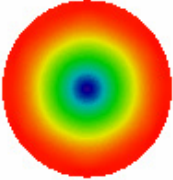
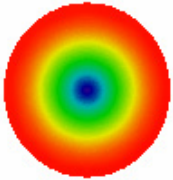
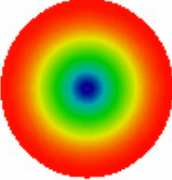
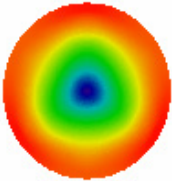
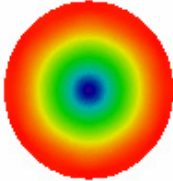
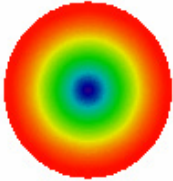
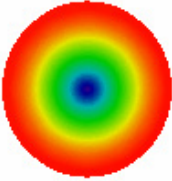
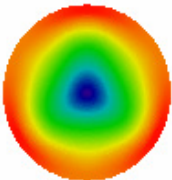
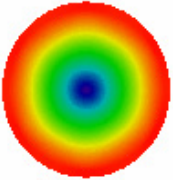
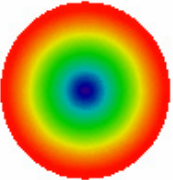
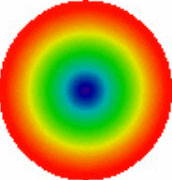
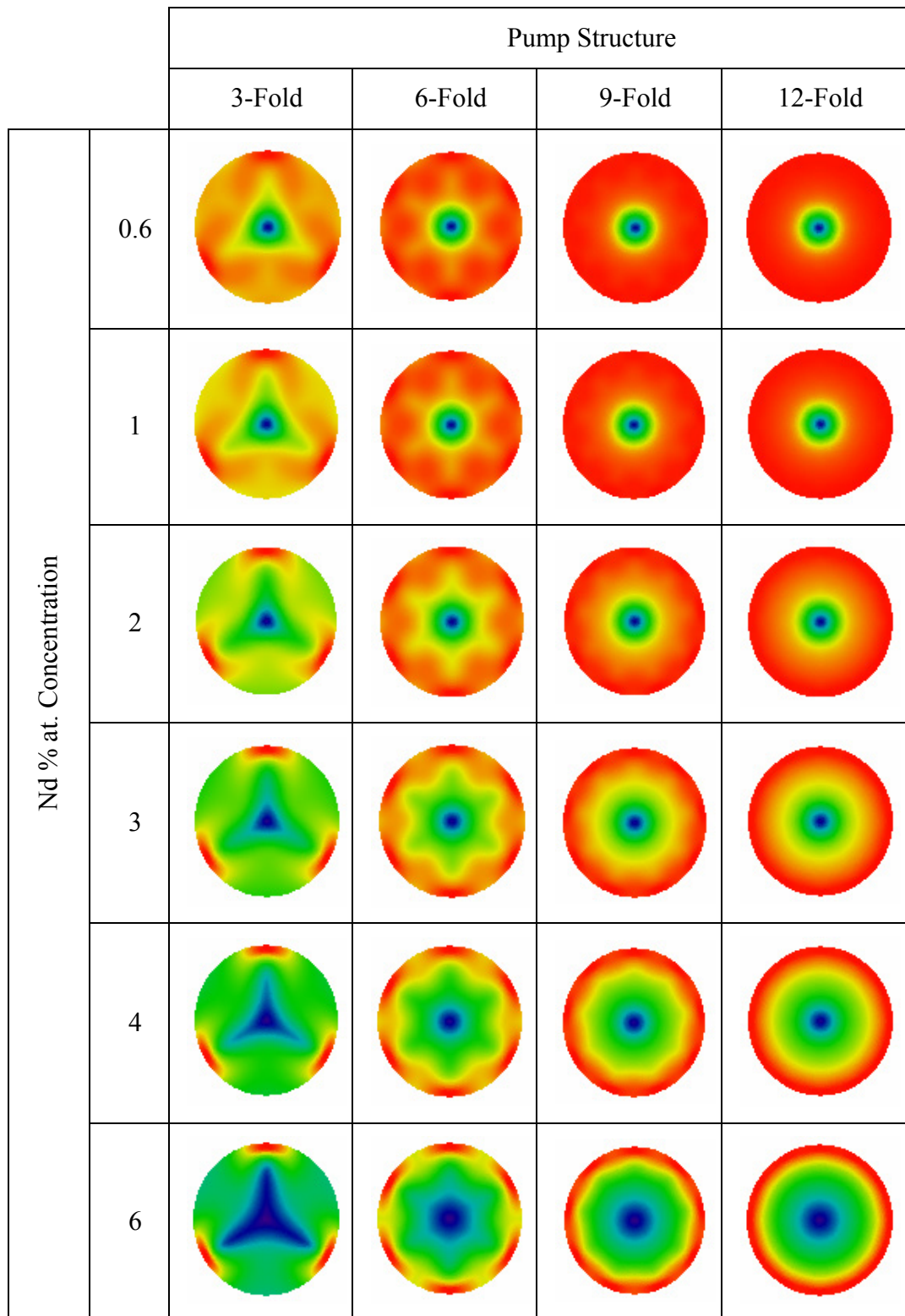
		Pump Structure			
		3-Fold	6-Fold	9-Fold	12-Fold
Nd % at. Concentration	0.6				
	1				
	2				
	3				
	4				
	6				

Table A4. 4- Thermal gradient distribution of 6 mm rod pumped with 885 nm source



APPENDIX V

RADIAL STRESS RESULTS

Table A5.1- Radial stress distribution of 3 mm rod pumped with 808 nm source

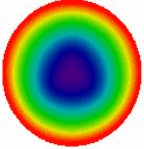
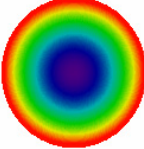
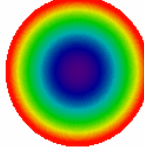
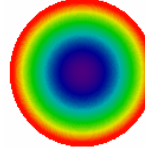
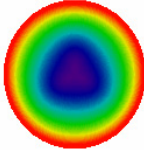
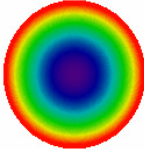
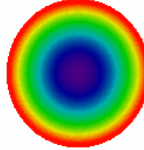
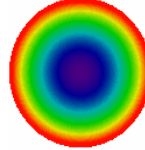
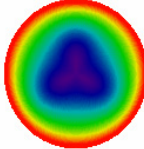
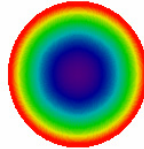
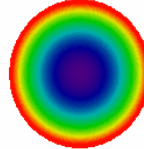
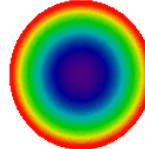
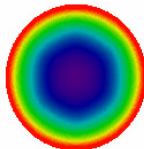
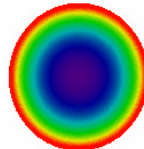
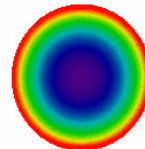
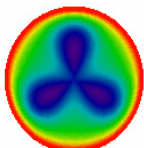
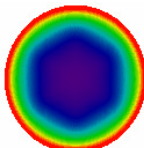
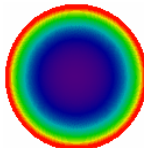
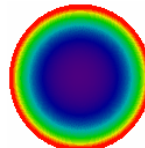
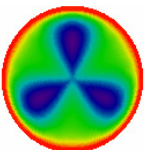
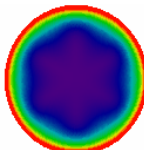
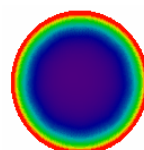
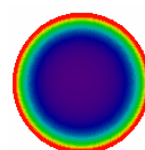
		Pump Structure			
		3-Fold	6-Fold	9-Fold	12-Fold
Nd % at. Concentration	0.6				
	1				
	2				
	3				
	4				
	6				

Table A5.2- Radial stress distribution of 6 mm rod pumped with 808 nm source

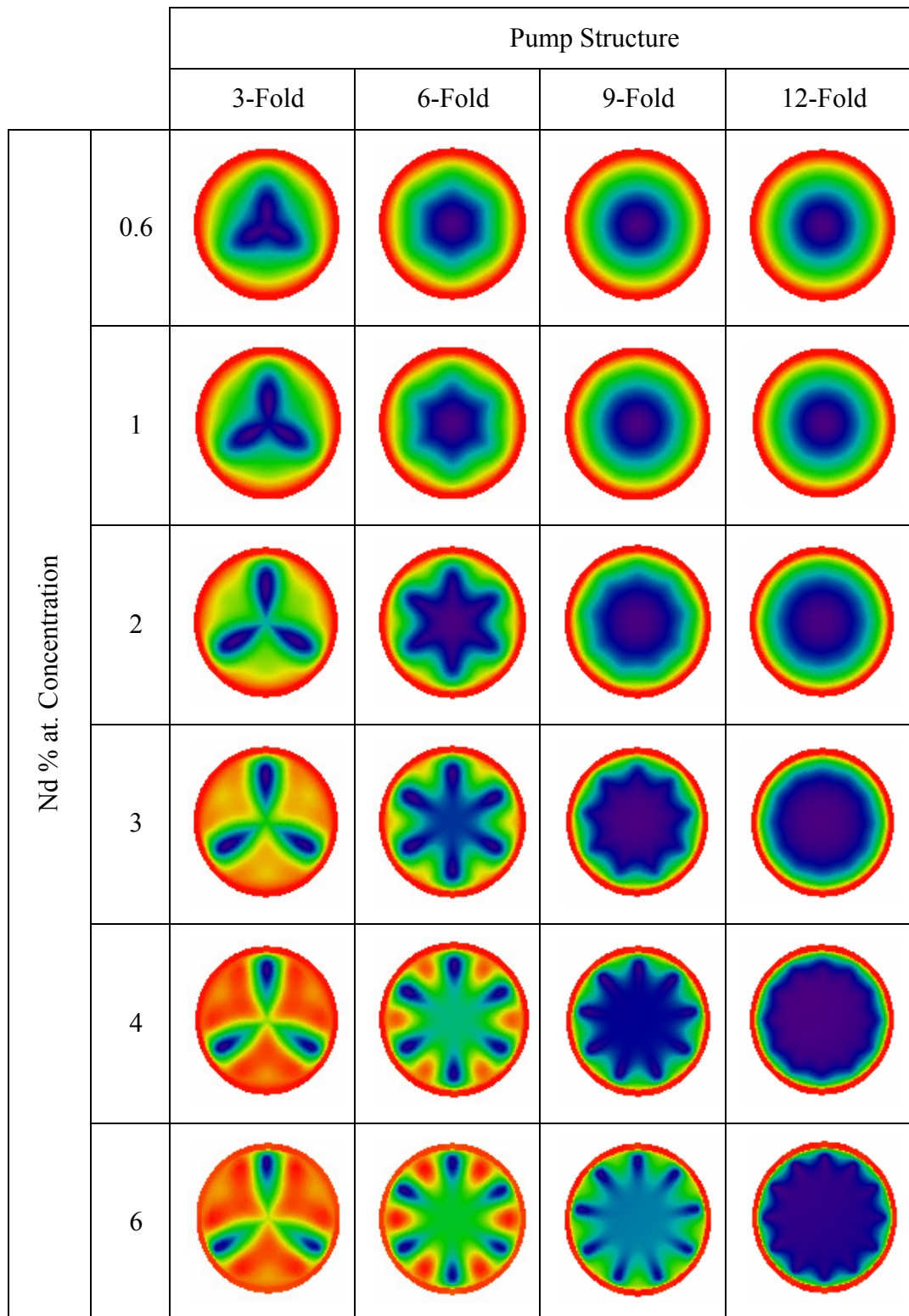


Table A5.3- Radial stress distribution of 3 mm rod pumped with 885 nm source

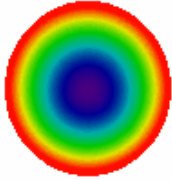
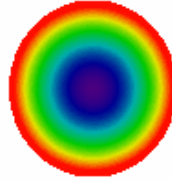
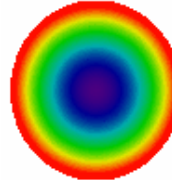
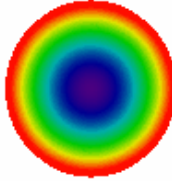
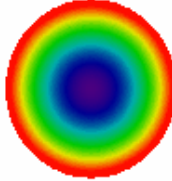
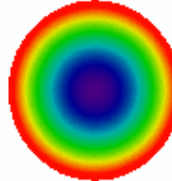
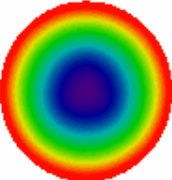
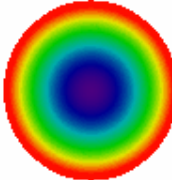
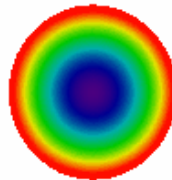
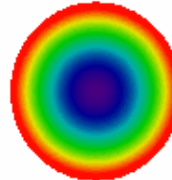
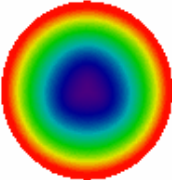
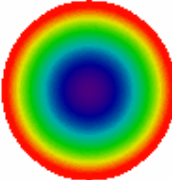
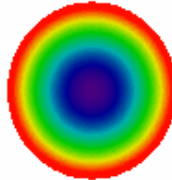
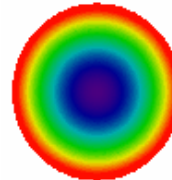
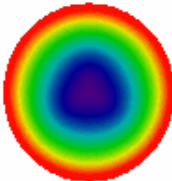
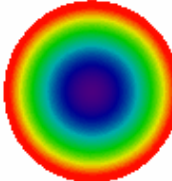
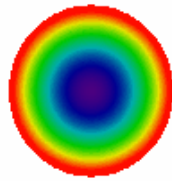
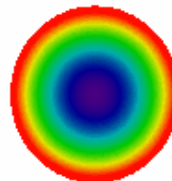
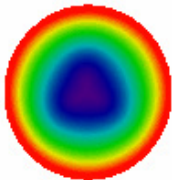
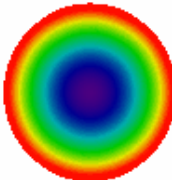
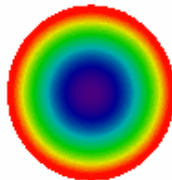
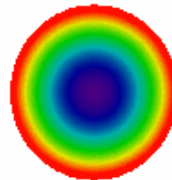
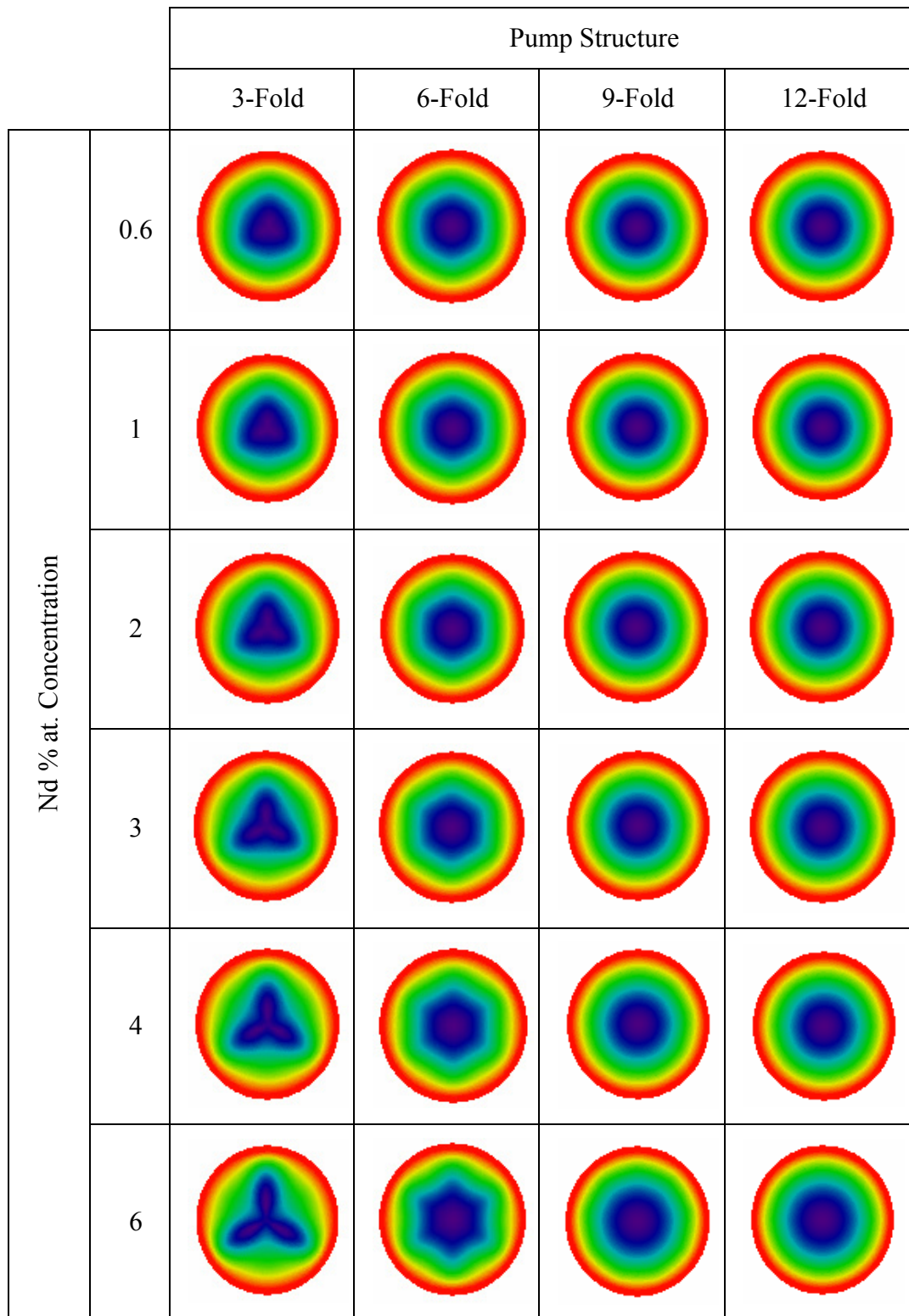
		Pump Structure			
		3-Fold	6-Fold	9-Fold	12-Fold
Nd % at. Concentration	0.6				
	1				
	2				
	3				
	4				
	6				

Table A5.4- Radial stress distribution of 6 mm rod pumped with 885 nm source



APPENDIX VI

AZIMUTHAL STRESS RESULTS

Table A6. 1-Azimuthal stress distribution of 3 mm rod pumped with 808 nm source

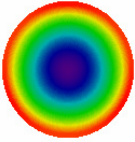
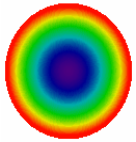
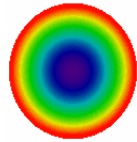
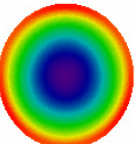
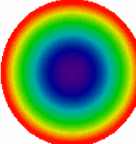
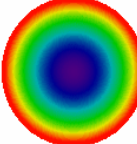
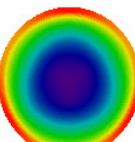
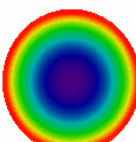
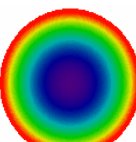
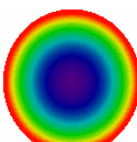
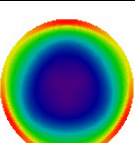
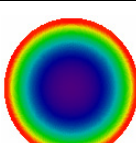
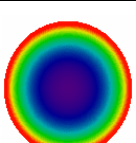
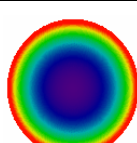
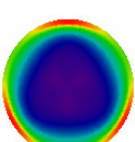
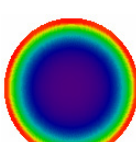
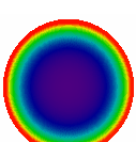
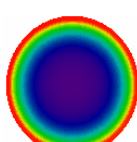
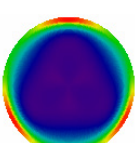
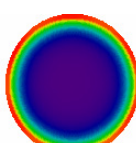
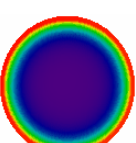
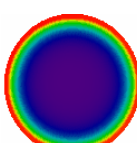
		Pump Structure			
		3-Fold	6-Fold	9-Fold	12-Fold
Nd % at. Concentration	0.6				
	1				
	2				
	3				
	4				
	6				

Table A6. 2- Azimuthal stress distribution of 6 mm rod pumped with 808 nm source

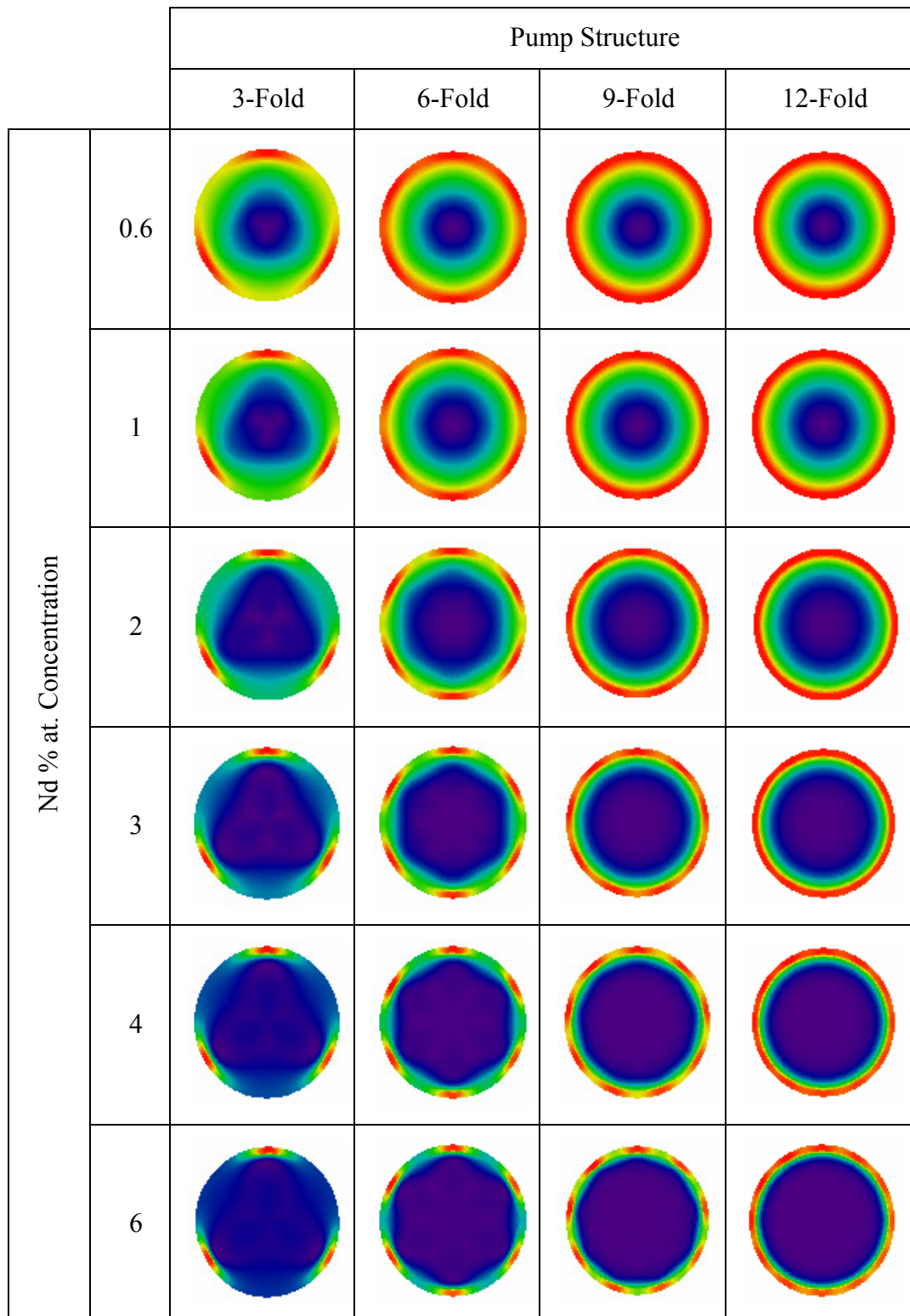


Table A6. 3- Azimuthal stress distribution of 3 mm rod pumped with 885 nm source

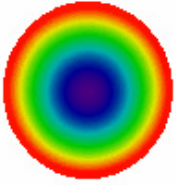
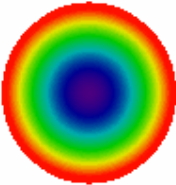
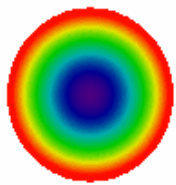
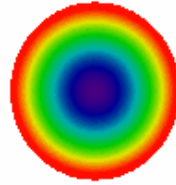
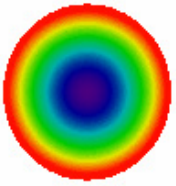
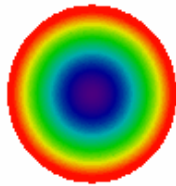
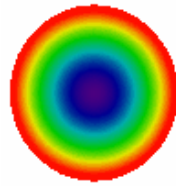
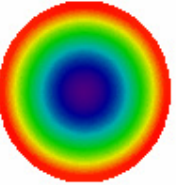
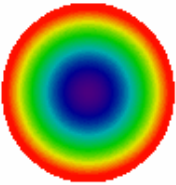
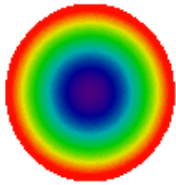
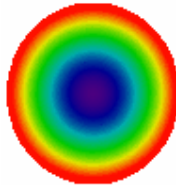
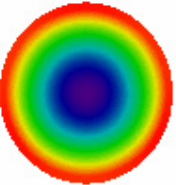
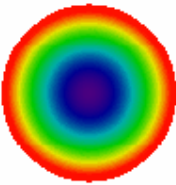
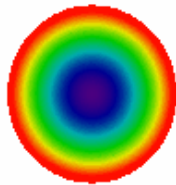
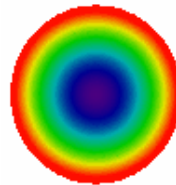
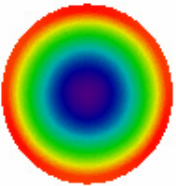
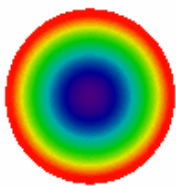
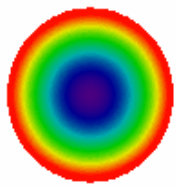
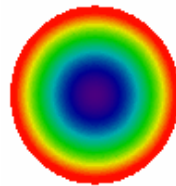
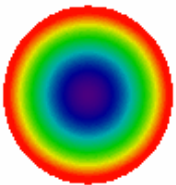
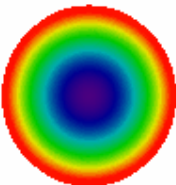
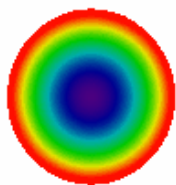
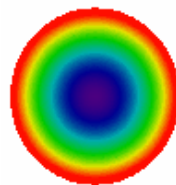
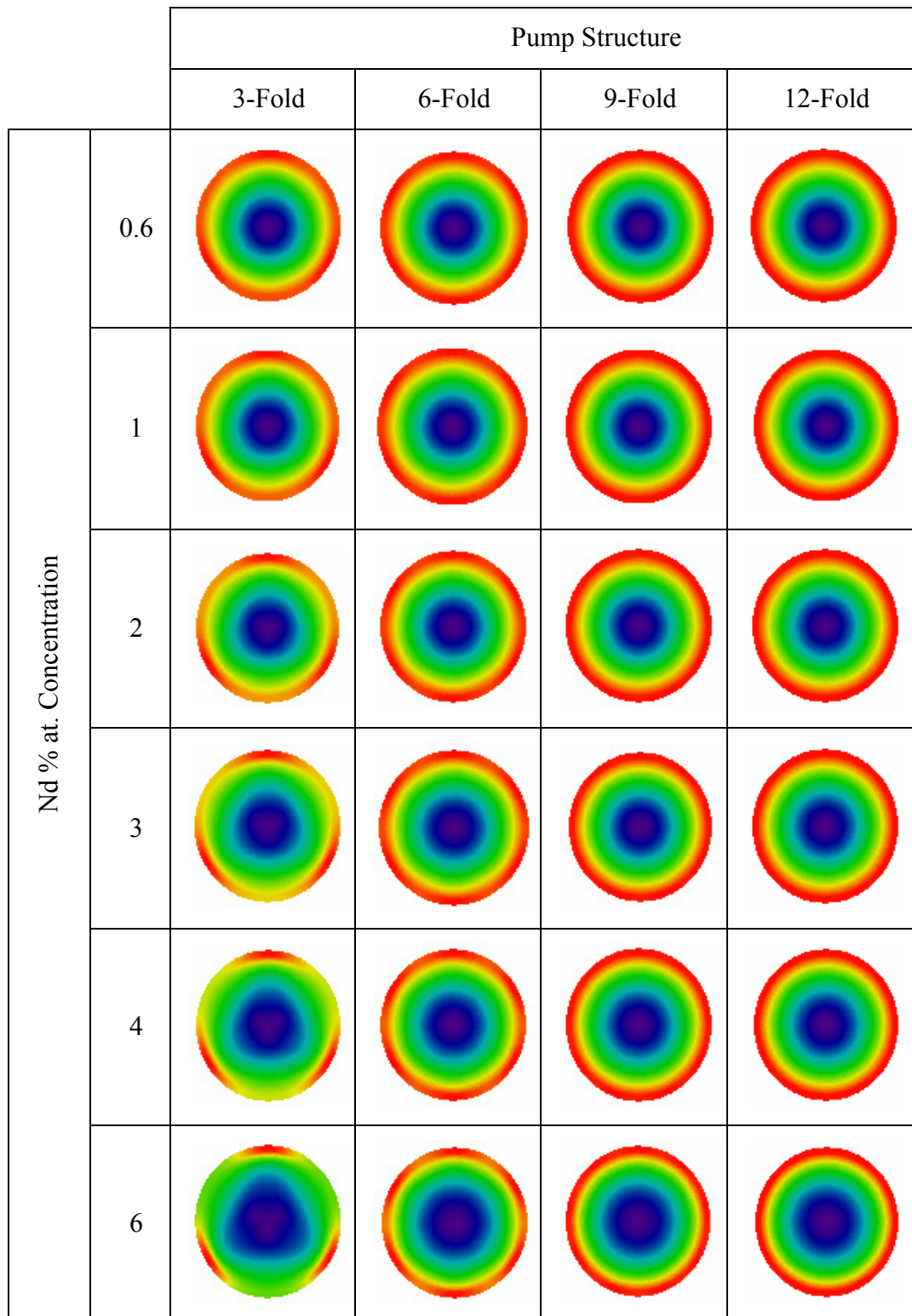
		Pump Structure			
		3-Fold	6-Fold	9-Fold	12-Fold
Nd % at. Concentration	0.6				
	1				
	2				
	3				
	4				
	6				

Table A6. 4- Azimuthal stress distribution of 6 mm rod pumped with 885 nm source



APPENDIX VII

AXIAL STRESS RESULTS

Table A7.1– Axial stress distribution of 3 mm rod pumped with 808 nm source

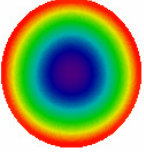
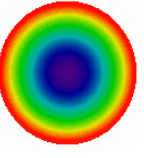
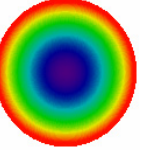
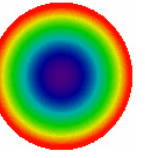
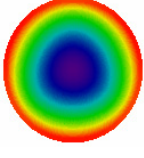
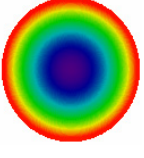
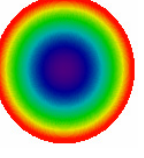
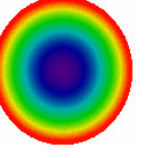
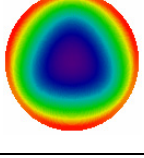
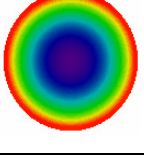
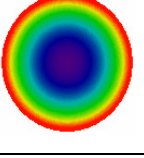
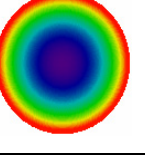
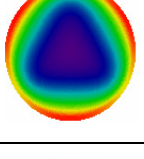
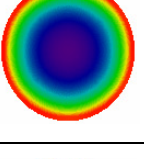
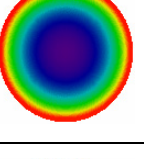
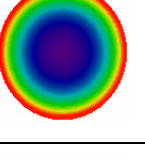
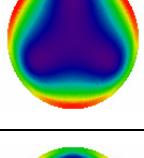
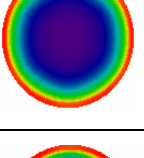
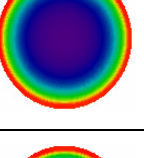
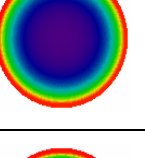
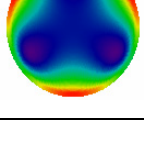
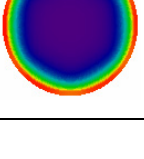
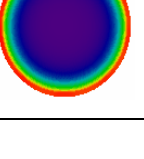
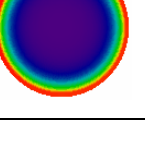
		Pump Structure			
		3-Fold	6-Fold	9-Fold	12-Fold
Nd % at. Concentration	0.6				
	1				
	2				
	3				
	4				
	6				

Table A7.2- Axial stress distribution of 6 mm rod pumped with 808 nm source

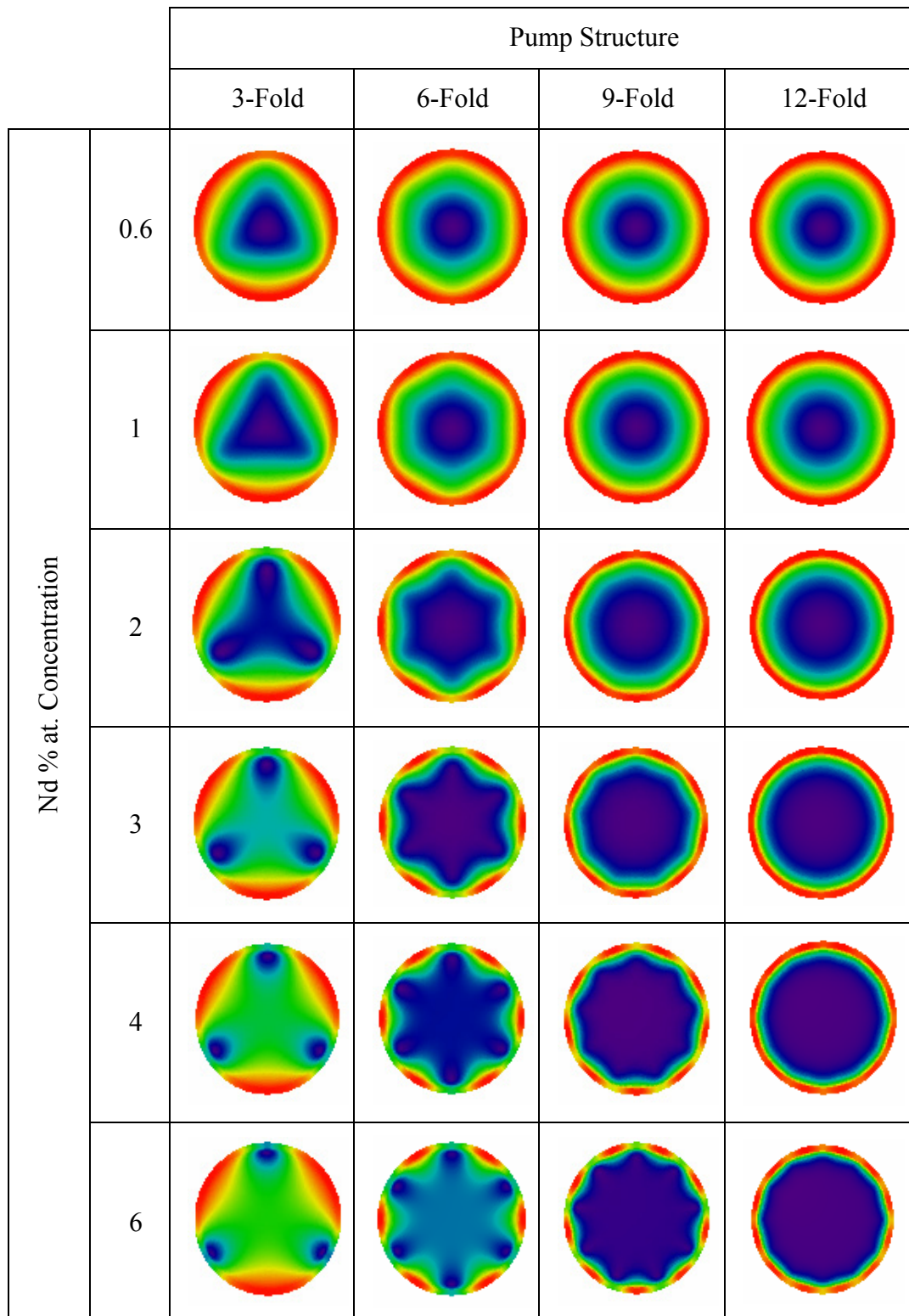


Table A7.3- Axial stress distribution of 3 mm rod pumped with 885 nm source

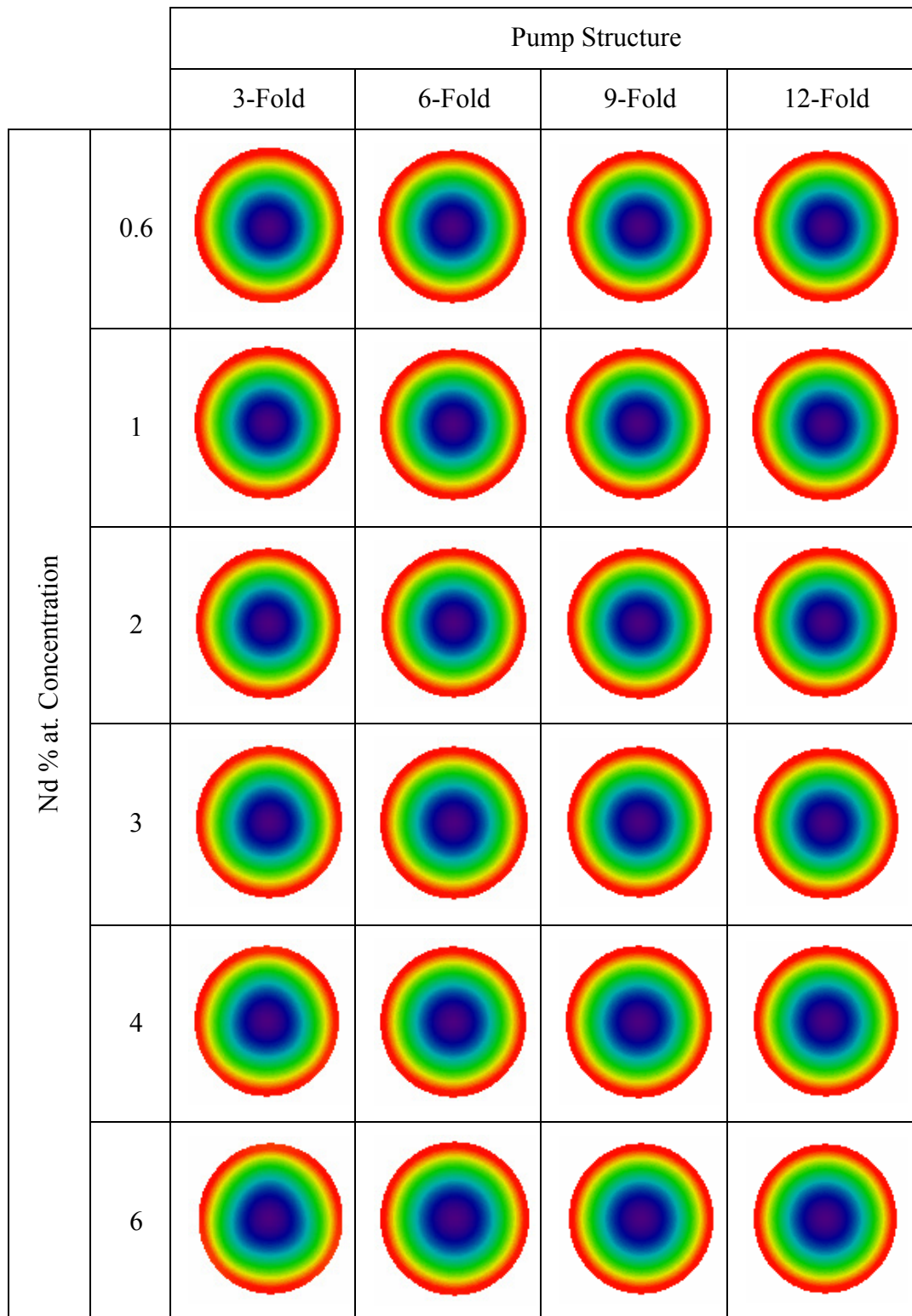
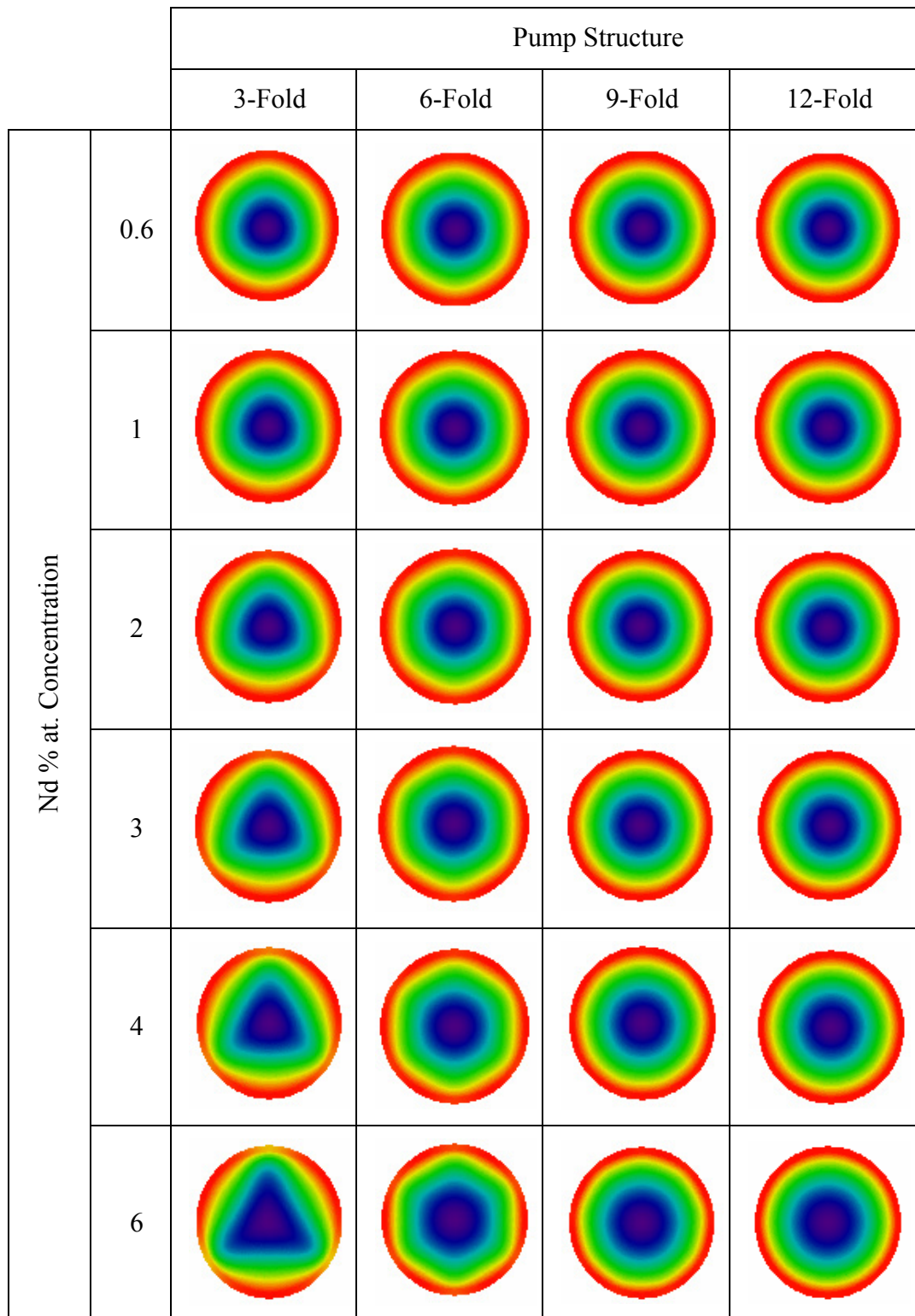


Table A7.4- Axial stress distribution of 6 mm rod pumped with 885 nm source



APPENDIX VIII

SHEAR STRESS RESULTS

Table A8. 1– Shear stress distribution of 3 mm rod pumped with 808 nm source

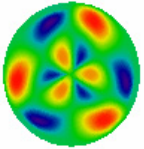
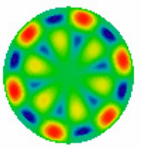
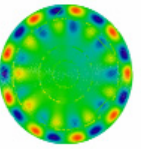
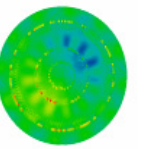
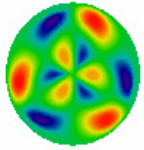
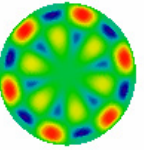
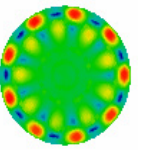
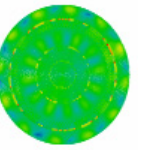
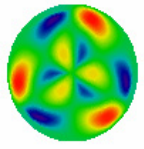
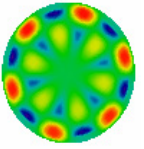
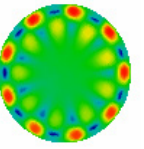
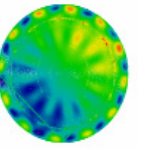
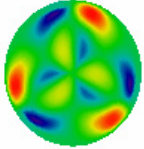
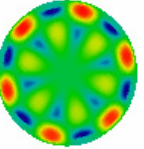
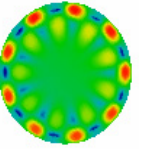
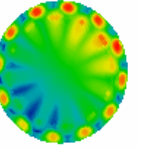
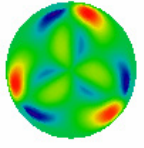
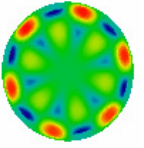
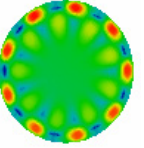
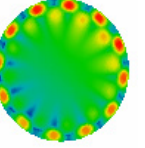
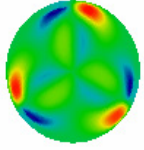
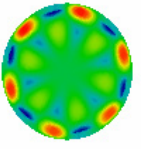
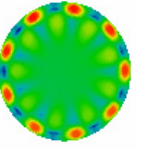
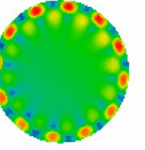
		Pump Structure			
		3-Fold	6-Fold	9-Fold	12-Fold
Nd % at. Concentration	0.6				
	1				
	2				
	3				
	4				
	6				

Table A8. 2– Shear stress distribution of 6 mm rod pumped with 808 nm source

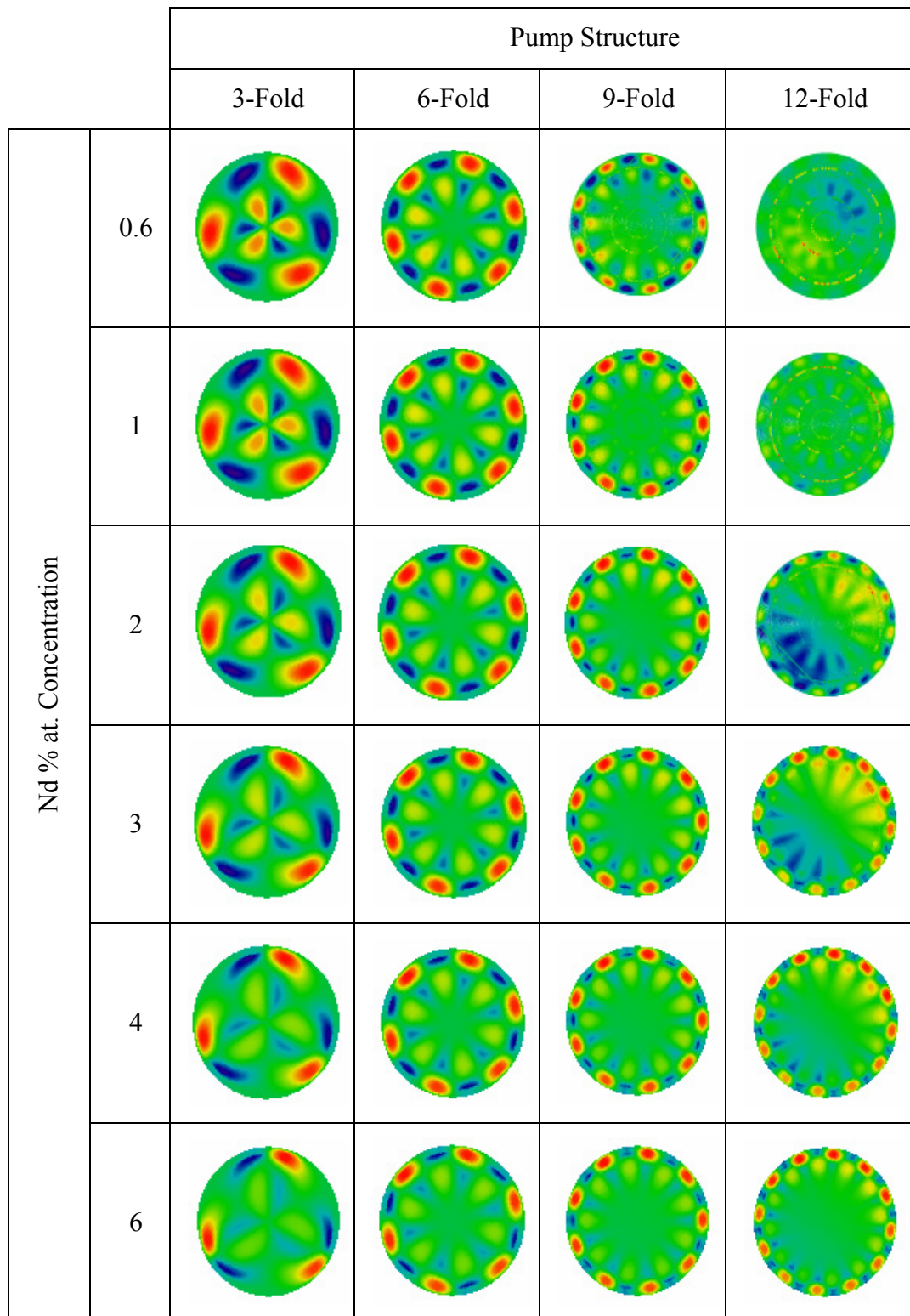


Table A8.3- Shear stress distribution of 3 mm rod pumped with 885 nm source

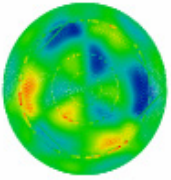
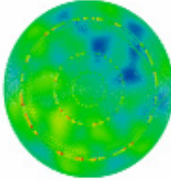
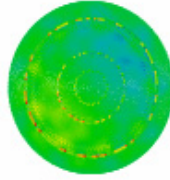
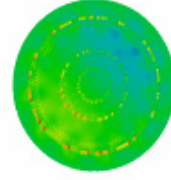
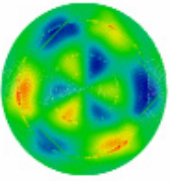
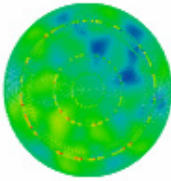
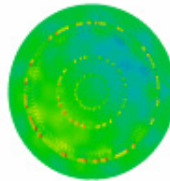
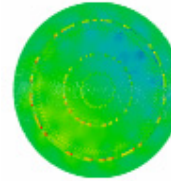
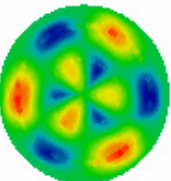
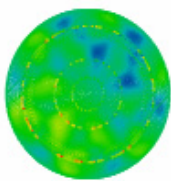
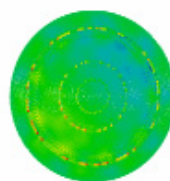
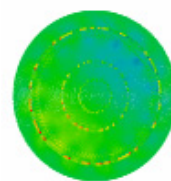
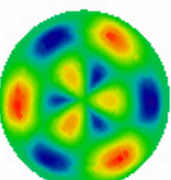
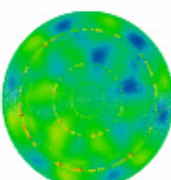
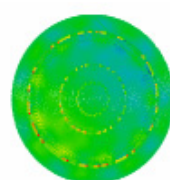
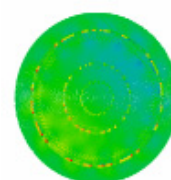
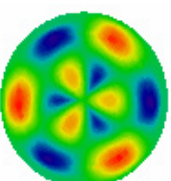
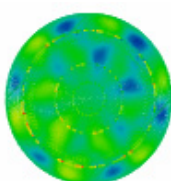
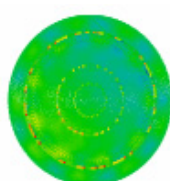
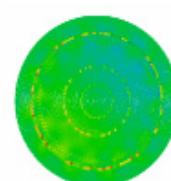
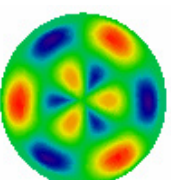
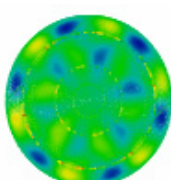
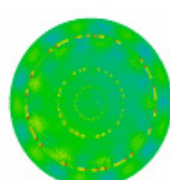
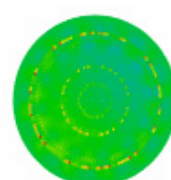
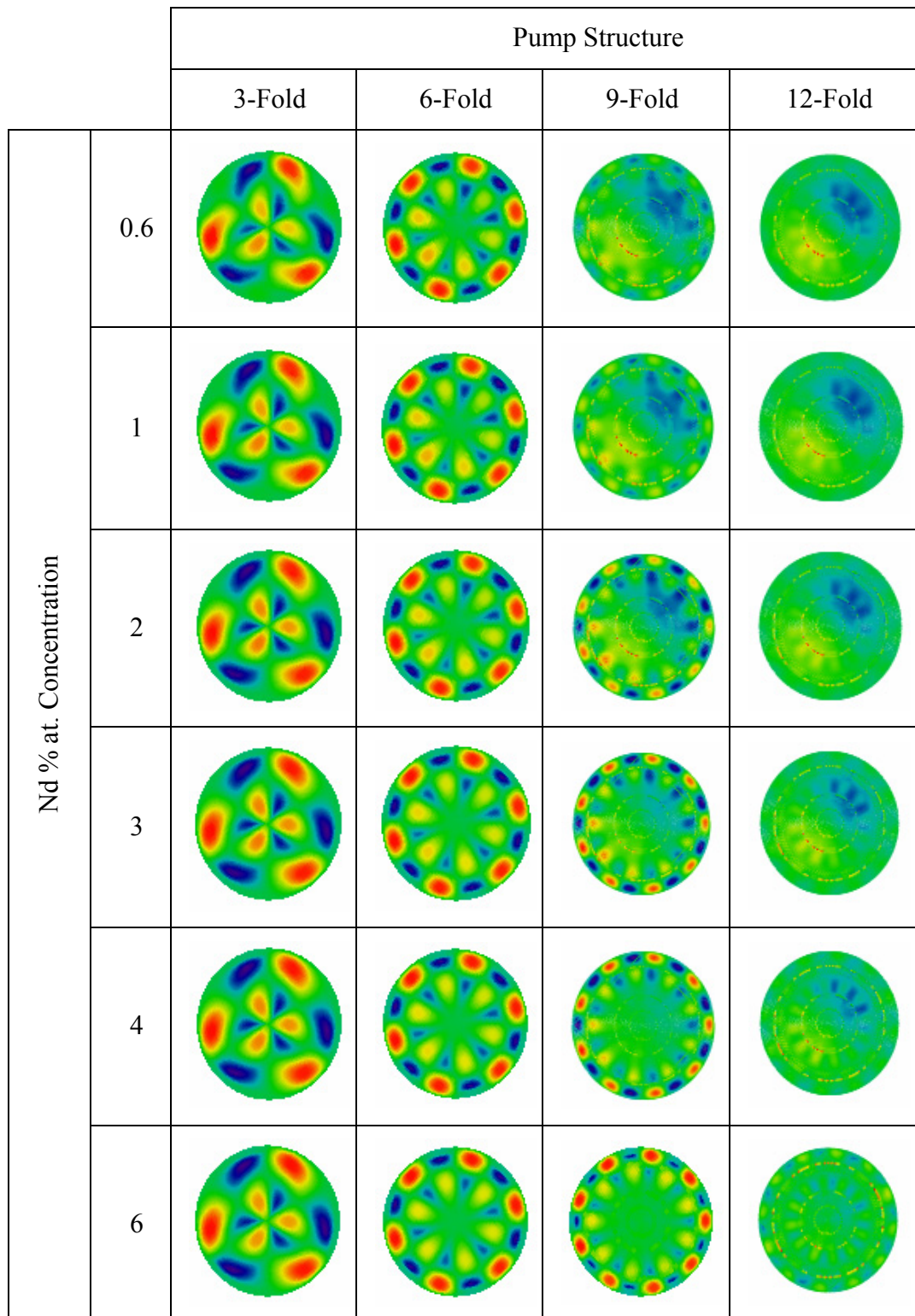
		Pump Structure			
		3-Fold	6-Fold	9-Fold	12-Fold
Nd % at. Concentration	0.6				
	1				
	2				
	3				
	4				
	6				

Table A8. 4- Shear stress distribution of 6 mm rod pumped with 885 nm source



APPENDIX IX

VON MISES STRESS RESULTS

Table A9. 1 – Von Mises stress distribution of 3 mm rod pumped with 808 nm source

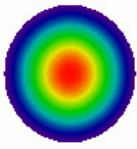
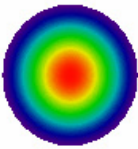
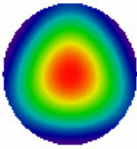
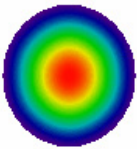
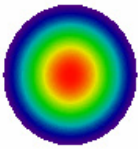
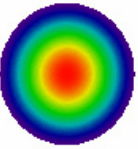
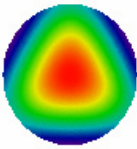
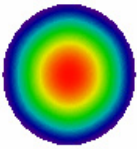
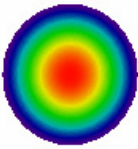
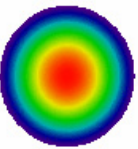
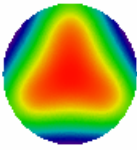
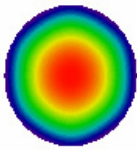
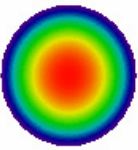
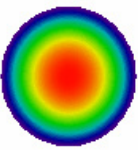
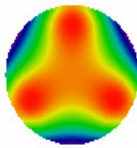
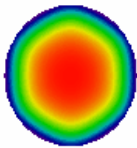
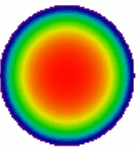
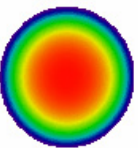
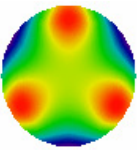
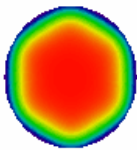
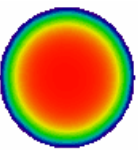
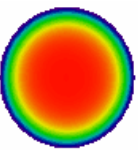
		Pump Structure			
		3-Fold	6-Fold	9-Fold	12-Fold
Nd % at. Concentration	0.6				
	1				
	2				
	3				
	4				
	6				

Table A9. 2 – Von Mises stress distribution of 6 mm rod pumped with 808 nm source

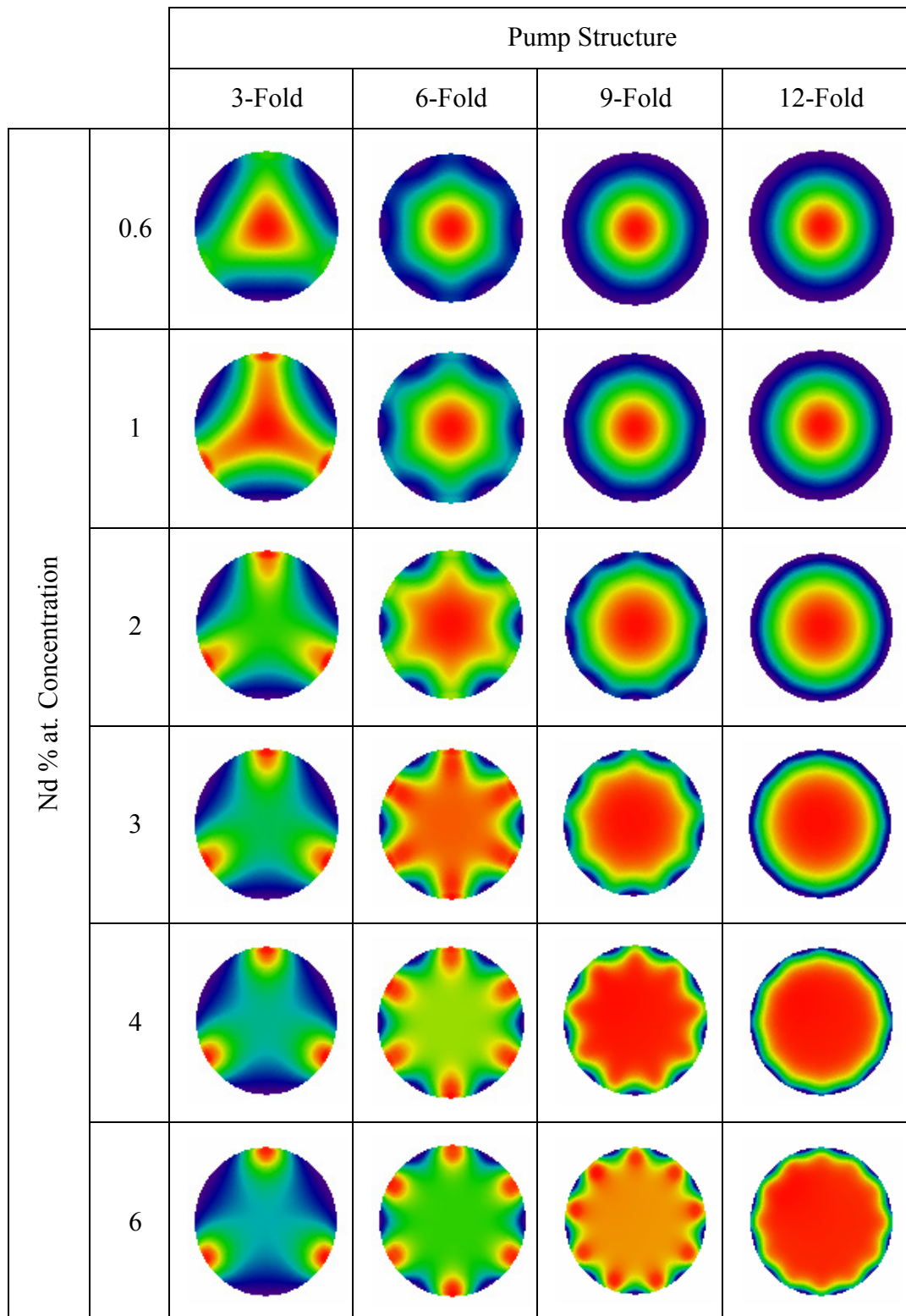


Table A9. 3– Von Mises stress distribution of 3 mm rod pumped with 885 nm source

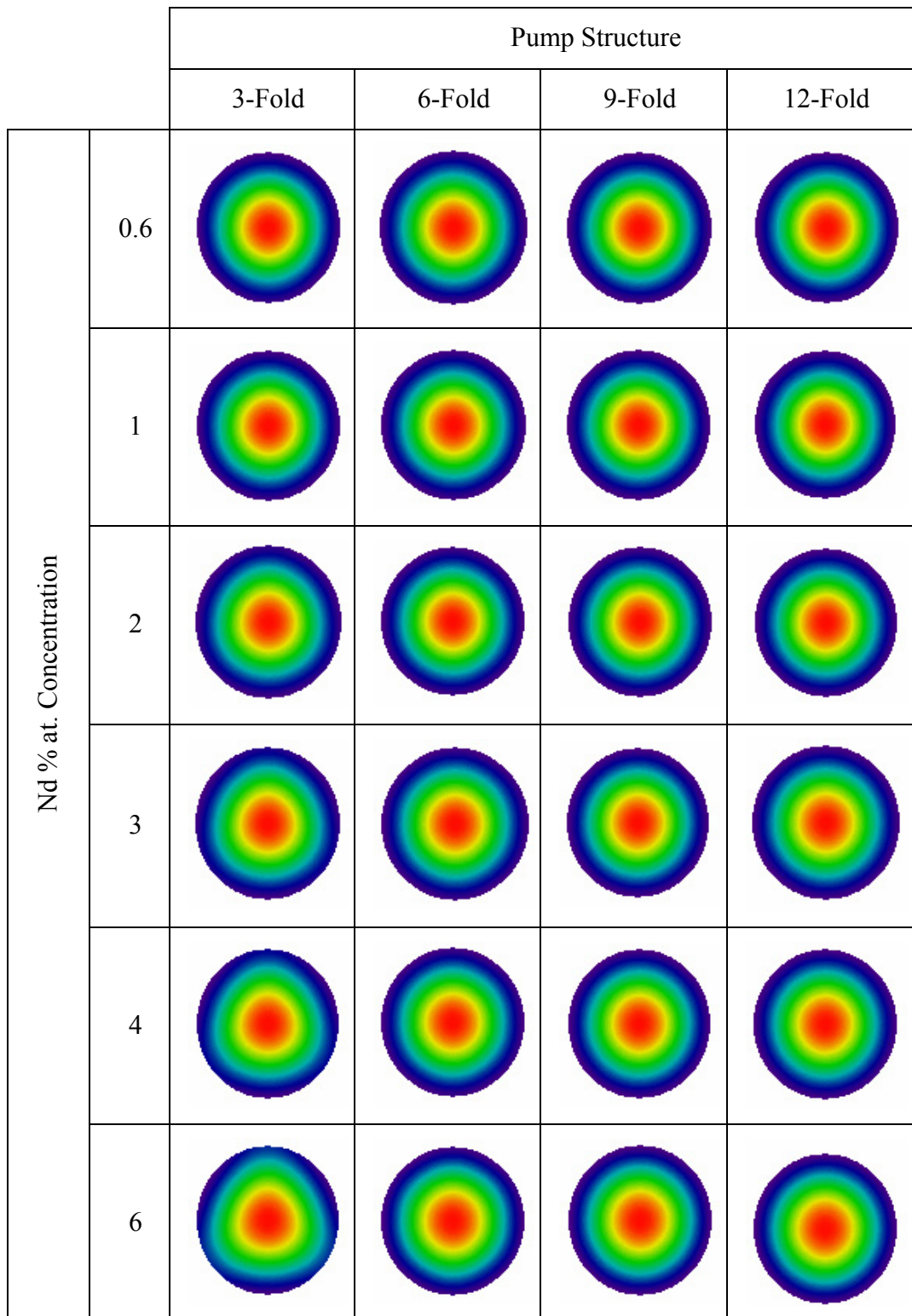
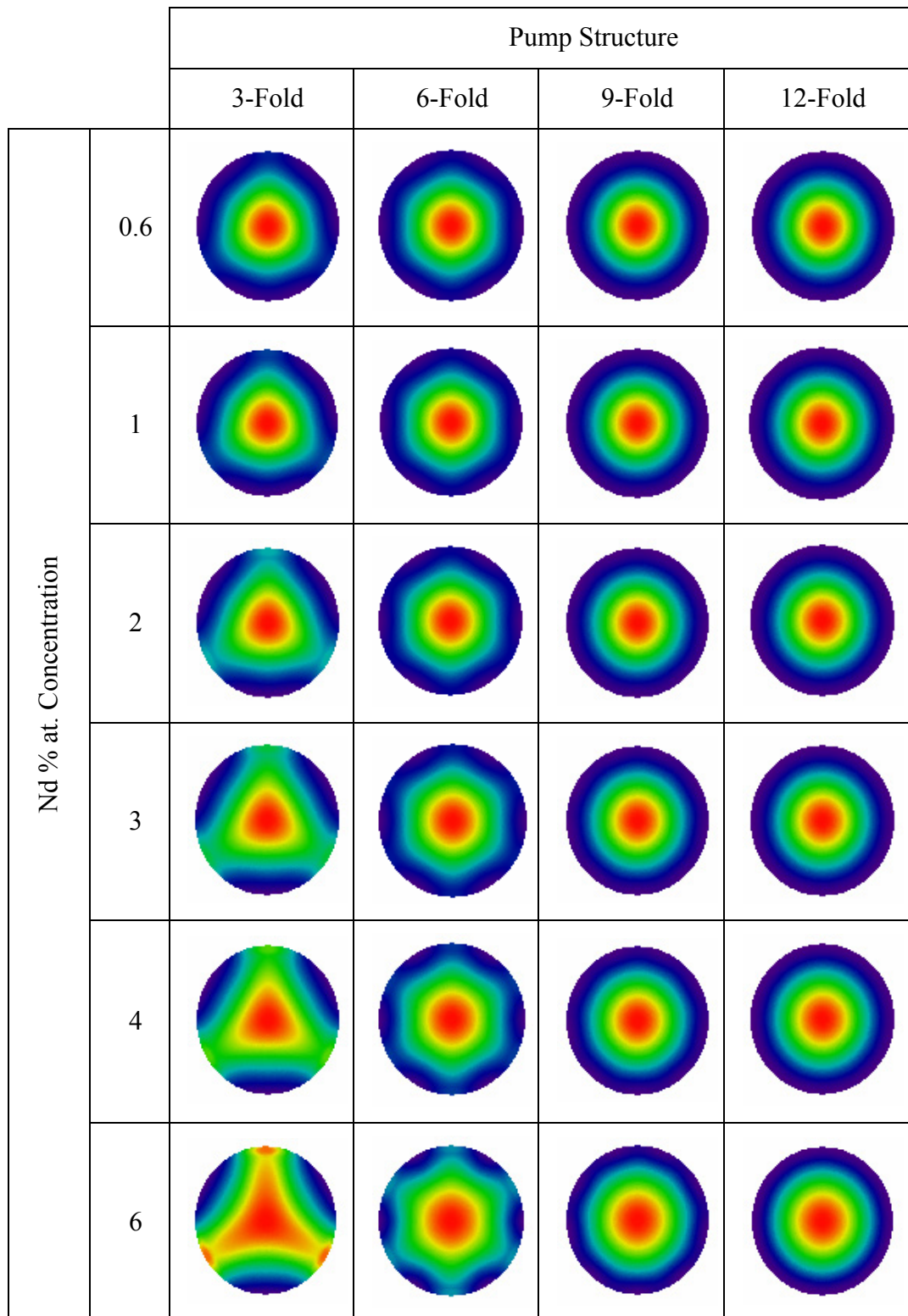


Table A9.4- Von Mises stress distribution of 6 mm rod pumped with 885 nm source



APPENDIX X

INDEX VARIATION DUE TO TEMPERATURE

Table A10. 1 - Thermal index change distribution of 3 mm rod pumped with 808 nm source

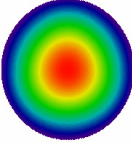
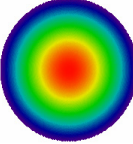
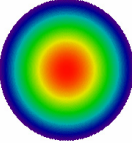
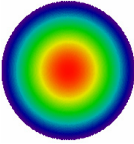
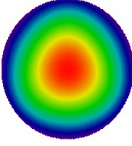
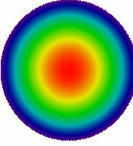
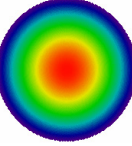
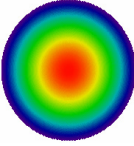
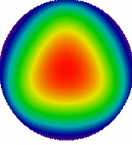
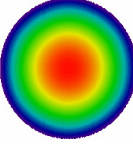
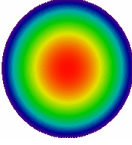
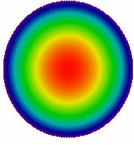
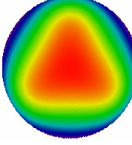
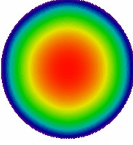
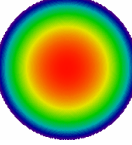
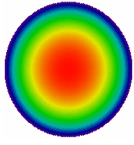
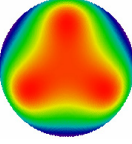
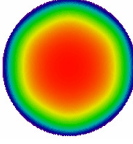
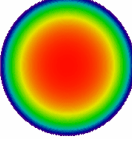
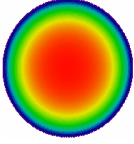
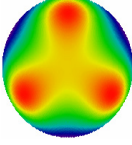
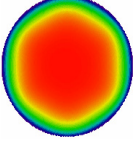
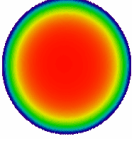
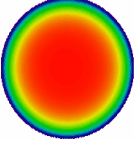
		Pump Structure			
		3-Fold	6-Fold	9-Fold	12-Fold
Nd % at. Concentration	0.6				
	1				
	2				
	3				
	4				
	6				

Table A10. 2 - Thermal index change distribution of 6 mm rod pumped with 808 nm source

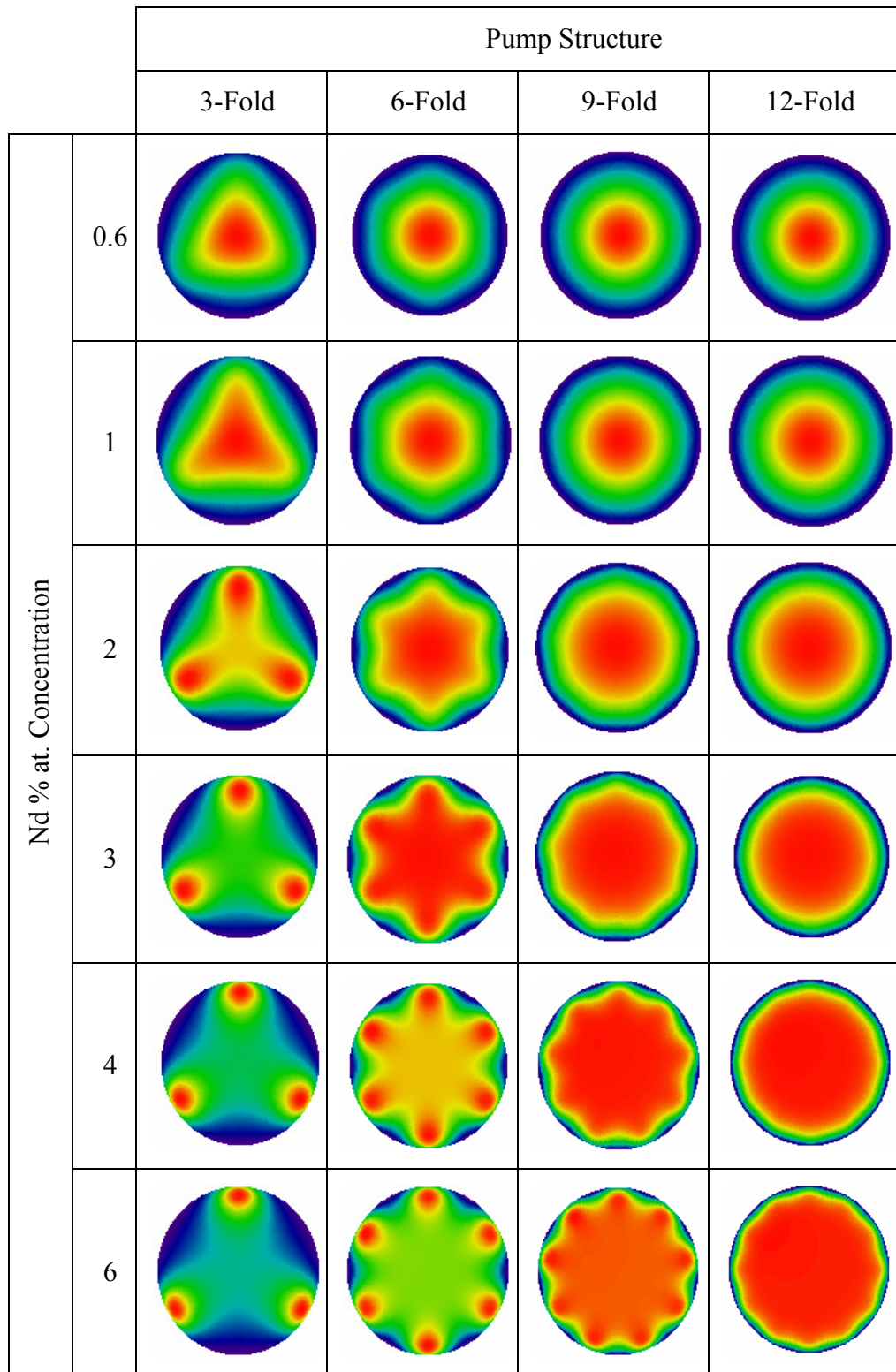


Table A10. 3- Thermal index change distribution of 3 mm rod pumped with 885 nm source

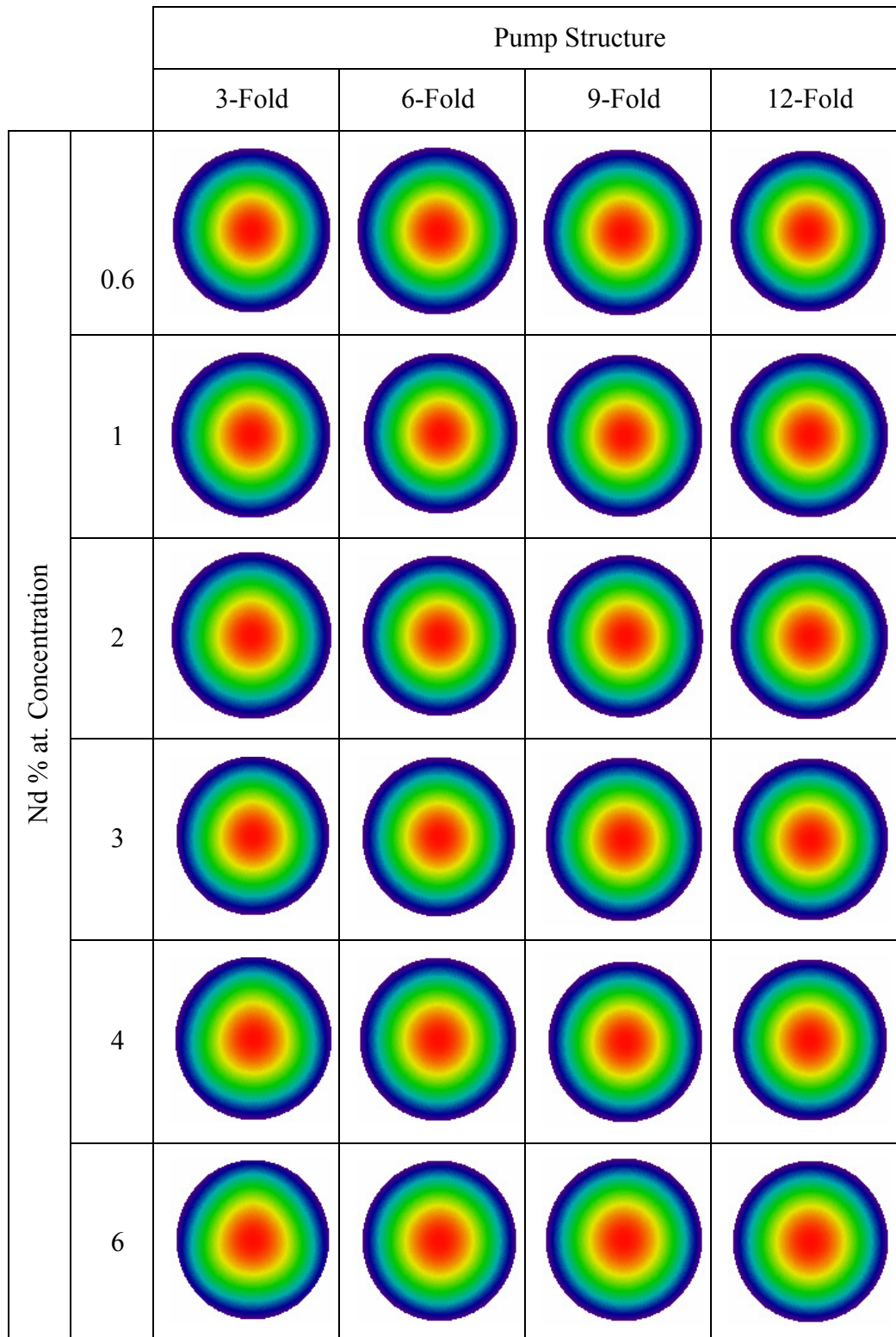
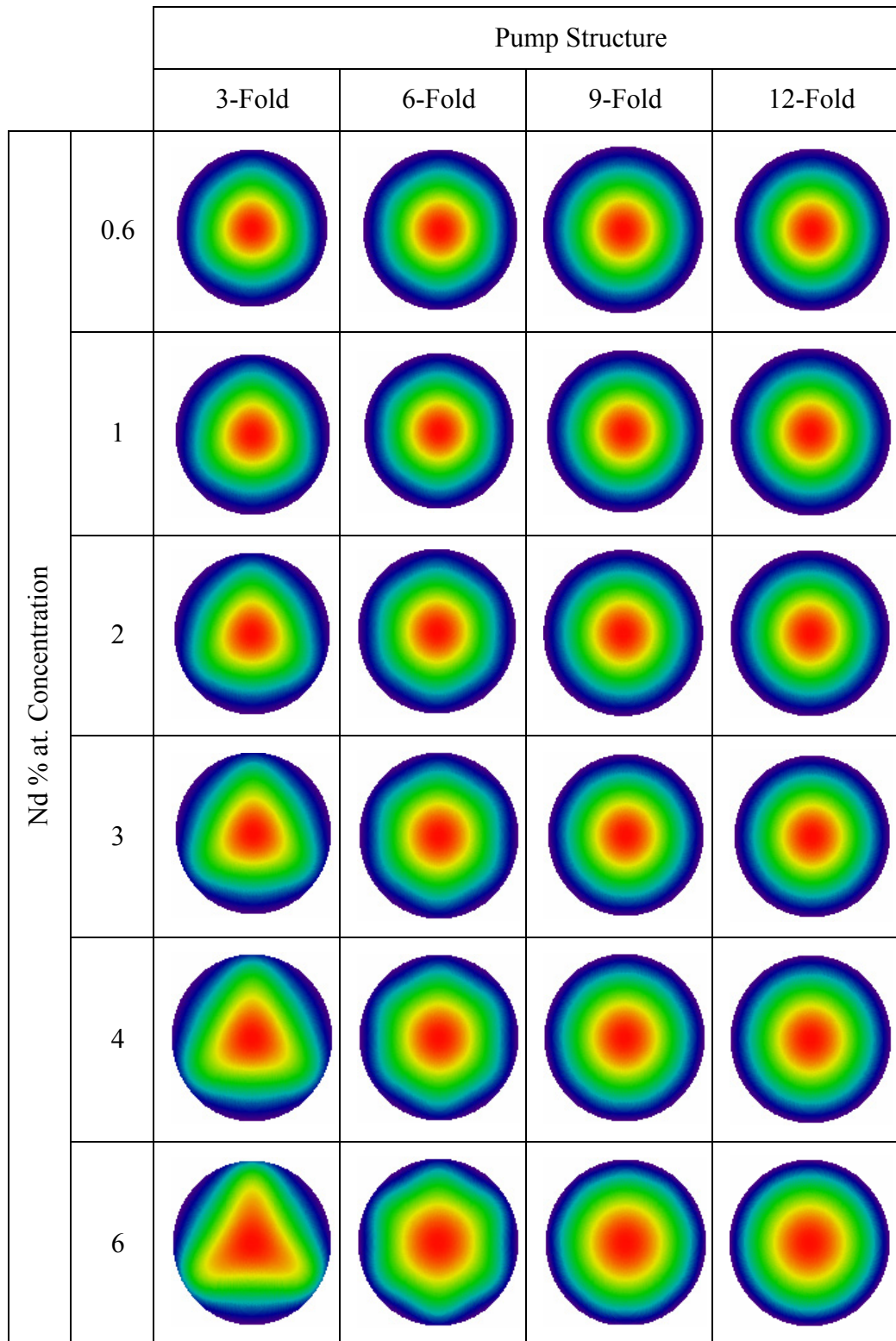


Table A10. 4- Thermal index change distribution of 6 mm rod pumped with 885 nm source



APPENDIX XI

INDEX VARIATION FOR RADIALLY POLARIZED LIGHT

Table A11. 1- Stress induced index change distribution of 3 mm rod pumped with 808 nm source for radially polarized light

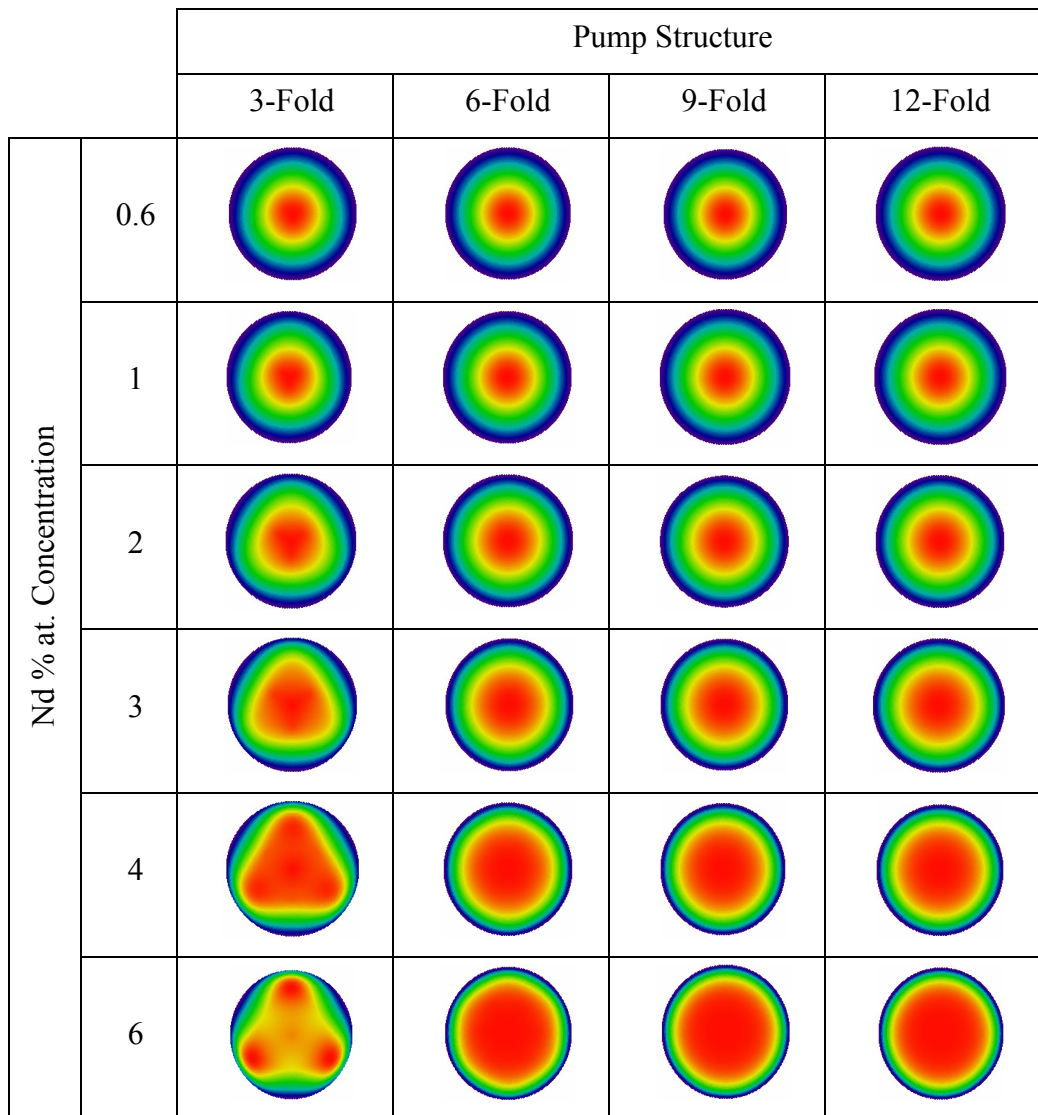


Table A11. 2- Stress induced index change distribution of 6 mm rod pumped with 808 nm source for radially polarized light

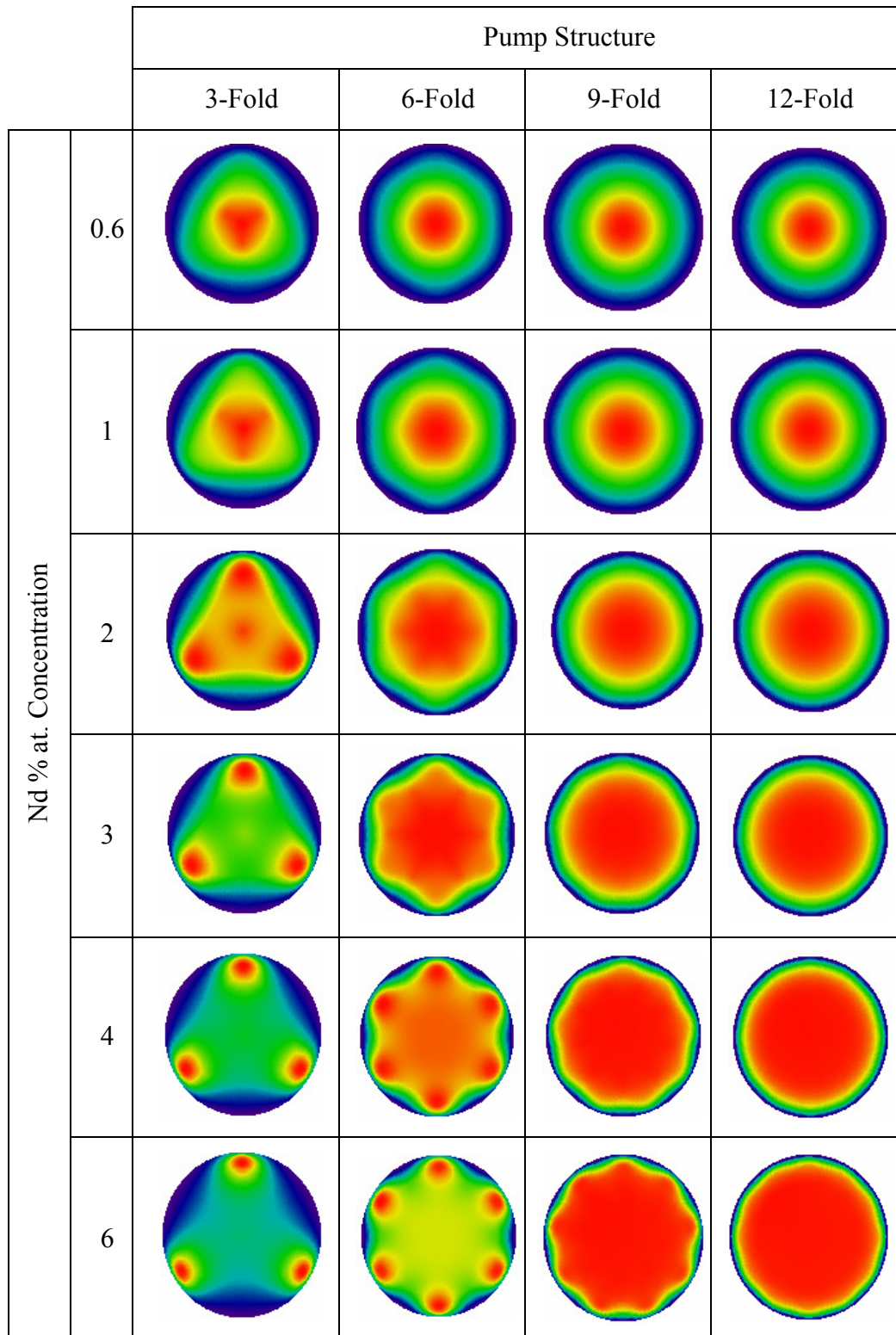


Table A11. 3- Stress induced index change distribution of 3 mm rod pumped with 885 nm source for radially polarized light

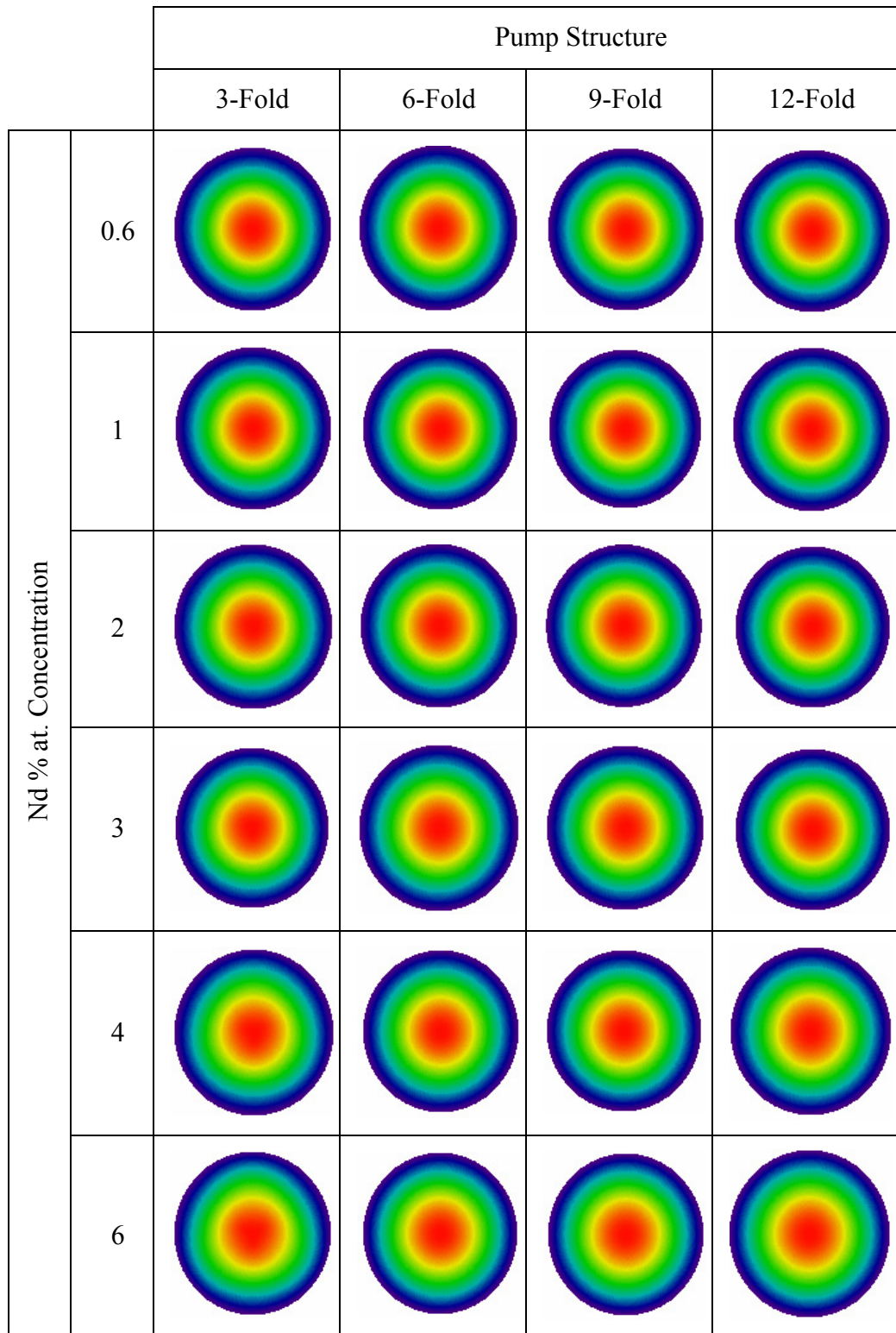
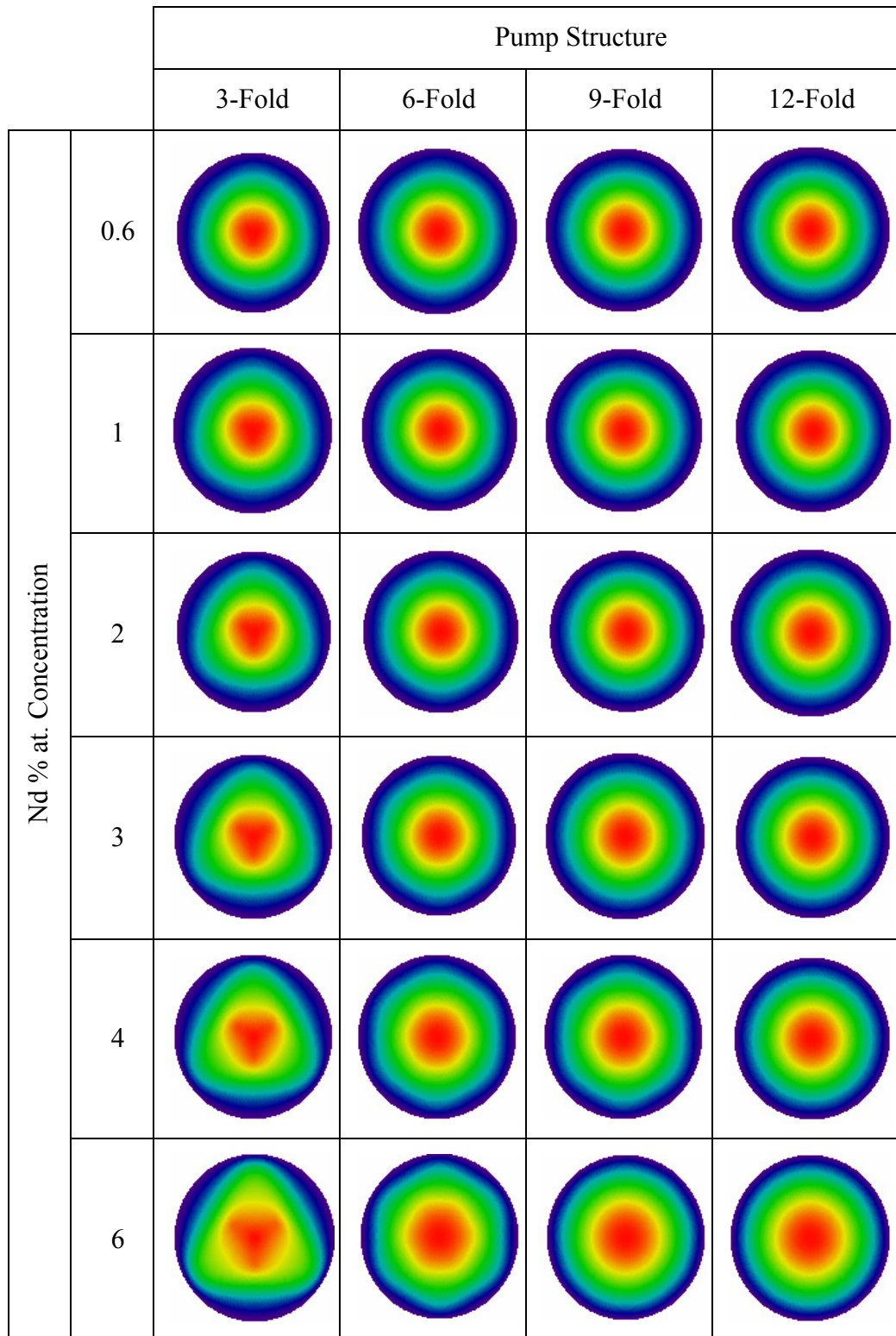


Table A11. 4- Stress induced index change distribution of 6 mm rod pumped with 885 nm source for radially polarized light



APPENDIX XII

INDEX VARIATION FOR AZIMUTHALLY POLARIZED LIGHT

Table A12. 1- Stress induced index change distribution of 3 mm rod pumped with 808 nm source for azimuthally polarized light

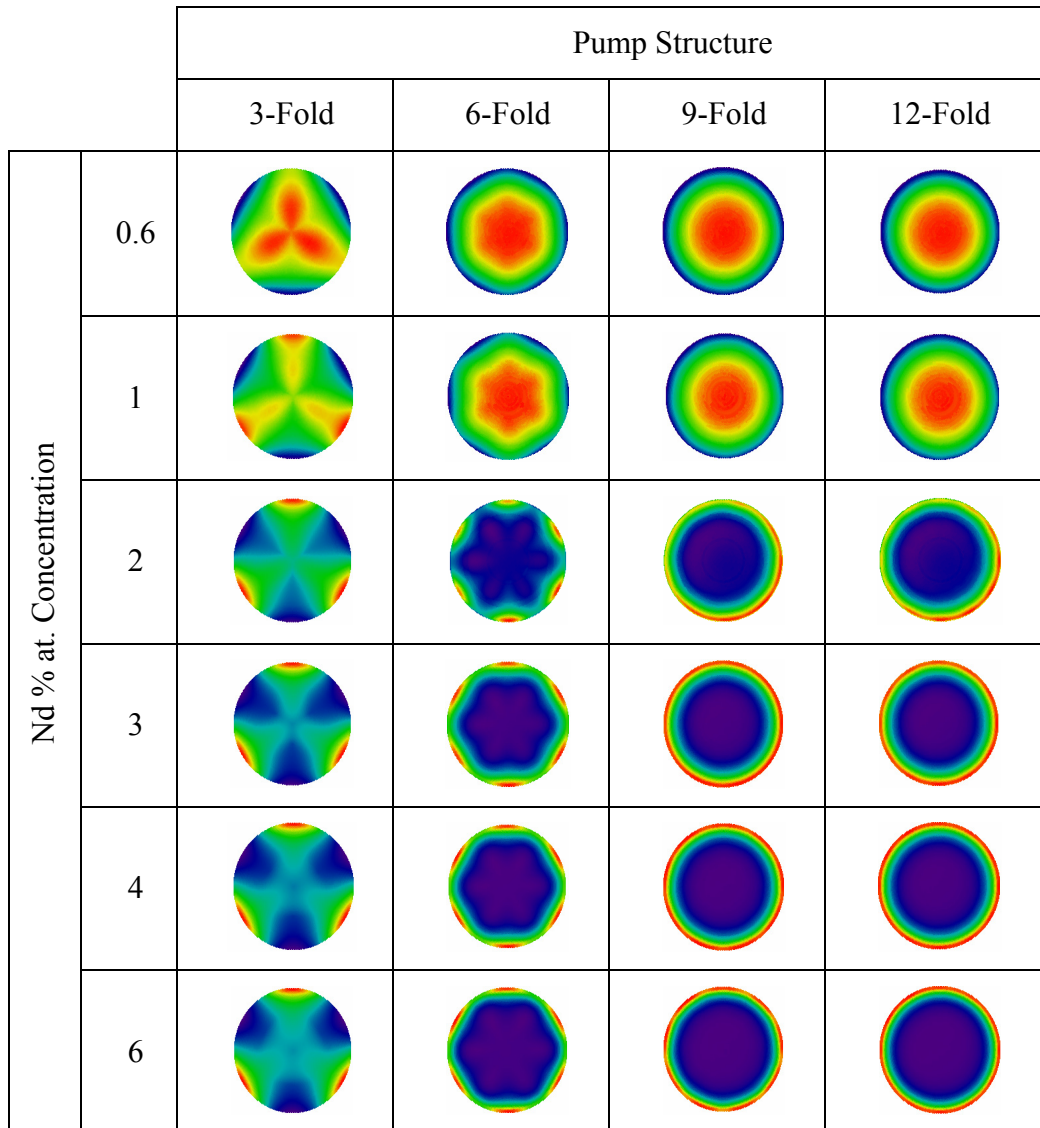


Table A12. 2- Stress induced index change distribution of 6 mm rod pumped with 808 nm source for azimuthally polarized light

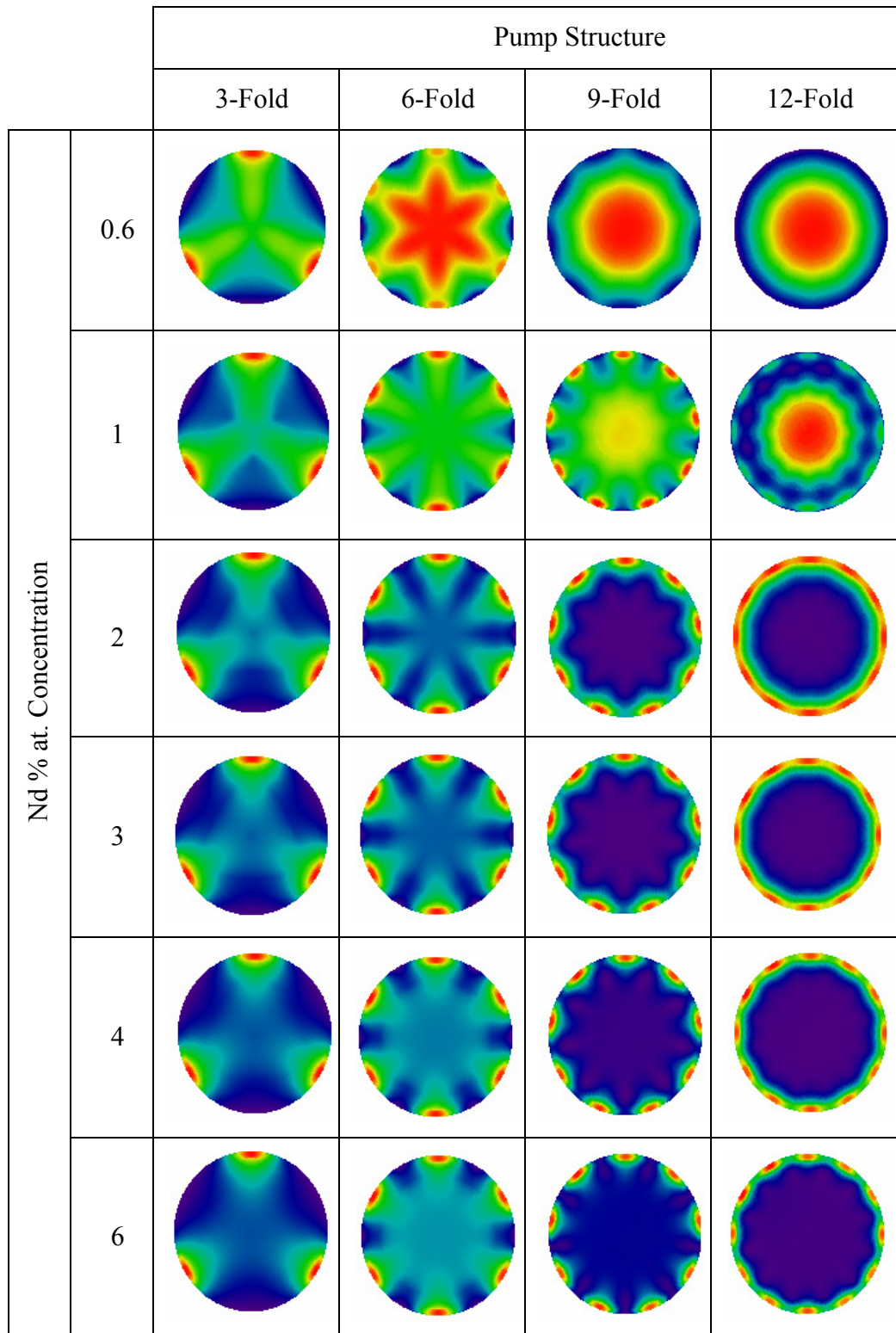


Table A12. 3 - Stress induced index change distribution of 3 mm rod pumped with 885 nm source for azimuthally polarized light

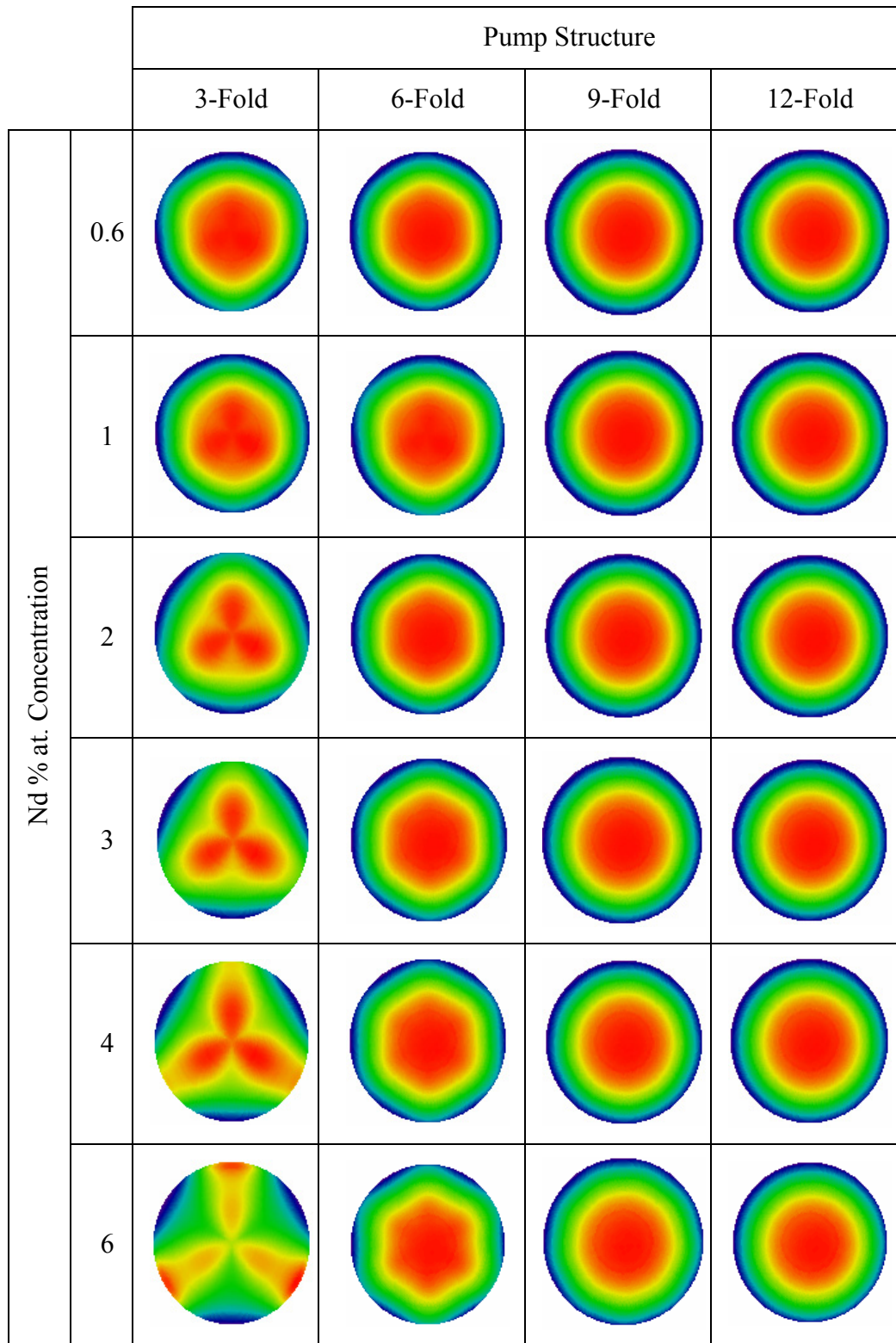
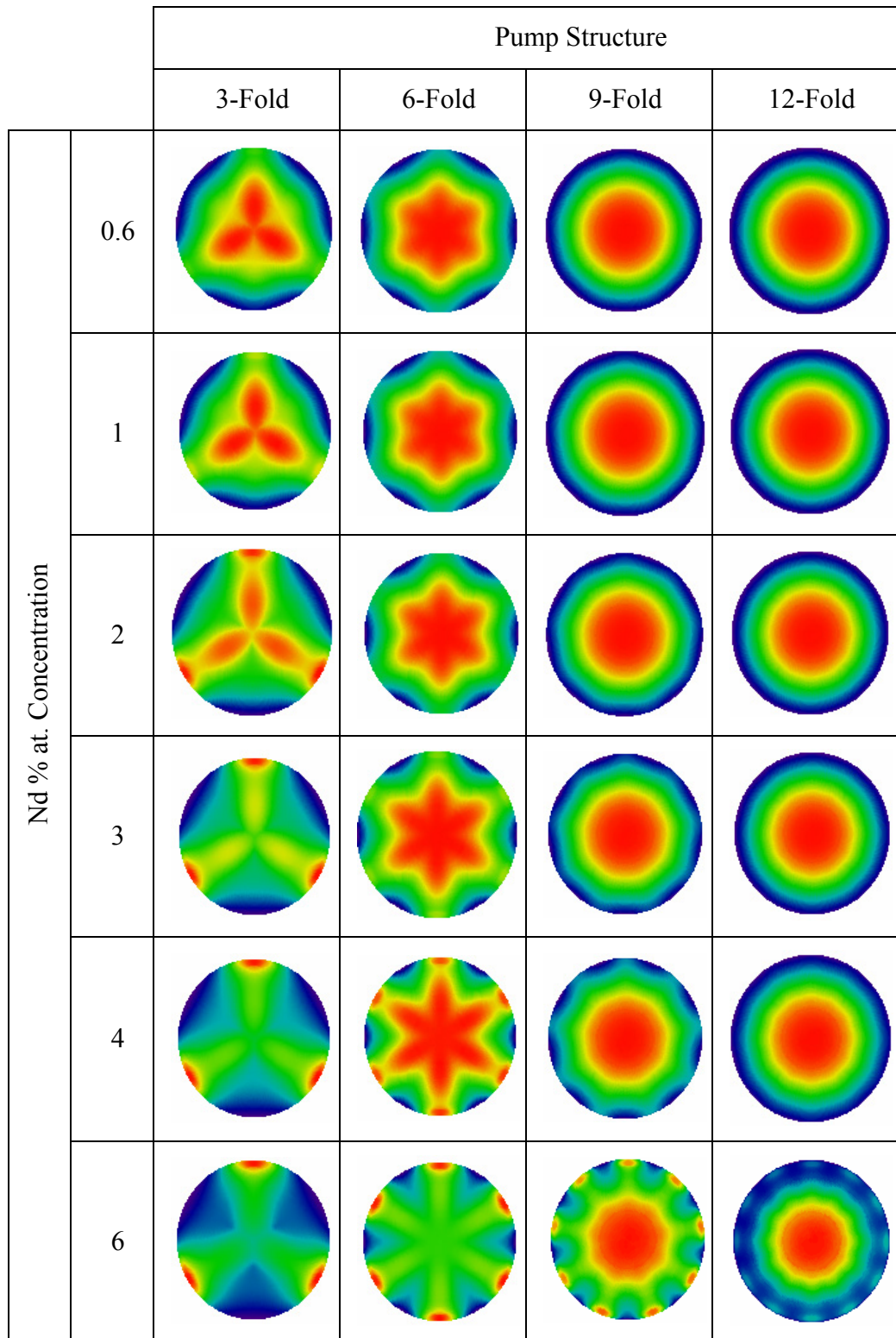


Table A12. 4- Stress induced index change distribution of 6 mm rod pumped with 885 nm source for azimuthally polarized light



APPENDIX XIII

DEPOLARIZATION

Table A13. 1- Depolarization distribution of 3 mm rod pumped with 808 nm source

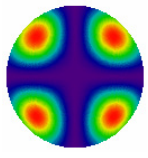
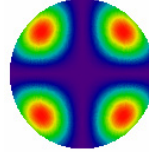
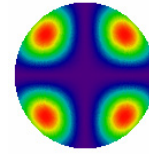
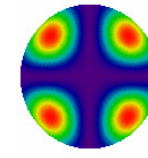
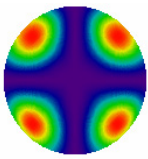
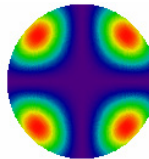
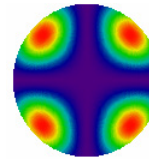
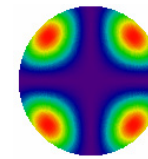
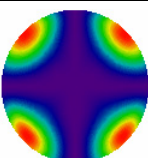
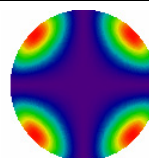
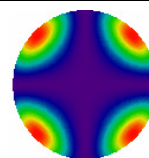
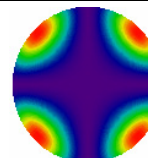
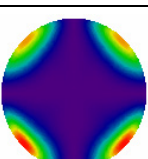
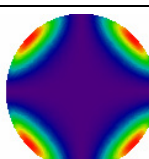
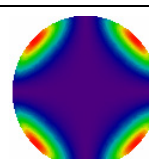
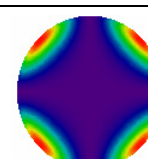
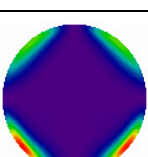
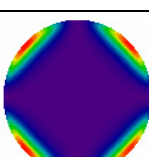
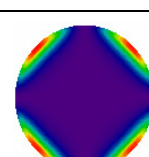
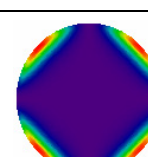
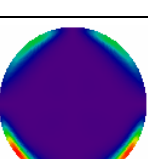
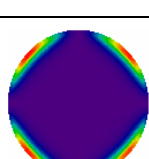
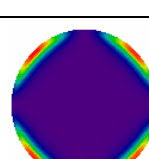
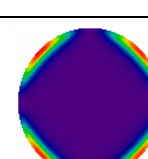
		Pump Structure			
		3-Fold	6-Fold	9-Fold	12-Fold
Nd % at. Concentration	0.6				
	1				
	2				
	3				
	4				
	6				

Table A13. 2- Depolarization distribution of 6 mm rod pumped with 808 nm source

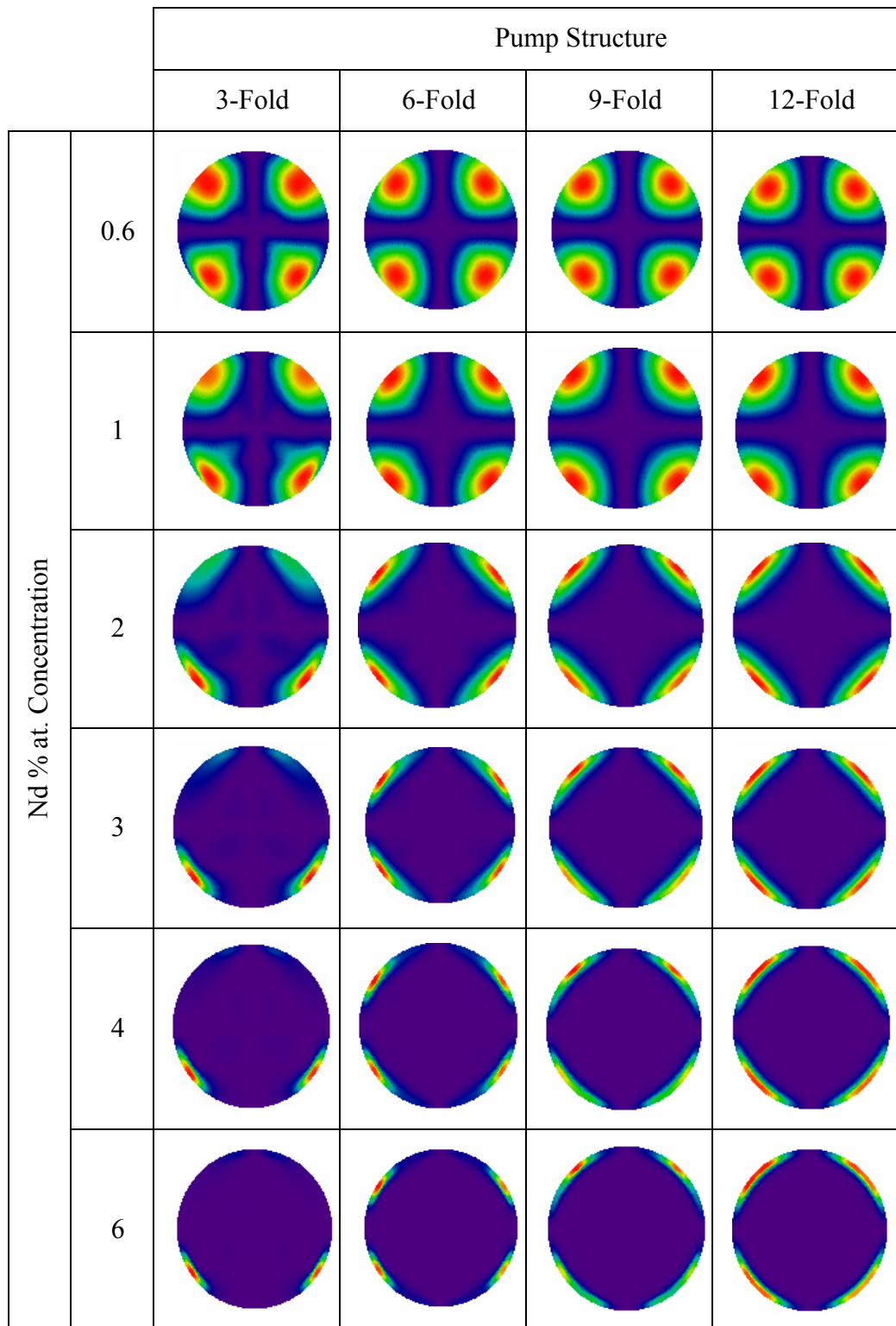


Table A13. 3- Depolarization distribution of 3 mm rod pumped with 885 nm source

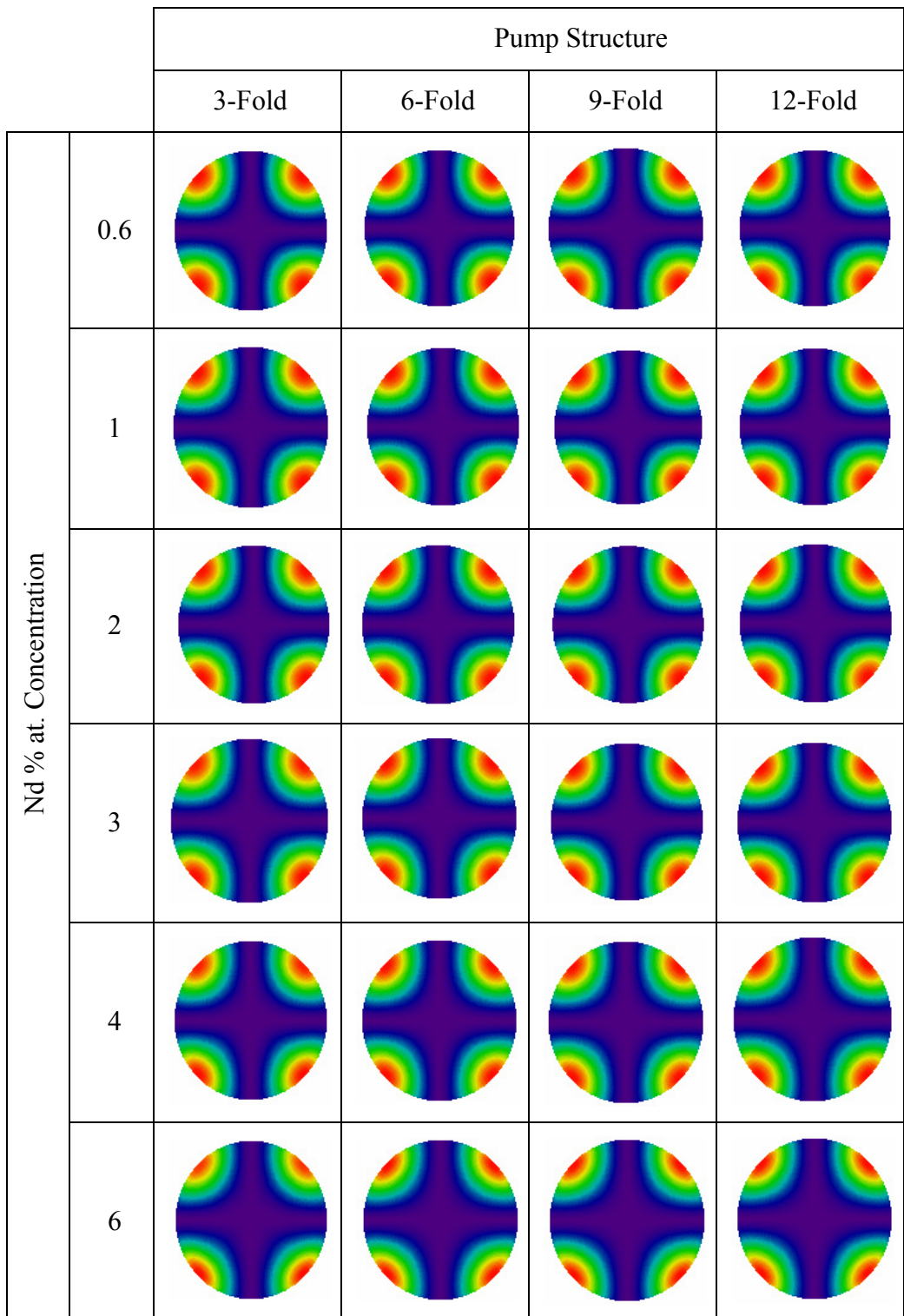
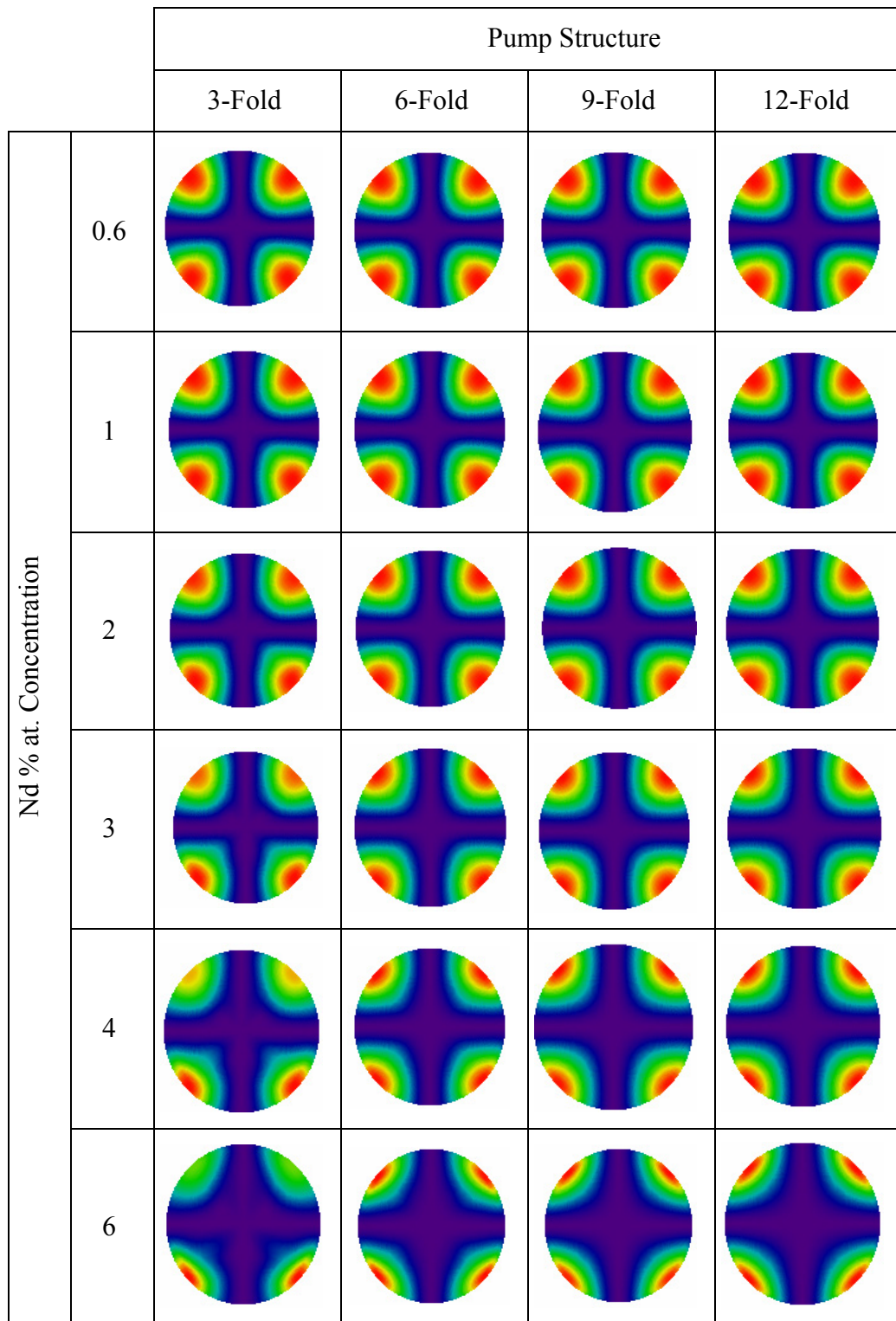


Table A13. 4 - Depolarization distribution of 6 mm rod pumped with 885 nm source



CURRICULUM VITAE

PERSONAL INFORMATION

Surname, Name: Kenar, Necmettin
Nationality: Turkish (TC)
Date and Place of Birth: 10 December 1975, Venetz, Bulgaria
Marital Status: Single
Phone: +90 535 695 60 86
Fax: +90 312 257 11 94
Email: necmettinkenar@gmail.com

EDUCATION

Degree	Institution	Year of Graduation
MS	METU Physics	2003
BS	METU Mechanical Engineering	2000
BS	METU Physics	2000
High School	Beydere Agricultural Technical High School, Manisa	1994

WORK EXPERIENCE

Year	Place	Enrollment
2006-Present	KENAR Mühendislik	
2002-2006	METU Department of Physics	Research Assistant
1995-2002	Ministry of Agriculture	Technician

FOREIGN LANGUAGES

English,